12-8-2017

Microstructural Behavior And Multiscale Structure-Property Relations For Cyclic Loading Of Metallic Alloys Procured From Additive Manufacturing (Laser Engineered Net Shaping -- LENS)

Mohammad Ali Bagheri

Microstructural behavior and multiscale structure-property relations for cyclic loading of metallic alloys procured from additive manufacturing (Laser Engineered Net Shaping – LENS)

By

Mohammad Ali Bagheri

A Dissertation
Submitted to the Faculty of
Mississippi State University
in Partial Fulfillment of the Requirements
for the Degree of Doctor of Philosophy
in Engineering
in the Department of Mechanical Engineering

Mississippi State, Mississippi

December 2017

Microstructural behavior and multiscale structure-property relations for cyclic loading of metallic alloys procured from additive manufacturing (Laser Engineered Net Shaping – LENS)

By

Mohammad Ali Bagheri

Approved:

_____

Mark F. Horstemeyer
(Major Professor)

_____

James C. Newman Jr.
(Committee Member)

_____

Yucheng Liu
(Committee Member / Graduate Coordinator)

_____

Youssef Hammi
(Committee Member)

_____

Jason M. Keith
Dean
Bagley College of Engineering

Name: Mohammad Ali Bagheri

Date of Degree: December 8, 2017

Institution: Mississippi State University

Major Field: Engineering

Major Professor: Mark F. Horstemeyer

Title of Study: Microstructural behavior and multiscale structure-property relations for cyclic loading of metallic alloys procured from additive manufacturing (Laser Engineered Net Shaping – LENS)

Pages in Study 117

Candidate for Degree of Doctor of Philosophy

The goal of this study is to investigate the microstructure and microstructure-based fatigue (MSF) model of additively-manufactured (AM) metallic materials. Several challenges associated with different metals produced through additive manufacturing (Laser Enhanced Net Shaping – LENS®) have been addressed experimentally and numerically. Significant research efforts are focused on optimizing the process parameters for AM manufacturing; however, achieving a homogenous, defect-free AM product immediately after its fabrication without post-fabrication processing has not been fully established yet. Thus, in order to adopt AM materials for applications, a thorough understanding of the impact of AM process parameters on the mechanical behavior of AM parts based on their resultant microstructure is required. Therefore, experiments in this study elucidate the effects of process parameters – *i.e*. laser power, traverse speed and powder feed rate – on the microstructural characteristics and mechanical properties of AM specimens. A majority of fatigue data in the literature are on rotation/bending test of wrought specimens; however, few studies examined the fatigue behavior of AM specimens. So, investigating the fatigue resistance and failure mechanism of AM

specimens fabricated via LENS® is crucial. Finally, a microstructure-based MultiStage Fatigue (MSF) model for AM specimens is proposed. For calibration of the model, fatigue experiments were exploited to determine structure-property relations for an AM alloy. Additional modifications to the microstructurally-based MSF Model were implemented based on microstructural analysis of the fracture surfaces – *e.g.* grain misorientation and grain orientation angles were added to the MSF code.

DEDICATION

I would like to dedicate this work to my parents and my wife, who have supported me with love and respect throughout graduate school.

ACKNOWLEDGEMENTS

First, I would like to thank my advisor, Dr. Mark F. Horstemeyer, who, without his direction, input, mentoring, and friendship, this dissertation would not be possible. I would also like to thank my former advisor, Dr. Nima Shamsaei, for introducing me to the world of additive manufacturing and fatigue modeling approach. Expressed appreciation is also due to Dr. Ricolindo Carino for his help with the numerical simulations. I want to thank Dr. Mohammad Javad Mahtabi as he has definitely been a positive influence in my research, and along with all of the help and mentoring that he has given me. Also, I would like to thank Army Research Laboratory (ARL) and Bagley College of Engineering. Special thanks to the Center for Advanced Vehicular Systems (CAVS) for allowing me to use the testing equipment and other facilities that made this research possible. I will treasure the friendships I made while in graduate school and the many discussions I was able to have with Denver Seely, Bradley Huddleston, Shiraz Mojahed, Yubraj Paudel and Andrew Bowman. Finally, I would like to express gratitude to my wife, Azadeh, for all of the support that she gave during graduate school.

TABLE OF CONTENTS

LIST OF TABLES

LIST OF FIGURES

CHAPTER I

INTRODUCTION

1.1 Additive Manufacturing Technologies

American Society for Testing and Materials (ASTM) defines Additive Manufacturing (AM) as ‘‘a process of joining materials to make objects from 3D model data, usually layer upon layer, as opposed to subtractive manufacturing methodologies. Synonyms include additive fabrication, additive processes, additive techniques, additive layer manufacturing, layer manufacturing, and freeform fabrication’’ [1]. According to ASTM’s broad definition of AM, all classes of materials such as metals, ceramics, polymers, composites, and biological systems can be included in AM. Despite use in materials processing applications for over twenty years, AM only recently has become an attractive tool for commercial manufacturing [1,2].

AM manufacturing techniques enable us to fabricate geometrically complex net-shaped pieces and assemblies where traditional manufacturing techniques fail. New developments in AM processes as well as new advanced materials extend our approaches for product development, manufacturing, and supply chain management [3,4]. AM techniques are categorized based on the feed stock form (*e.g.*, powder versus wire), feeding system (*e.g.*, powder bed versus blown powder), energy source (*e.g.*, laser versus electron beam), and materials in use (*e.g.*, metal versus polymer) [5–7].

The advantages of AM, such as fewer geometrical constraints, allow for new design paradigms that can optimize the time, cost, and design of manufactured products. The AM technology is also suitable for manufacturing functionally-graded parts. As AM technology made remote manufacturing and repair (in space, at sea) possible, it became a potential candidate for fabrication of functional service parts in various industries, such as aerospace and biomedical. However, the use of AM for load bearing parts is still an active area of research [8]. Uncertainty in structural properties of AM fabricated parts is the main concern holding back industries from using AM technology for manufacturing [6,7,9] due to the heterogeneous microstructures and randomly dispersed defects observed in AM parts [10]. Different factors introduce variations that make the AM process uncertain, including powder characteristics, building procedure, and AM systems. Additionally, many process parameters produce variation in the final part, especially factors shaping the thermal history of products, such as laser power, laser speed, and layer thickness. [6,7,10].

1.2 Microstructure and Process Parameters

The thermal history during the manufacturing of AM parts strongly influences their microstructural characteristics (*e.g*. morphology and grain size). The thermal history includes high heating/cooling rates, significant temperature gradients, and bulk temperature rises. Predicting the microstructural features of AM parts is a major challenge due to the uncertainty surrounding the process parameters that affect the thermal history. However, determining the influence of the thermal history on microstructural characteristics of AM parts is required to establish the effective control mechanisms for fabricating AM parts with superior mechanical properties. Various

studies [5-10] have been done on AM parts with specific shapes to investigate the impact of certain thermal history parameters on their microstructural characteristics and material properties [9–14]. However, the ability to exploit these findings for fabrication of complex pieces is unclear, because the microstructure dependence on the thermal history is geometry dependent.

Finer microstructures can be created by fast cooling rates produced by an increasing traverse velocity and a decreasing laser power as they decrease the incident energy at the top of the AM part. In contrast, the combination of a lower traverse speed and higher laser power results in coarser microstructures due to lower cooling rates [6,10,11].

Grain morphologies of AM parts that are strongly affected by material-type and laser strength play a pivotal role in determining the morphology of AM parts too (*e.g.* fine vs coarse). In general, finer equiaxed structures are produced as a result of lower incident energy, which can be generated by laser attenuation and/or radiation effects, while columnar grains and coarser microstructures are produced as a result of higher incident energy [6]. For example, in thin walls of Direct Laser Deposition (DLD) Ti-6Al-4V, increasing the incident energy (by decreasing laser traverse speed and/or increasing laser power) increases the grain size [11,12]. In the case of Ti-6Al-4V, a coarser microstructure (*e.g.*, an increase in length and width of both α and β laths) is formed by increasing powder feed rate. However, at higher laser powers, the effect of feed rate is minimal. Increased traverse velocity causes a slight decrease in the size of α and β laths and introduces more porosity. Further studies on a burn-resistant Ti alloy (Ti-25V-15Cr-2Al-0.2C), Waspalloy [15], and Inconel 625 [16] reported similar effects of process

parameters on the microstructural properties. Studies on a burn-resistant Ti alloy with mainly equiaxed grains reported that the microstructure is less dependent on process parameters than the thermal history [6,15,16].

During the AM process, heat conduction through the deposited structure is the primary way of transferring the incident energy [1]. Highly directional columnar structures are typically formed in areas with fast/high cooling rates, including areas near the substrate or through previously-deposited layers. The columnar structures can extend across the deposited layers, indicating epitaxial growth of dendrites from the substrate or previously deposited layers [6]. Microstructural properties of AM parts, such as grain size, are progressively modified via a variety of metallurgical phenomena activated by the thermal history [17]. Heterogeneous behavior in the microstructure caused by variation in the thermal history experienced at different locations along an AM part affects other mechanical properties, such as tensile strength and fatigue resistance [18].

For DLD processes, distribution of powder density in the melt pool (deposited mass flow rate) is affected by powder feed rate [19], which also affects layer height and microstructure. According to a study conducted by Liu and Dupont, as the powder feed rate increases, layer height increases linearly, leading to a coarser microstructure [20]. For a fixed powder feed rate, the amount of powder that is injected into the melt pool varies for different laser scanning directions because of the distance between the powder stream and laser spot. Depending on scanning direction, the powder injection point may be ahead or behind the laser spot.

1.3 Mechanical Properties

Overall, the mechanical properties under static loading (*e.g*. such as tensile, compressive, and hardness) of AM parts are comparable to or even higher than parts fabricated by conventional methods [21]. Microstructural observations can be explained by the relatively higher cooling rates experienced by AM parts during their fabrication, which results in a finer microstructure compared to the parts fabricated by conventional methods, which leads to the same mechanical properties (such as yielding strength and ultimate tensile strength). [7,8,22,23]. Although a number of studies investigated the mechanical characterization of AM parts, the mechanical behavior of AM parts, such as trustworthiness and durability is still an active area of research [8].

Fatigue resistance is defined as the weakening of a material under repeated applied loads, which is a common mode of mechanical failure in many engineering structures. The performance and durability of AM parts under cyclic loading, *i.e*. their fatigue resistance is a major challenge and concern for using metallic AM parts [8,24,25].

Failure caused by fatigue is mostly a local phenomenon caused by impurities and microstructural heterogeneity. Since microstructural heterogeneity is commonly observed in AM parts, they are more susceptible to the fatigue failure than their wrought counterparts [8,24,25]. Therefore, a thorough understanding of the mechanisms of fatigue damage, fatigue failure, and their dependence on the microstructure of AM materials is required to improve the trustworthiness and durability of AM parts.

1.4 Microstructure-Based MultiStage Fatigue Modeling of Alloys

Fatigue damage incubation and development occurs in four major stages: fatigue crack incubation, microstructurally small crack (MSC) growth, physically small crack

(PSC) growth, and long crack (LC) growth [26]. The Multistage Fatigue (MSF) model is based on this categorization of fatigue damage [27]. The MSF model is used to predict the fatigue damage arising from various microstructural features. The MSF model takes into account microstructural inclusions (pores, oxide films, and particles), porosity, dendrite cell size (DCS), and nearest neighbor distance of defects (NND) in order to accurately predict the fatigue damage in wrought material – *e.g*. aluminum alloy, magnesium alloy, and steel alloy. [27]. The MSF model was utilized to predict the fatigue behavior of LENS®-processed steel [28]. As LENS® steel possesses a significant amount of pores and weakly bonded particles, the experimentally observed fatigue damage was similar to cast alloys. Although a number of studies investigated fatigue behavior of AM parts, the impact of microstructural characteristics, such as grain size, grain misorientation angle, and grain orientation angle on fatigue behavior of AM parts, is not well understood.

1.5 Objective and Organization

The goal of this dissertation is to address challenges associated with metal AM techniques using Laser Engineered Net Shaping (LENS®). In this regard, experimental and numerical investigation of microstructural, mechanical, and fatigue properties of AM metallic materials was performed. In the experimental section, the effects of process parameters on microstructural features and mechanical properties of AM specimens, fabricated via DLD, were investigated. Next, the effects of process-induced defects (*e.g*., voids, un-melted regions) on the fatigue life of NiTi were investigated. Finally, a microstructure-based MultiStage Fatigue (MSF) model for AM specimens is proposed.

The model was modified by implementing the effect of grain misorientation and grain orientation angle for a better fatigue life prediction of AM specimens.

An introduction to the additive manufacturing technology, mechanical properties, and microstructural characteristics of AM parts and the MSF model usage for prediction of fatigue behavior is provided in Chapter 1. Next, the impact of process parameters on the mechanical behavior and microstructural characteristics of AM parts is presented in Chapter 2. Fatigue resistance and failure mechanism of AM parts are described in Chapter 3. Fatigue-life prediction of AM parts via multistage fatigue model (MSF) is discussed in Chapter 4. A summary of results and final conclusion is presented in Chapter 5. Finally, future directions and potential research topics for advancing the knowledge in mechanical behavior of AM parts are discussed in Chapter 6.

1.6 References

[1] Alcisto J, Enriquez A, Garcia H, Hinkson S, Steelman T, Silverman E, et al. Tensile properties and microstructures of laser-formed Ti-6Al-4V. J Mater Eng Perform 2011;20:203–212.

[2] ASTM F2792-12A. Standard terminology for additive manufacturing technologies. West Conshohocken, PA: ASTM International; 2012.

[3] Lott P, Schleifenbaum H, Meiners W, Wissenbach K, Hinke C, Bültmann J. Design of an optical system for the In situ process monitoring of selective laser melting (SLM). Phys Procedia 2011;12:683–90. doi:10.1016/j.phpro.2011.03.085.

[4] Emelogu A, Marufuzzaman M, Thompson SM, Shamsaei N, Bian L. Additive manufacturing of biomedical implants: A feasibility assessment via supply-chain cost analysis. Addit Manuf 2016;11:97–113. doi:10.1016/j.addma.2016.04.006.

[5] Thompson SM, Bian L, Shamsaei N, Yadollahi A. An overview of Direct Laser Deposition for additive manufacturing; Part I: Transport phenomena, modeling and diagnostics. Addit Manuf 2015;8:36–62. doi:10.1016/j.addma.2015.07.001.

[6] Selcuk C. Laser Metal Deposition for Powder Metallurgy Parts. Powder Metall 2011;54:94–9. doi:10.1179/174329011X12977874589924.

[7] Frazier WE. Metal Additive Manufacturing: A Review. J Mater Eng Perform 2014;23:1917–28. doi:10.1007/s11665-014-0958-z.

[8] Shamsaei N, Yadollahi A, Bian L, Thompson SM. An overview of direct laser deposition for additive manufacturing; Part II: Mechanical behavior, process parameter optimization and control. Addit Manuf 2015;8:12–35. doi:10.1016/j.addma.2015.07.002.

[9] Mazumder J, Dutta D, Kikuchi N, Ghosh A. Closed loop direct metal deposition: art to part. Opt Lasers Eng 2000;34:397–414.

[10] Zheng B, Zhou Y, Smugeresky JE, Schoenung JM, Lavernia EJ. Thermal behavior and microstructural evolution during laser deposition with laser-engineered net shaping: Part I. Numerical calculations. Metall Mater Trans A 2008;39:2228–2236.

[11] Bontha S, Klingbeil NW, Kobryn PA, Fraser HL. Thermal process maps for predicting solidification microstructure in laser fabrication of thin-wall structures. J Mater Process Technol 2006;178:135–142.

[12] Bontha S, Klingbeil NW, Kobryn PA, Fraser HL. Effects of process variables and size-scale on solidification microstructure in beam-based fabrication of bulky 3D structures. Mater Sci Eng A 2009;513:311–318.

[13] Griffith ML, Schlienger ME, Harwell LD. Thermal behavior in the LENS process. Sandia National Labs., Albuquerque, NM (United States); 1998.

[14] Kobyrn PA, Semiatin SL. Mechanical properties of laser-deposited Ti-6Al-4V solid freeform fabrication symposium. Austin USA 2001.

[15] Pinkerton AJ, Karadge M, Ul Haq Syed W, Li L. Thermal and microstructural aspects of the laser direct metal deposition of waspaloy. J Laser Appl 2006;18:216–226.

[16] Dinda GP, Dasgupta AK, Mazumder J. Laser aided direct metal deposition of Inconel 625 superalloy: microstructural evolution and thermal stability. Mater Sci Eng A 2009;509:98–104.

[17] Costa L, Vilar R. Laser powder deposition. Rapid Prototyp J 2009;15:264–279.

[18] Keicher DM, Smugeresky JE. The laser forming of metallic components using particulate materials. Jom 1997;49:51–54.

[19] Li Y, Yang H, Lin X, Huang W, Li J, Zhou Y. The influences of processing parameters on forming characterizations during laser rapid forming. Mater Sci Eng A 2003;360:18–25.

[20] Liu W, Dupont JN. In-situ reactive processing of nickel aluminides by laser-engineered net shaping. Metall Mater Trans A 2003;34:2633–2641.

[21] Bian L, Thompson SM, Shamsaei N. Mechanical properties and microstructural features of direct laser-deposited Ti-6Al-4V. JOM 2015;67:629–38. doi:10.1007/s11837-015-1308-9.

[22] Spierings AB, Starr TL, Wegener K. Fatigue performance of additive manufactured metallic parts. Rapid Prototyp J 2013;19:88–94.

[23] Trosch T, Ströβner J, Völkl R, Glatzel U. Microstructure and mechanical properties of selective laser melted Inconel 718 compared to forging and casting. Mater Lett 2016;164:428–431.

[24] Yadollahi A, Shamsaei N, Thompson SM, Elwany A, Bian L. Effects of building orientation and heat treatment on fatigue behavior of selective laser melted 17-4 PH stainless steel. Int J Fatigue 2016. doi:10.1016/j.ijfatigue.2016.03.014.

[25] Stephens RI, Fatemi A, Stephens RR, Fuchs HO. Metal fatigue in engineering. Second. Wiley; 2000.

[26] Suresh S. Fatigue of materials. Cambridge university press; 1998.

[27] McDowell DL, Gall K, Horstemeyer MF, Fan J. Microstructure-based fatigue modeling of cast A356-T6 alloy. Eng Fract Mech 2003;70:49–80.

[28] Xue Y, Pascu A, Horstemeyer MF, Wang L, Wang PT. Microporosity effects on cyclic plasticity and fatigue of LENSTM-processed steel. Acta Mater 2010;58:4029–4038.

CHAPTER II

MICROSTRUCTURE AND MECHANICAL PROPERTIES OF TI-6AL-4V PARTS FABRICATED BY LASER ENGINEERED NET SHAPING

(*Published in* ASME, doi: 10.1115/IMECE2015-51698)

Laser Engineered Net Shaping (LENS®) is a Direct Laser Deposition (DLD) additive manufacturing technology that can be used for directly building complex 3D components from metal powders in a combined deposition/laser-melting process. In this study, the effect of LENS process parameters, such as laser power, powder feed rate and traverse speed, on the resultant microstructure, hardness and tensile strength of Ti-6Al-4V components was experimentally investigated. Optical Microscopy (OM) and Scanning Electron Microscopy (SEM) were used to characterize the microstructure in terms of grain size and morphology. Relationships between process parameters and the microstructural/mechanical properties are provided. Results indicated that the scale of columnar grains increased with slower laser traverse speeds while other process parameters were maintained constant. The sizes of α and β laths increased with higher laser powers and slower traverse speeds. The ultimate tensile and yield strengths of the LENS specimens were found to be higher than those of cast and wrought materials, and this can be generally attributed to the different cooling rates inherent to the LENS

process, which impacts grain size. The percent elongations to failure, however, were consistently lower than those measured in the wrought material.

2.1 Introduction

Titanium alloys have been widely investigated and utilized in a variety of applications, such as aircraft engines, structural components, and bio-applications (*e.g.* implants) due to their corrosion resistance, low density, high strength at elevated temperatures, and good formability. The primary alloying elements in Ti-6Al-4V are aluminum (Al) and vanadium (V) with trace amounts of oxygen (O) and nitrogen (N). Ti-6Al-4V is a commonly-used titanium alloy with a microstructure that is strongly sensitive to manufacturing process parameters and thermal history. The alloy consists of primary and secondary Hexagonal Close Packed (HCP) α grains along with scattered and stabilized Body Centered Cubic (BCC) β phases. The mechanisms and kinetics differ between these two phases, thus impacting the mechanical behavior of this alloy. Therefore, microstructural identification is essential to better understand and predict the mechanical behavior of many titanium alloys [1].

Laser Engineered Net Shaping (LENS®), a commercialized form of Direct Laser Deposition (DLD), is an additive manufacturing technology first developed by Sandia National Laboratories in the late 1990s [2]. The technology allows for the ability to produce complex metallic geometries which may be difficult to manufacture through conventional metal forming techniques. As shown in Fig. 2.1, during DLD, metal parts are manufactured layer-by-layer from a Computer Aided Design (CAD) solid model by injecting metal powder into a molten pool created by a laser beam. In order to fabricate the desired geometry, a substrate (or build plate) is scanned upon by the laser beam,

during which, powder deposition simultaneously occurs. By repeating the process, consecutive layers are sequentially built in the height-wise direction. Due to its significant cost-saving potential and ability to produce fine microstructures, the DLD process has become a unique means for rapid prototyping/manufacturing and product repair. The DLD process is also appealing for its potential to create functionally-graded compositions [3, 4].

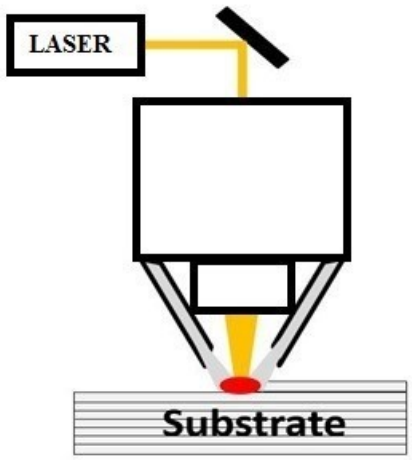

Figure 2.1 Schematic of the direct laser deposition (DLD) process.

Many studies have aimed to characterize the mechanical properties of various kinds of titanium alloys manufactured by DLD [5-9]. Such properties include yield strength, ultimate strength, and hardness, and have been shown to strongly depend on microstructure characteristics, such as area fraction, size, distribution, and the morphology of primary and secondary α phases, which are sensitive to the thermal history of the part. In many cases, any novelty in mechanical properties has been attributed to the fine microstructures produced by the high cooling rates inherent to the DLD process. The influence of laser power and number of passes on the microstructure

and hardness has also been evaluated [6]. The results show that the equiaxed α+β microstructure of the parts changes to a mixture of acicular α in β matrix after DLD due to the high cooling rates during the manufacturing process [2]. Furthermore, increasing the energy input increased the thickness of the remelted region. As a result of low cooling rates in the remelted region, the grain size of the alloy might increase/evolve further.

Kummailil *et al*. demonstrated that increasing the powder feed rate or laser power increases Ti-6Al-4V layer thickness, while increasing traverse speed decreases layer thickness [4, 10-12]. Brice *et al*. [6] illustrated the importance of monitoring/controlling the feed rate during DLD fabrication of Ti-6Al-4V. By monitoring/controlling the process parameters –*e.g*. laser power, traverse speed, and hatch spacing– higher quality deposits are achievable.

Kobryn *et al*. [7] investigated the effect of DLD process parameters (laser power and traverse speed) on microstructure, porosity, and build height of Ti-6Al-4V parts. The DLD parts were found to possess a columnar microstructure and a fine Widmanstätten microstructure. Their work demonstrated that increasing the laser power and traverse speed decreases the two types of porosity, namely lack-of-fusion and gas entrapment, in laser-deposited specimens. Besides, increasing the traverse speed decreases the build height, while laser power has an insignificant effect on build height. Wu *et al*. [11] also investigated the effects of process parameters on the deposited microstructure of thin-wall Ti-6Al-4V samples. The study reported that increasing the laser power causes a transition from columnar to mixed/equiaxed morphology in microstructure, while increasing the traverse speed decreases grain size. Also, the direction of the solidification

heat flux affects the grain morphology of laser-deposited thin-wall Ti-6Al-4V specimens [11].

Kelly and Kampe investigated the microstructure evolution of laser-deposited Ti-6Al-4V samples, using experimental [12] and modeling approaches [13]. Eighteen layers of a Ti-6Al-4V thin wall, deposited using AeroMet's laser forming process, were examined in their experimental study [12]. Optical microscopy, hardness, and composition measurements were used to illustrate that the layer-band and gradient morphologies are resultant from the complex thermal history throughout the build direction, and are not consequences of segregation or oxidation.

Thus far, only few studies examined fatigue behavior of additive manufacturing parts, therefore, improving the fatigue life of the fabricated products is becoming another challenge for researchers in this area. For instance, Dong Lin *et al*. [14] investigated the single layer graphene oxide reinforced metal matrix composites produced by Laser Sintering. Their investigation showed an improvement in the fatigue life after laser sintering of GO-reinforced iron matrix nanocomposites. In another study, Dong Lin *et al*. investigated the fundamental mechanism of fatigue performance enhancement during a novel hybrid manufacturing process. Adding TiN nanoparticles helped to further increase the dislocation density by laser shock peening and improved the mechanical properties [15].

In the current study, the evaluation of microstructure variation along the growth direction of the DLD build process was examined and the influence of laser processing parameters, laser output power, traverse speed, and powder feed rate on the resultant microstructure of Ti-6Al-4V rod-shaped specimens, were investigated. The goal was to

further expose the effects of DLD process parameters on the microstructure and mechanical properties of fabricated Ti-6Al-4V and compare with wrought and cast Ti-6Al-4V.

2.2 Experimental Procedure

The material used for this study was Ti-6Al-4V (AMS 4998C) spherical powder (-100/+325 mesh). An OPTOMEC LENS® 750 machine with a 1 kW laser source (Nd:YAG) was utilized to fabricate the specimens. Cylindrical specimens with diameter of 7 mm and height of 77 mm were manufactured. The DLD processing chamber was purged with argon to keep the average oxygen content below 20 ppm. Microstructural properties of the specimens were investigated by employing different combinations of process parameters, such as powder feed rate (0.08 and 0.16 gm/s), traverse speed (0.85, 1.27 and 1.69 cm/s), and laser output power (350 and 400 W). The different combinations of process parameters are shown in Table 2.1.

Table 2.1 The investigated direct laser deposition (DLD) process parameter combinations.

Laser Power (W)	Powder Feed Rate (gr/s)	Traverse Speed (cm/s)
350	0.156	0.85
		1.27
		1.69
400	0.076	0.85
		1.27
		1.69
	0.156	0.85
		1.27
		1.69

The layer thickness and hatch spacing were 0.02 mm and the layer orientation alternated between 0º and 90º as shown in Fig. 2.2.

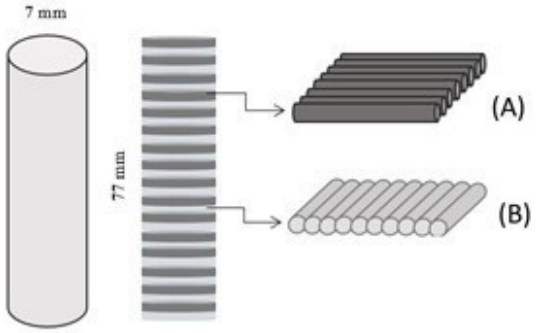

Figure 2.2 Schematic of direct laser deposition (DLD) deposition alternating patterns (A) 0^0 Rastering and (B) 90^0 Rastering.

Each fabricated specimen was cut into three sections and a morphology study was conducted on radial sections, while some were on the longitudinal of sections using Optical Microscopy (OM) and Scanning Electron Microscopy (SEM). The surface of each section was prepared by standard mechanical polishing and etched by a solution composed of 1 ml HF, 2 ml HNO3 and 68 ml H2O. The microstructure was characterized using a Zeiss Axiovert 200 Optical Microscopy (OM). The microhardness was measured on the surface of each section by using a LECO Vickers microindentation measurement device with a test load of 500 g and a hold time of 10 s. Five indentions were made across the polished radial sections of each 'as-deposited' specimen.

Using the different combinations of process parameters, as shown in Table 2.1, nine groups of samples were fabricated with 5 samples in each group. All samples were fabricated in the vertical direction (perpendicular to ground) on base plates one at a time. On each plate, 5 samples were fabricated, 4 samples on the corners of the plate and one

sample at the center of the plate. The plate dimensions were (152.5 mm)×(152.5 mm)×(3.2 mm). For each group, it took approximately 8 seconds to print one specimen layer and the total time of manufacture was approximately 20 min. Due to variation in process parameters, each set of specimens is expected to experience a different thermal history, especially regarding different cooling rates.

2.3 Results and Discussions

2.3.1 Microstructural Behavior

The microstructural features, and mechanical properties, of DLD specimens are mainly affected by their laser-imposed, volumetric thermal history, consisting of a complex, spatiotemporal temperature field that exists during processing. Prediction of, and designing for, a specimen final mechanical property is a major challenge since each process parameter has a different impact on thermal history.

Experimental results indicated that, for the majority of investigated process parameters, the microstructure of DLD Ti-6Al-4V was predominantly columnar containing large columnar prior β grains. Prior β grain boundaries were continuous across the multiple layers as shown in Fig. 2.3.

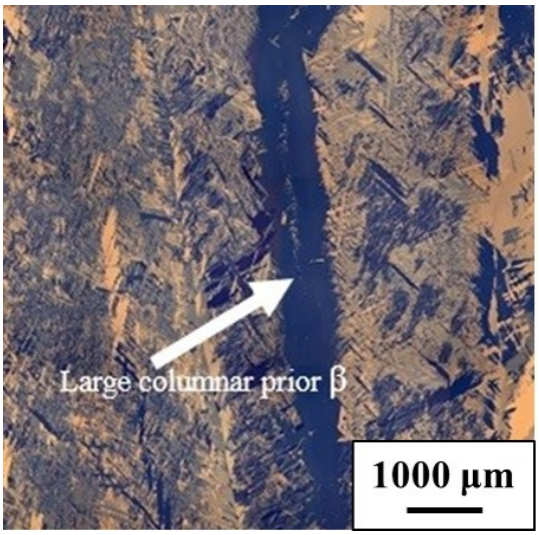

Figure 2.3 Columnar grain structure of longitudinal cross section at the top of the specimens. Indicating that β grain boundaries are continuous across the multiple layers.

When the fabrication process starts, the heat rapidly dissipates into the bottom substrate, and grains grow counter to the direction of the heat flux; upward in this case. The addition of each new layer results in re-melting the top surface columnar grains, thereby causing epitaxial growth. Kurs *et al*. also showed that the microstructure was columnar and parallel to the deposit build direction for all their deposited specimens [16].

During fabrication of the cylinder, a new layer overlaps a previously-deposited perimeter line, causing the outer surface of cylinder to be heated again. The outer edges of the specimen receive approximately twice as much heat input as the rest of the build, causing the perimeter of the cylinder to cool at a slower rate than the interior portion, which results in growth of equiaxed grains; shown in Fig. 2.4.

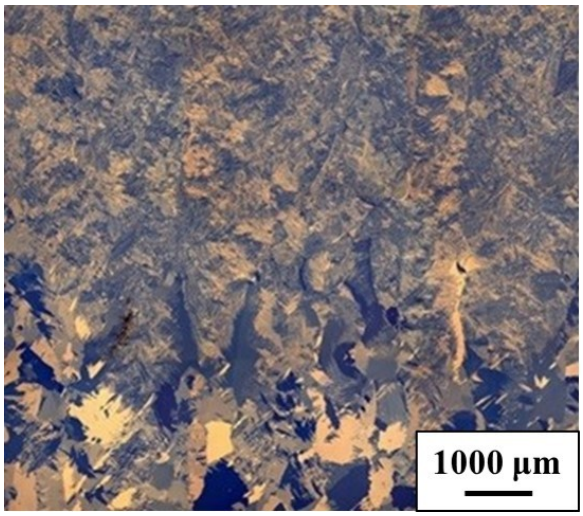

Figure 2.4 Equiaxed grain structure throughout the top cross-section of cylindrical specimens.

The microstructure between layers consist of basket-weave Widmanstätten α laths surrounded by retained β grain boundaries. Within the layers, the microstructure exhibits larger colonies of acicular α. The morphology of the layers deposited varies relative to the fully developed microstructure. These layers have experienced different thermal histories compared to previous layers and can be used to capture the intermediate development and evolution of the gradient α morphologies observed in the fully developed underlying layers.

2.3.1.2 Effect of Laser Power

The influence of laser power on the microstructure of DLD Ti-6Al-4V is presented in Fig. 2.5, where, the optical morphologies achieved at the same location for each deposited specimen with varying laser power are observable. The size of columnar grains, β lath, in each sample varies from edge-to-edge and from bottom-to-top. By increasing laser power, the length of the columnar grains decreases and are gradually replaced by large equiaxed grains; (α and β lath).

Increased laser power also removes pores resulting in production of denser layers. The density of the fabricated specimens was measured using Archimedes' principle. Higher laser power raises the temperature of deposited layers, which reduces the local cooling rates. In cases with extremely small temperature gradients, the microstructure will be composed primarily of equiaxed grains. Fig. 2.5 illustrates, for any given sample, the size of the α and β laths varies at different locations within the sample. These laths tend to become bigger towards the top of the samples, because the substrate becomes hot at the first layer, and the substrate and the build remain hot during subsequent deposition, which leads to the removal of columnar grains, while large equiaxed grains are formed – this has also been reported in the literature [7, 8, 13].

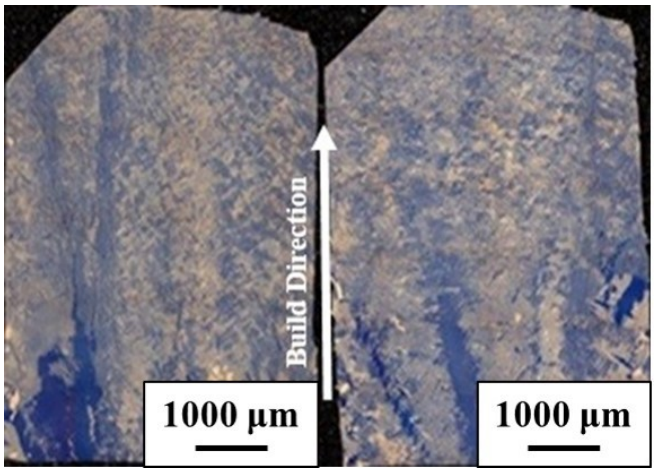

Figure 2.5 Effect of laser power throw-out the longitudinal cross section of the top of the specimens, left: 400 W, 0.16 gr/s and 0.85 cm/s, right: 350 W, 0.156 gr/s and 0.85 cm/s. Increasing the laser power causes a decrease in the length of columnar grains which are gradually transformed to large equiaxed grains; α and β lath.

2.3.1.3 Effect of Powder Feed Rate

Fig. 2.6 shows the effect of powder feed rate (0.08 and 0.16 gr/s) on microstructure. For constant laser power and traverse speed, increasing the powder feed

rate coarsens the microstructure. If the traverse speed increases, the powder feed rate must also increase proportionally to maintain full density. However, the variations in the results of the powder feed rates are negligible at the middle and the top of the sample, which lies in agreement with findings from the literature [3, 4, 12].

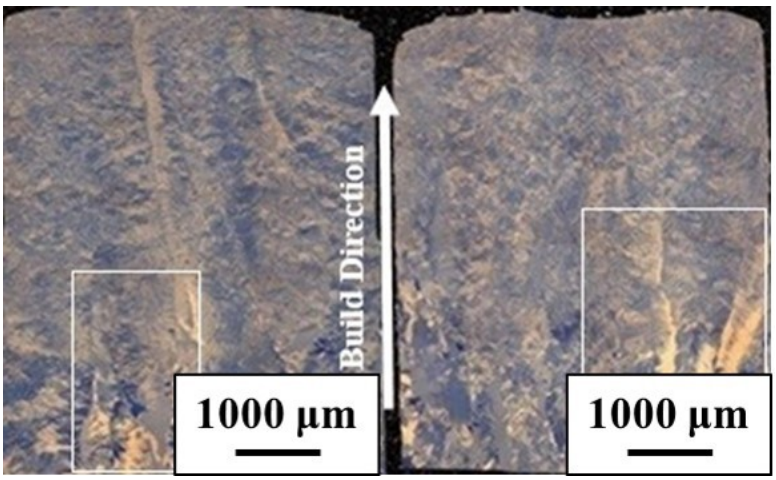

Figure 2.6 Effect of powder feed rate throw-out the longitudinal cross section of the top of the specimens, Left: 0.076 gr/s, 400 W and 0.169 cm/s, Right: 0.156 gr/s, 400 W, and 0.169 cm/s. The higher powder feed rate leads to coarser microstructures.

2.3.1.4 Effect of Traverse Speed

The influence of traverse speed on the morphology is shown in Fig. 2.7. For the same laser power and powder feed rate, with increasing traverse speed, the grain size decreases. The thickness of the layers further decreases by increasing the traverse speed. When the traverse speed increases, columnar grains become longer and finer due to the decreased energy density of the previously deposited layer. The reduction in energy input is because the laser and deposition head are traveling faster relative to the previously deposited layer, which results in a higher cooling rate. Higher cooling rates do not provide sufficient time for large grain growth. The resulting finer grains serve as

nucleation points for the subsequent layers, leading to continued epitaxial grain growth [7, 11-13].

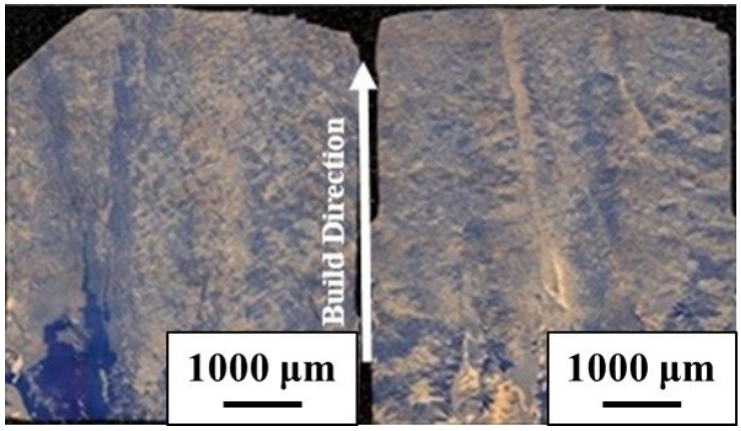

Figure 2.7 Effect of traverse speed throughout the longitudinal cross section of the top of the specimens, Left: 0.85 cm/s, 400 W and 0.156 gr/s, Right: 0.169 cm/s, 400 W and 0.156 gr/s. By increasing the traverse speed, longer and finer columnar grains are produced due to the decreased energy density of the previously deposited layer.

2.3.2 Mechanical Properties

2.3.2.1 Hardness Measurements

Effects of process parameters on specimen hardness are presented in Fig. 2.8. The experimental results clearly indicate that part hardness varies with observed microstructure. High hardness and smaller grain size are considered to improve the mechanical properties of Ti-6Al-4V. Results show that increasing the laser power raises the Vickers Hardness (HV) values, while increasing the traverse speed decreases HV, and increasing the powder feed rate does not have a significant effect on hardness. Microhardness tends to be greater at the bottom and top layers than in the middle of a specimen [17, 18]. Distinct microstructure regions with different micro-hardness values have been reported for DLD Ti-6Al-4V [19]. In one regard, the cooling rate of the melt

pool and velocity of solidification at the middle part region is slower than the top and bottom regions. In another regard, the middle region is exposed to the cyclic reheating from subsequent layer depositions. The higher cooling rates at the top and bottom regions typically result in a finer microstructure.

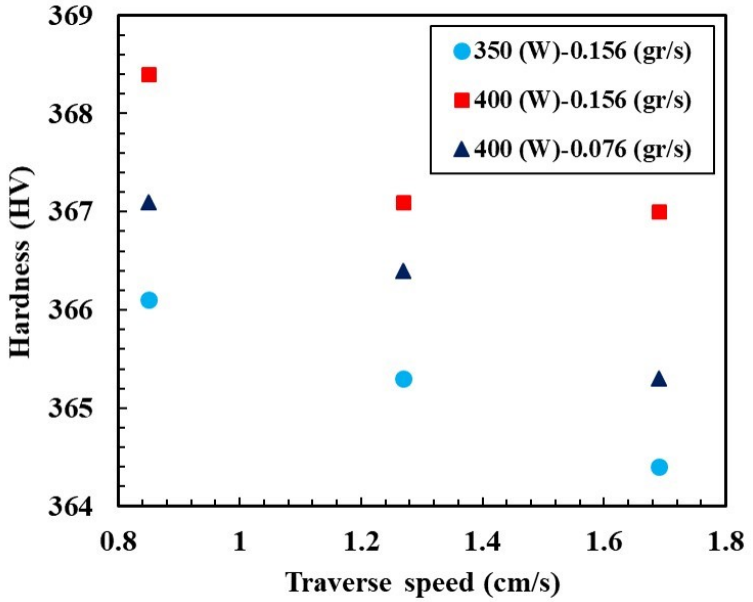

Figure 2.8 Microhardness along radius as a function of traverse speed. Increasing the laser power raises the Vickers Hardness (HV) values, however, HV is decreased by an increase in the traverse speed.

2.3.2.2 Tensile Tests

All the rod specimens were machined to 32 mm gage length, 4 mm gage diameter, 6 mm grip diameter, and fillet radius of 30 mm. The tensile loading axis was, therefore, parallel to the built direction. The yield strength and ultimate tensile strength (UTS) are shown in Figs. 2.9 and 2.10 as a function of traverse speed for different combinations of process parameters.

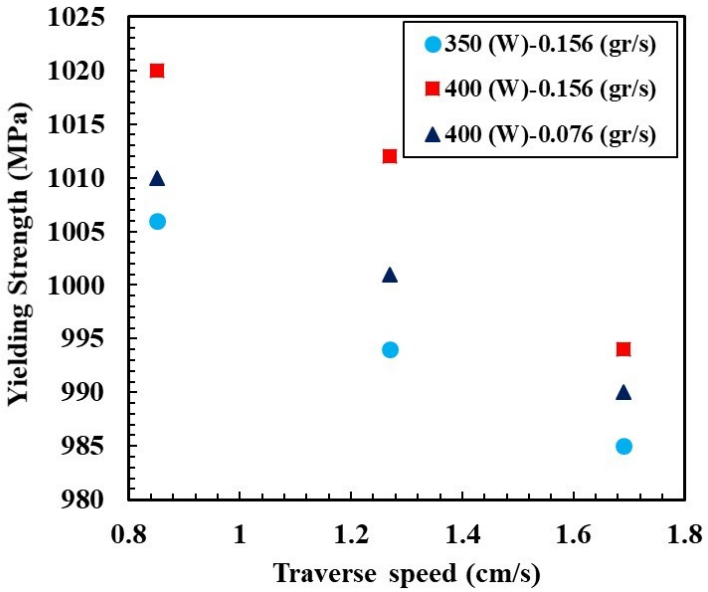

Figure 2.9 Yielding strength as a function of traverse speed. Yield strength of all direct laser deposition (DLD) fabricated specimens increases proportionally to the laser power and decreases inversely with powder feed rate.

The results indicate that the ultimate tensile strength and yield strength of all specimens fabricated by DLD increase proportionally to the laser power and decrease inversely with powder feed rate. However, there is no significant effect on elongation to failure observed.

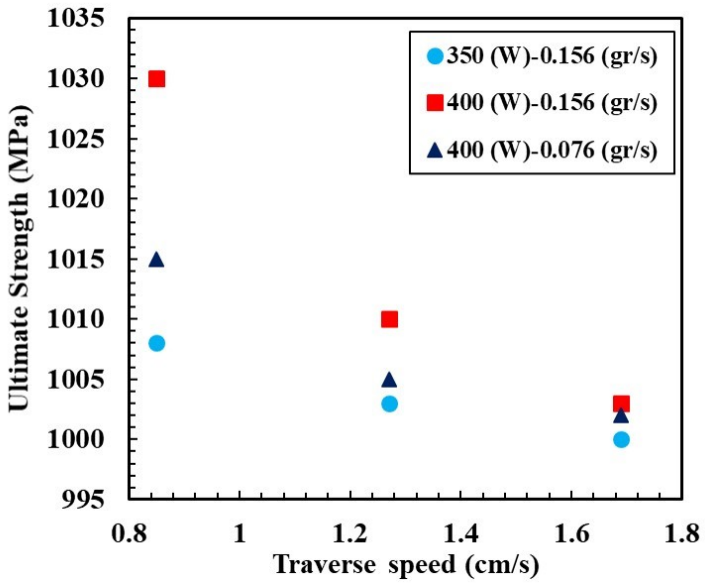

Figure 2.10 Ultimate tensile strength as a function of traverse speed. The ultimate tensile strength of direct laser deposition (DLD) fabricated specimens increases proportionally to the laser power and decreases inversely with powder feed rate.

Tensile properties for DLD Ti-6Al-4V and a comparison with cast, and wrought Ti-6Al-4V are illustrated in Fig. 2.11. The results show that the UTS and yield strength for DLD specimens are slightly higher than those for wrought and annealed materials. The difference in strength can be attributed to higher cooling rates inherent to DLD, impacting grain size. Fig. 2.11 shows that the UTS and yielding strengths of DLD specimens are lower than SLM and EBM products, likely due to the lower cooling rates associated with DLD, compared to the SLM and EBM techniques. The highest values for elongation to failure were obtained using the EMB method, as compared to LENS® and SLM. Using an electron beam as power source, as opposed to a laser, helps to melt the metal powder efficiently which leads to less porosity and reduced lack-of-fusion, thereby improving the elongation to failure rates values.

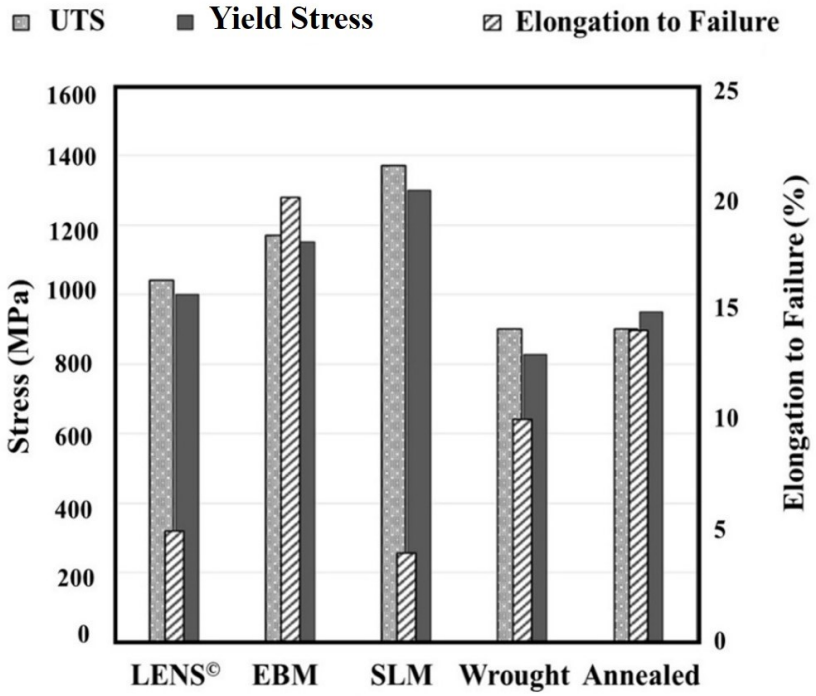

Figure 2.11 Comparison between direct laser deposition (DLD), electron beam melting (EBM) [20], selective laser melting (SLM) [20], wrought [21] and annealed [22-23] Ti-6Al-4V specimens. The elongation to failure for the DLD fabricated samples is significantly lower compared to the cast and wrought materials.

The elongation to failure for the DLD samples is significantly compared to the cast and wrought materials. Lack of fusion between layers (or lower laser penetration depths) creates voids, which can be seen at tensile fracture surface of DLD samples; and these voids contribute to the lower elongation to failure.

2.4 Conclusions

This study has investigated the effects of process parameters on microstructure and mechanical characteristics of Ti-6Al-4V fabricated by Laser Engineering Net Shaping (LENS®). From this work, the following conclusions were made regarding the Direct Laser Deposition (DLD) of Ti-6Al-4V:

1. By increasing traverse speed, columnar grains become longer and finer due to decreased energy density of the previously deposited layer, therefore, the thickness of the layers are decreased. If the traverse speed is increased, the powder feed rate must also increase proportionally to maintain full density.

2. By increasing laser power, the length of the columnar grains decreases and are gradually replaced by large equiaxed grains; (α and β lath). Also, increasing laser power reduces pores, resulting in denser layers.

3. The dynamic and repitious temperature gradients/spikes and sustainable cooling rates, inherent to fabricating DLD Ti-6Al-4V result in the prevalence of columnar microstructures. Besides, the width of columnar grains decreases by increasing the cooling rates using higher traverse speeds.

4. Higher ultimate and yield strengths are observed for fabricated specimens than cast and wrought Ti-6Al-4V. Higher cooling rates resulted in finer microstructures, which are mainly responsible for such increases. Occurrence of imperfections (*e.g.* voids, partially melted powder particles and oxide inclusions) lead to lower elongation to failure compared to the cast and wrought material.

2.5 References

[1] C.J. Maiden, S.J. Green, Compressive strain-rate tests on six selected materials at strain rates from 10- 3 to 104 in/in/sec, J. Appl. Mech. 33 (1966) 496–504.

[2] C. Atwood, M. Ensz, D. Greene, M. Griffith, L. Harwell, D. Reckaway, T. Romero, E. Schlienger, J. Smugeresky, Laser engineered net shaping (LENS (TM)): A tool for direct fabrication of metal parts, Sandia National Laboratories, Albuquerque, NM, and Livermore, CA, 1998.

[3] P.A. Kobryn, S.L. Semiatin, The laser additive manufacture of Ti-6Al-4V, JOM. 53 (2001) 40–42.

[4] P.A. Kobryn, S.L. Semiatin, Microstructure and texture evolution during solidification processing of Ti–6Al–4V, J. Mater. Process. Technol. 135 (2003) 330–339.

[5] C.L. Atwood, M.T. Ensz, D.L. Greene, M.L. Griffith, L.D. Harwell, F.P. Jeantette, D.M. Keicher, M.S. Oliver, D.E. Reckaway, J.A. Romero, others, Laser spray fabrication for net-shape rapid product realization LDRD, Sandia National Labs., Albuquerque, NM (US); Sandia National Labs., Livermore, CA (US), 1999.

[6] C.A. Brice, K.I. Schwendner, D.W. Mahaffey, E.H. Moore, H.L. Fraser, Process variable effects on laser deposited Ti-6Al-4V, in: Solid Free. Fabr. Proc., Austin, 1999: pp. 9–11.

[7] P.A. Kobryn, E.H. Moore, S.L. Semiatin, The effect of laser power and traverse speed on microstructure, porosity, and build height in laser-deposited Ti-6Al-4V, Scr. Mater. 43 (2000) 299–305.

[8] P. Kobryn, S.L. Semiatin, Laser Forming of Ti–6Al–4V: Research Overview, Solid Free. Fabr. Proc. Univ. Tex. Austin TX. (2000) 58–65.

[9] A. Foroush Bastani, Z. Ahmadi, and D. Damircheli, “A radial basis collocation method for pricing American options under regime-switching jump-diffusion models,” Appl. Numer. Math., vol. 65, no. Supplement C, pp. 79–90, Mar. 2013.

[10] J. Kummailil, C. Sammarco, D. Skinner, C.A. Brown, K. Rong, Effect of select LENSTM processing parameters on the deposition of Ti-6Al-4V, J. Manuf. Process. 7 (2005) 42–50.

[11] X. Wu, J. Liang, J. Mei, C. Mitchell, P.S. Goodwin, W. Voice, Microstructures of laser-deposited Ti–6Al–4V, Mater. Des. 25 (2004) 137–144.

[12] S.M. Kelly, S.L. Kampe, Microstructural evolution in laser-deposited multilayer Ti-6Al-4V builds: Part I. Microstructural characterization, Metall. Mater. Trans. 35 (2004) 1861.

[13] S.M. Kelly, S.L. Kampe, Microstructural evolution in laser-deposited multilayer Ti-6Al-4V builds: Part II. Thermal modeling, Metall. Mater. Trans. 35 (2004) 1869.

[14] A. F. Bastani and D. Damircheli, “On Adaptive Multiple-Shooting Method for Stochastic Multi-Point Boundary Value Problems,” Numer. Algorithms, vol. 74, no. 4, pp. 1119–1143, Apr. 2017.

[15] D. Lin, C. Ye, Y. Liao, S. Suslov, R. Liu, G.J. Cheng, Mechanism of fatigue performance enhancement in a laser sintered superhard nanoparticles reinforced nanocomposite followed by laser shock peening, J. Appl. Phys. 113 (2013) 133509.

[16] X. Guo, Fundamentals of solidification, Trans Tech Switz. (1986).

[17] H. El Kadiri, L. Wang, M.F. Horstemeyer, R.S. Yassar, J.T. Berry, S. Felicelli, P.T. Wang, Phase transformations in low-alloy steel laser deposits, Mater. Sci. Eng. A. 494 (2008) 10–20.

[18] B. Zheng, Y. Zhou, J.E. Smugeresky, J.M. Schoenung, E.J. Lavernia, Thermal behavior and microstructural evolution during laser deposition with laser-engineered net shaping: Part I. Numerical calculations, Metall. Mater. Trans. A. 39 (2008) 2228–2236.

[19] B. Baufeld, O. van der Biest, R. Gault, K. Ridgway, Manufacturing Ti-6Al-4V components by shaped metal deposition: microstructure and mechanical properties, in: IOP Conf. Ser. Mater. Sci. Eng., IOP Publishing, 2011: p. 012001.

[20] A. F. Bastani and D. Damircheli, “On Adaptive Multiple-Shooting Method for Stochastic Multi-Point Boundary Value Problems,” Numer. Algorithms, vol. 74, no. 4, pp. 1119–1143, Apr. 2017.

[21] P.A. Kobryn, S.L. Semiatin, Mechanical properties of laser-deposited Ti-6Al-4V, in: Solid Free. Fabr. Proc., Austin, 2001: pp. 6–8.

[22] S. Lampman, Wrought titanium and titanium alloys. ASM Handbook, Volume 2, Properties and selection: nonferrous alloys and special-purpose material, ASM International, 1990, ASM Handb. DVD ASM Int. Dialog Corp. (1999).

[23] H. Mahabadipour, H. Ghaebi, Development and comparison of two expander cycles used in refrigeration system of olefin plant based on exergy analysis, Appl. Therm. Eng. 50 (2013) 771–780

CHAPTER III

FATIGUE BEHAVIOR AND CYCLIC DEFORMATION OF ADDITIVE MANUFACTURED NITI

(*Published in* Journal of Materials Processing Technology, doi.org/10.1016/j.jmatprotec.2017.10.006)

The aim of this study is to experimentally investigate the fatigue behavior of additively manufactured (AM) NiTi (*i.e*. Nitinol) specimens and compare the results to the wrought material. Additive manufacturing is a technique in which components are fabricated in a layer-by-layer additive process and based on the desired geometries using sliced CAD models. NiTi rods were fabricated in this study using Laser Engineered Net Shaping (LENS), a Direct Laser Deposition (DLD) AM technique. Due to the high plateau stress of the as-fabricated NiTi, all the AM specimens were heat-treated under two different conditions (*i.e*. aging followed by air cooling and solution annealing followed by water quenching) to reduce their plateau stress, close to the one for the wrought material. Two different heat treatment processes, resulting in different stress plateaus, were employed to be able to compare the results in stress- and strain-based fatigue analysis. Strain-controlled constant amplitude pulsating fatigue experiments were conducted on heat-treated AM NiTi specimens at room temperature (~24°C) to

investigate the cyclic deformation and fatigue behavior. Fatigue lives of AM NiTi specimens were observed to be shorter than wrought material specifically in the high cycle fatigue regime. Fractography of the fracture surface of fatigue specimens, by means of Scanning Electron Microscopy (SEM), revealed the microstructural defects such as voids, resulting from entrapped gas or lack of fusion and serving as crack initiation sites, to be the main reasons for the shorter fatigue lives observed for AM NiTi specimens. However, the maximum stress level found to be the most influential factor in the fatigue behavior of superelastic NiTi.

3.1 Introduction

NiTi (*i.e*. Nitinol) is an almost equiatomic alloy of nickel and titanium and exhibits unique properties such as shape memory and superelasticity (also called pseudoelasticity). Shape memory is the ability of the material to recover a plastic strain by heating the material to above a certain temperature, while superelasticity is the capability of the material to recover strain levels as large as 4%-8% by just unloading. Because of these properties as well as high resistance to severe environmental conditions, NiTi has been utilized in various applications in civil engineering, automotive, aerospace and biomedical industries. Endovascular stents, endodontic files, and vena cava filters are some examples of NiTi application in the biomedical industry [1–3]. In addition, NiTi has been used for bio-implants [4,5] where an appropriate combination of mechanical properties as well as biocompatibility is needed. In such applications, however, the main challenge is the size and geometry of the implant, which is patient-injury dependent, making the design and fabrication of the implant somewhat complicated.

The process of fabricating NiTi parts with complex geometries using conventional techniques, such as machining, metal stamping, forging, casting and powder metallurgy, is excessively difficult. Machining NiTi parts, although possible, is cumbersome due to the work hardening property of the material [6]. Moreover, mechanical properties of NiTi, such as modulus of elasticity and loading/unloading stress plateaus, are very sensitive to the manufacturing and post-manufacturing processes such as the amount of prior cold work as well as heat treatment time and temperature [7]. For instance, the loading and unloading stress plateau levels are highly sensitive to the temperature difference between the operating temperature and the austenite finish temperature, A_f. On the other hand, the transformation temperatures of NiTi alloys vary significantly by altering the heat treatment process [2]. Existence of an insignificant amount of impurities such as oxygen content would also cause a large variation in the mechanical properties of this alloy such as fatigue strength [8].

Vacuum arc melting (VAM) and vacuum induction melting (VIM) followed by casting, hot working or cold working with intermediate annealing and finally shape memory treatment, are the most commonly used commercial methods for the production of NiTi components [9]. Due to the high affinity of titanium towards oxygen, the melting process in these methods has to be conducted in a vacuum or inert atmosphere. In vacuum arc melting process, in order to have sufficient homogeneity, re-melting several times is required because of the small molten zone present, which is produced as the arc progressively melts the electrode. Therefore, there is a less homogeneous distribution in chemical composition along the ingot. As a result of the variation in the chemical composition from top to bottom of the ingot, the transformation temperatures may vary

more than 10˚C along the height of the ingot. By repeating the vacuum arc re-melting (VAR) process, so called multiple melting process, a more homogeneous ingot may be achieved [6]. In addition, the vacuum induction melting process has the drawback of crucible contamination to calcia (CaO) or graphite, meaning that molten NiTi picks up carbon contaminants from the crucible, which in turn may change the transformation temperature [6]. Finally, the main problem related to the casting process is the presence of high level of microstructural defects [10], which can significantly affect the mechanical behavior and fatigue resistance of the product.

Various fabrication processes have been developed in order to overcome the issues related to the melting process and conventional machining of NiTi parts. Accordingly, powder metallurgy methods like hot isostatic pressing (HIP) [11,12], self-propagating high-temperature synthesis (SHS) [13,14], metal injection molding [11,15,16], and normal sintering have been utilized to fabricate NiTi components. In powder metallurgy techniques, since the pressure has to be applied equally from all directions, fabrication of parts with more complex geometries becomes increasingly challenging.

Laser Engineered Net Shaping (LENS) is a Direct Laser Deposition (DLD) additive manufacturing (AM) technique where the metal powder is injected into the melt pool created from the laser beam, forming the object. In the late 1990s, Sandia National Laboratories first developed DLD technique [17], provides the ability of producing and cladding metallic materials with complex geometries, which are difficult to fabricate by the conventional manufacturing techniques. In the DLD process, components are fabricated layer-by-layer based on a sliced CAD model, and injecting metal powder into a

molten pool, created by a laser beam. The desired geometry is formed by repeating this process and adding consecutive layers along the height. As a result of its cost-saving potential, ability to produce fine microstructures and create functionally-graded compositions, the DLD process has become a unique technique for rapid prototyping/manufacturing and product repair [18].

Using AM processes to fabricate structural components still has major challenges due to the AM materials possessing different microstructure, mechanical and, more importantly, fatigue properties as compared to their wrought counterparts [19]. Different microstructure and mechanical properties can be obtained by adjusting various process parameters such as laser power, beam travel speed, layer thickness, and powder feed rate, which provide complex thermal histories [20]. Different thermal histories, subsequently, may create a non-homogeneous, anisotropic microstructure with inevitable porosity and defects [19]. Generally, monotonic mechanical properties of AM metallic materials, such as tensile and compressive strengths, as well as hardness, are comparable to or even higher than wrought and cast materials, due to a higher cooling rate during the AM process, resulting in finer microstructures [21,22]. However, the fatigue strength of the AM components are reported to be lower due to the detrimental effects of microstructural defects such as voids and un-melted particles [23–25]. Therefore, fabrication of AM components with superior mechanical and fatigue properties based on an effectively optimized set of controllable process parameters is an area of interest for the research community [19]. Although fabricating NiTi components using AM techniques has recently become very popular, fatigue performance of these components is still the main challenge against adopting these techniques in load bearing applications [26].

In most applications, NiTi components are under cyclic loads, and thus, their fatigue behavior should be thoroughly characterized [26]. Therefore, extensive investigations [26,27] have been conducted in the past two decades to investigate the fatigue behavior of NiTi materials fabricated by traditional techniques. However, fatigue data for AM NiTi are not readily available in the literature and the effects of manufacturing induced defects on their fatigue resistance are unknown. Lack of sufficient fatigue data on AM NiTi is partially due to the AM techniques being relatively new and in part because of difficulties involved in fatigue testing of NiTi specimens [26,28]. The aim of this study is to investigate the uniaxial fatigue behavior and failure mechanisms of superelastic NiTi specimens manufactured using LENS under strain-controlled pulsating ($R_\varepsilon = 0$) cyclic loads. Various aspects of the fatigue behavior of AM NiTi are compared to the wrought counterpart and results are discussed.

3.2 Material and Experimental Program

Spherical gas atomized NiTi powder (-100/+325 mesh), produced based on ASTM standard [29], was utilized to fabricated the AM NiTi rods in this study. The chemical composition of the powder included 55% nickel and 43% titanium in weight percent (50.7% Ni- 48.6%Ti in atomic percent). Details of the chemical composition of the powder are listed in Table 3.1.

Table 3.1 Chemical composition of NiTi powder used to fabricate specimens in this study.

Element	**O**	**Al**	**C**	**Fe**	**H**	**N**	**Cr**	**Ni**	**Ti**
Weight percent (%)	0.10	0.009	0.017	0.009	0.002	0.008	0.19	55.0	Balance

An OPTOMEC LENS® 750 machine, retrofitted with 1 kW laser source (Nd:YAG) was utilized to fabricate the AM specimens. NiTi rods of 8 mm diameter and 80 mm height, as shown in Fig. 3.1a, were manufactured one at a time (single-built), vertically on a pure titanium (grade 5) substrate. The AM processing chamber was purged with argon to control and keep the oxygen content below 5 ppm. Table 3.2 lists the LENS process parameters, *i.e*. laser power, scanning speed, powder feed rate, and layer thickness, utilized in manufacturing of NiTi bars. These parameters were selected through a process optimization study, based on the objective to obtain a high level of density for the AM material with reference to the wrought NiTi. The density of the AM bars were calculated based on the Archimedes' principle and the process parameters were selected to achieve 99.8% of the wrought NiTi density.

Table 3.2 Process parameters used for fabricating NiTi specimens by laser engineered net shaping (LENS®).

Laser power (W)	**Scanning speed (mm/s)**	**Powder feed rate (g/s)**	**Layer thickness (mm)**
280	8.47	0.06	0.2

As-fabricated NiTi bars were centered to ensure a constant diameter over the length of the bar and provide a smooth surface in the grip section. The centered bars then were machined to standard cylindrical specimens with uniform gage section with a 3.5 mm diameter, according to ASTM standard for strain-controlled fatigue testing [30]. Fig. 3.1b presents a picture of the machined specimen and the drawing of the specimens, illustrating the dimensions of the different sections, is also shown in Fig. 3.1c.

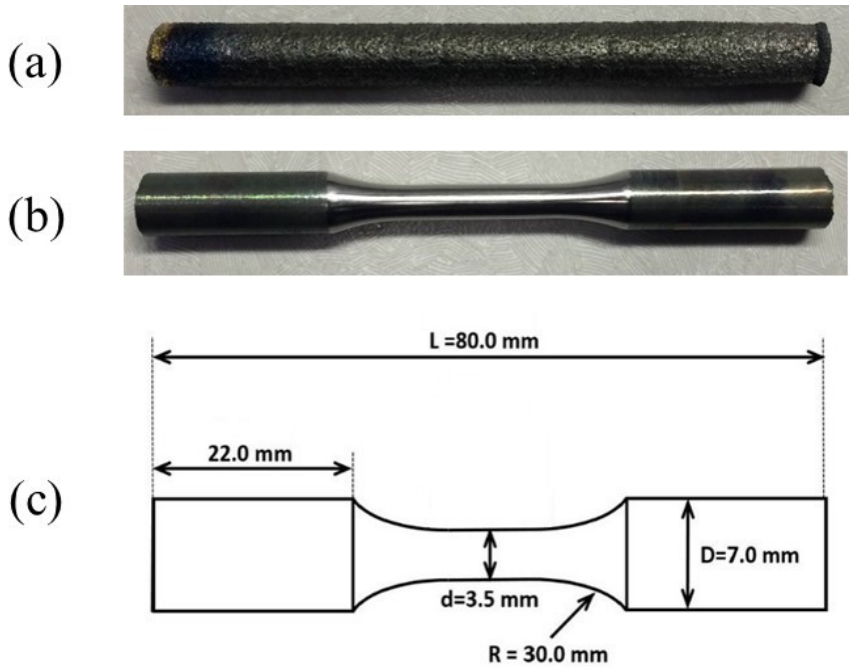

Figure 3.1 (a) As-Fabricated NiTi rod, (b) machined specimen, and (c) drawing of the fatigue specimen.

Machined cylindrical specimens were heat-treated in two different conditions. For the first heat treatment (HT1), the samples were aged at 550 °C for 60 min and cooled in air. Heat treatment 2 (HT2), however, included two steps: aging at 550 °C for 180 min and cooling in air, followed by solution annealing at 550 °C for 3 min and water quenching. Both heat treatments were selected to obtain a superelastic material at room temperature. The corresponding heat treatments for AM specimens were selected by trial and error so that two sets of specimens (*i.e*. AM HT1 and AM HT2) exhibit two different stress plateau levels, which enables investigating the fatigue behavior in strain-life and stress-life approaches. Gage sections of all the fatigue specimens were mechanically polished to minimize the effects of surface flaws on the fatigue life. In this case, sand papers from a rough level (girt #320) to a smooth level (girt #4000) were used to polish

all the specimens. Both monotonic and cyclic tests were performed in air and at room temperature (~ 24 °C).

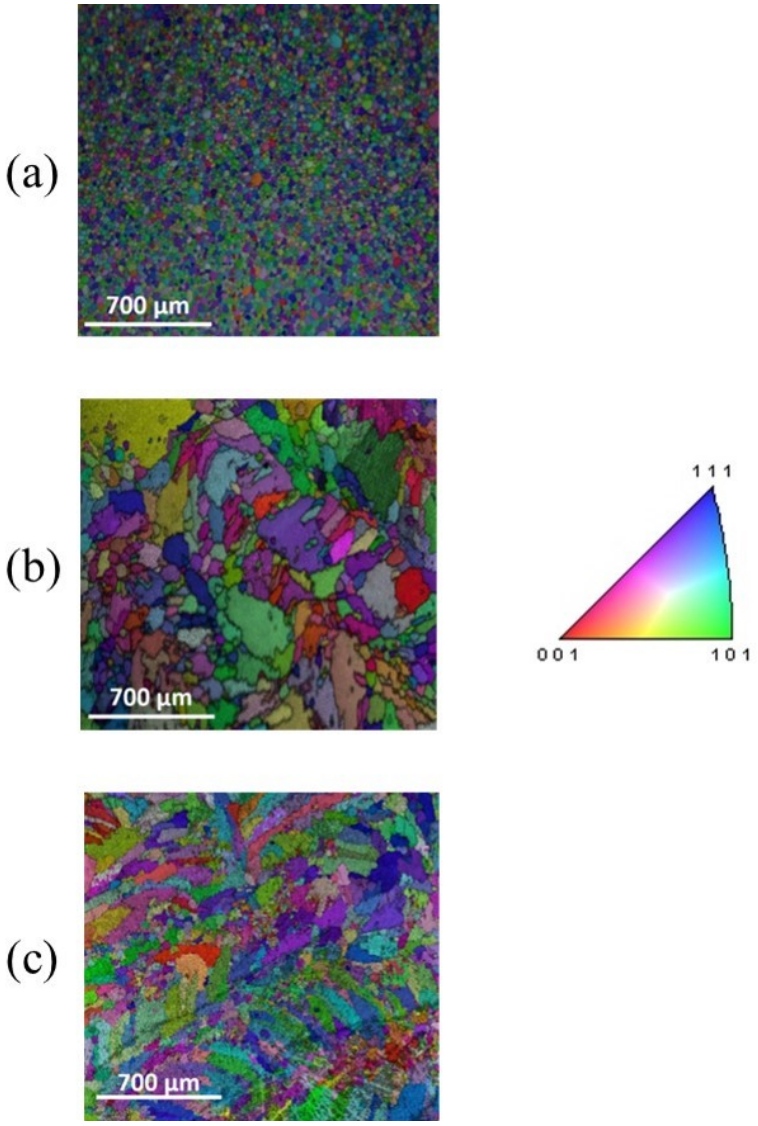

Figure 3.2 Electron backscatter diffraction (EBSD) colored map of microstructure of (a) wrought, (b) AM HT1, and (c) AM HT2 specimens indicating the grain shape, size, and orientation. The microstructure of AM specimens is different from wrought materials with significantly larger grain size and aspect ratio.

Microstructure of the heat-treated wrought and two AM NiTi specimens are shown in Fig. 3.2. As can be seen in Fig. 3.2a, grains in the heat-treated wrought NiTi are

uniformly distributed over the section of the specimen with an average grain size of ~5 μm and an aspect ratio of approximately one. AM specimens, however, show entirely different microstructure with significantly larger grain size and aspect ratio, as can be noticed from Figs. 3.2b and c. AM HT1 specimens, shown in Fig. 3.2b, appear to have significantly larger grain size due to lower cooling rate after annealing (cooled in air). The average grain size for this specimen was about 23 μm. AM HT2 specimens, which were quenched in iced water and underwent a very high cooling rate, has considerably smaller average grain size, as depicted in Fig. 3.2c, compared to AM HT1 specimen. The average grain size for this specimen was about 17 μm. As both AM HT1 and HT2 specimens have experienced a similar fabrication process, they are expected to inherit similar microstructures before the heat treatment process. Therefore, the observed different microstructure of these two specimens can be attributed to the effects of different heat treatments.

An MTS 810 uniaxial servo-hydraulic test system was used to perform all monotonic tests, on AM specimens, in a strain-controlled condition up to fracture. All the fatigue tests were conducted in pulsating strain-controlled condition ($R_\varepsilon = \varepsilon_{min}/\varepsilon_{max} = 0$) at different maximum strain levels (*i.e.* $\varepsilon_{max} = 0.6, 0.7, 0.8, 0.9, 1.0, 1.4$ and 2.0%) using an MTS 858 uniaxial servo-hydraulic testing machine. An MTS uniaxial extensometer with a gage length of 15 mm was used to measure and control the strain. All the cyclic tests were conducted at a constant average strain rate of ~ 0.1 s^{-1}, comparable to those used for testing wrought material [31]. Scanning electron microscopy (SEM) was used to observe the fracture surface of the fatigue specimens and study the crack initiation and propagation characteristics.

3.3 Deformation Behavior and Discussion

3.3.1 Monotonic Tensile Behavior

Tensile stress-strain curves of AM NiTi specimens, from monotonic tests, are compared with the one for wrought material in Fig. 3.3. The data related to the wrought material are from the authors' recent work [31]. As can be seen in this figure, the two heat treatment processes, selected for the AM NiTi specimens, resulted in plateau stresses somewhat comparable to the plateau stress of the wrought material. Fig. 3.3 also illustrates that the elongation to failure was ~ 4% and ~ 5% for AM HT1 and HT2 specimens, respectively, as compared to ~ 12% for the wrought counterpart. Thus, similar to other materials fabricated by LENS [20,32], AM NiTi specimens exhibit shorter elongation to failure than the wrought NiTi.

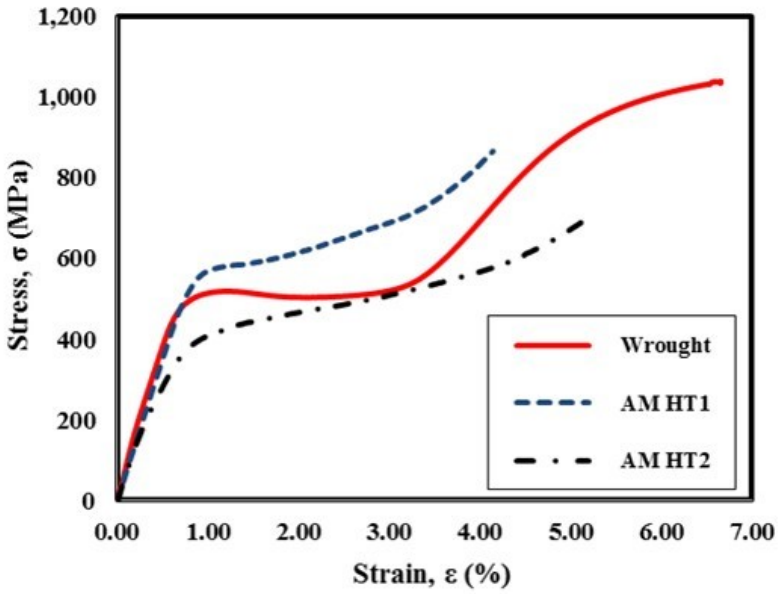

Figure 3.3 Comparison of the monotonic tensile stress-strain response of the wrought [31] and AM NiTi. Presence of the microstructural defects, such as voids and/or un-melted regions in AM specimens, may have contributed to the smaller elongation to failure of AM specimens.

Tensile specimens in all three conditions had a flat fracture surface with no indication of necking before final fracture. However, as shown in Fig. 3.4, dimples were observed on the fracture surface of both wrought and AM specimens, depicting a ductile fracture under tensile loading. Larger and deeper dimples, observed on the fracture surface of the wrought specimen (right column of Fig. 3.4a), can explain the larger elongation to failure and ductility, observed for this sample as compared to AM specimens. Presence of the microstructural defects such as voids (middle column of Figs. 3.4b and c), resulting from entrapped gas and/or un-melted regions, due to lack of fusion and/or low laser penetration depth, may have contributed to the smaller elongation to failure of AM specimens.

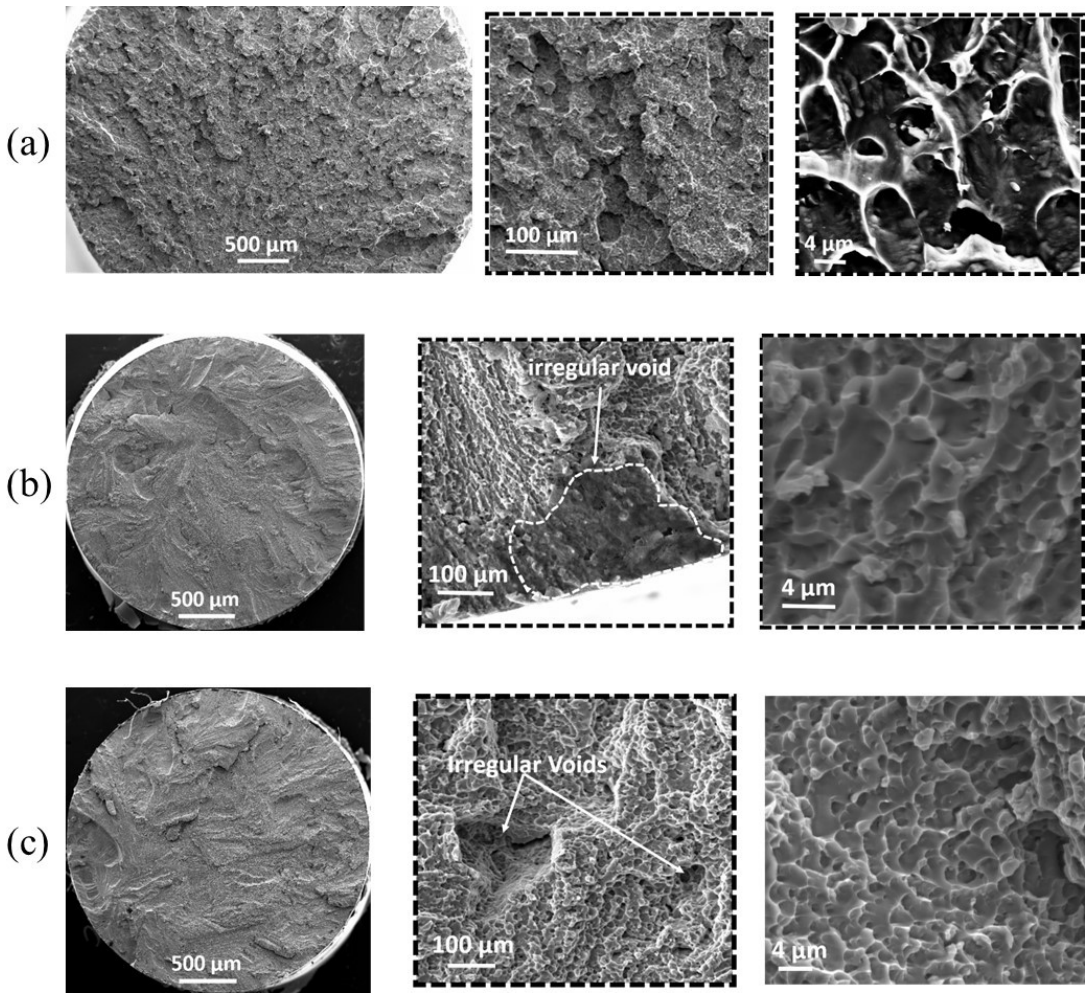

Figure 3.4 Fracture surfaces of tensile specimens for: (a) wrought, (b) AM HT1, and (c) AM HT2 exhibiting dimples as evidence of ductile fracture. Presence of larger and deeper dimples on the fracture surface of the wrought specimens may have contributed to the larger elongation to failure and ductility of wrought specimens.

Table 3.3 presents the tensile material properties, such as loading stress plateau and modulus of elasticity measured for wrought and AM specimens under monotonic loading. The results from monotonic tensile experiments demonstrate the austenite modulus (EA) of wrought material and AM HT1 specimen to be 73 GPa, while that for AM HT2 specimen was found to be lower and around 58 GPa. Obtaining a low austenite modulus of elasticity for the AM HT2 specimen, compared to HT1, indicates that the

modulus of elasticity, as well as other mechanical properties of NiTi such as stress plateau can be adjusted to desired, application-specific values. The ability to adjust mechanical properties of NiTi on application-specific values becomes promising, especially for the biomedical industry, knowing that the mechanical properties of AM NiTi may be adjusted to that of the human bone, providing a more durable, compatible, and effective implant. The modulus of the stress-induced martensite region (EM) for the wrought NiTi was reported to be ~ 22 GPa [31], while EM could not be measured for the AM material since the specimens fractured before reaching the fully martensitic region of the stress-strain curve. Furthermore, the stress-induced phase transformation appears to start at ~1.0% for all three sets of specimens.

Table 3.3 Tensile properties of wrought [31] and AM NiTi specimens used in this study.

Property	Wrought	AM HT1	AM HT2
Austenite modulus, E_A	73 GPa	73 GPa	58 GPa
A→M start stress, σ_S^{AM}	515 MPa	580 MPa	430 MPa
A→M start strain, ε_S^{AM}	1.0%	1.0%	1.0%

3.3.2 Cyclic Deformation Behavior

Stress-strain response of the first cycle of loading at different strain levels for both wrought and AM NiTi specimens are presented in Fig. 3.5. As shown for the wrought material, the stress-induced martensite start strain, ε_S^{AM}, is about 1.0% and the specimen exhibits a nearly perfect superelastic behavior, as it recovers all the applied strain with almost zero residual strain. Similarly, the first cycle responses of both AM NiTi specimens, heat-treated under two different thermal processes (*i.e*. HT1 and HT2),

illustrate a fully superelastic response, as presented in Figs. 3.5b and c. The superelastic behavior is at least valid for strain levels up to 2.0%. Analogous to the wrought specimen, the A→M start strain for both types of AM specimens appear to be around 1.0%.

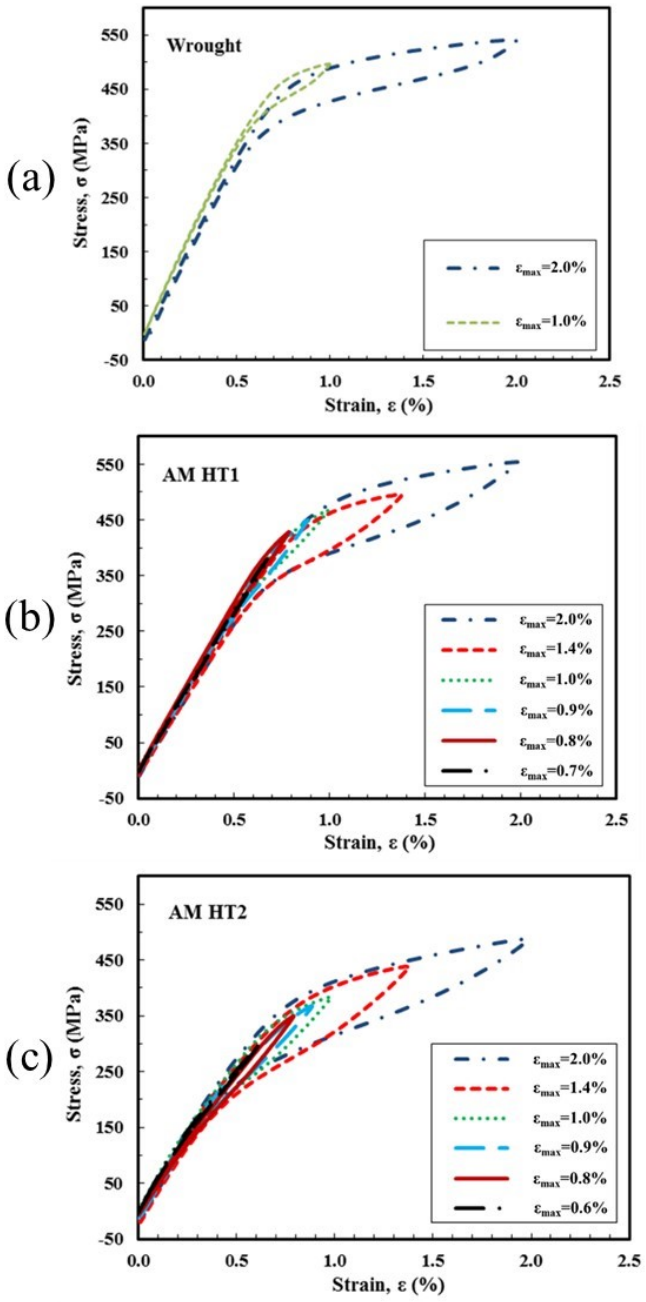

Figure 3.5 First cycle stress-strain response of NiTi at different maximum strain levels: (a) wrought [31], (b) AM HT1, and (c) AM HT2. All the specimens exhibit a nearly perfect superelastic behavior, as they recover all the applied strain with almost zero residual strain.

Similar to other metallic materials, cyclic deformation behavior of the superelastic NiTi evolves with increasing number of cycles of loading. However, the stress-strain

response reaches a stable state after a limited number of cycles (~150-200 cycles) as also reported in other studies for wrought NiTi [33,34]. The evolution of the cyclic stress-strain response for NiTi typically occurs in the form of change in stress-induced martensite start stress, σ_s^{AM}, the size of the hysteresis loop, and sometimes, accumulation of the residual strain. Furthermore, Mahtabi *et al*. [31] have also reported some cyclic stress hardening and mean stress relaxation for wrought superelastic NiTi and stated that the amount of stress hardening and mean stress relaxation were greater for tests with larger mean strains, where the volume fraction of the martensitic phase was larger.

Cyclic stress-strain responses of the first, tenth and mid-life cycles at ε_{max}=2.0% for three different NiTi alloys, employed in this study (*i.e*. wrought, AM HT1 and HT2), are presented in Fig. 3.6. According to Fig. 3.6, with increasing number of cycles of loading, a decrease in the A→M start stress (σ_s^{AM}) as well as an increase in the stress corresponding to the maximum strain (*i.e*. 2.0%) can be noticed for NiTi in all three conditions. Moreover, the area surrounded by loading and unloading paths, *i.e.* hysteresis loop, decreases with increasing number of cycles until the stress-strain response reaches a stable state. The increase in the stress range with increasing number of cycles of loading indicates a cyclic hardening behavior for both wrought and AM NiTi. For all the AM and wrought specimens, the amount of residual strain, probably due to the residual martensitic phase, at zero stress was not remarkable, as can be seen in Fig. 3.6.

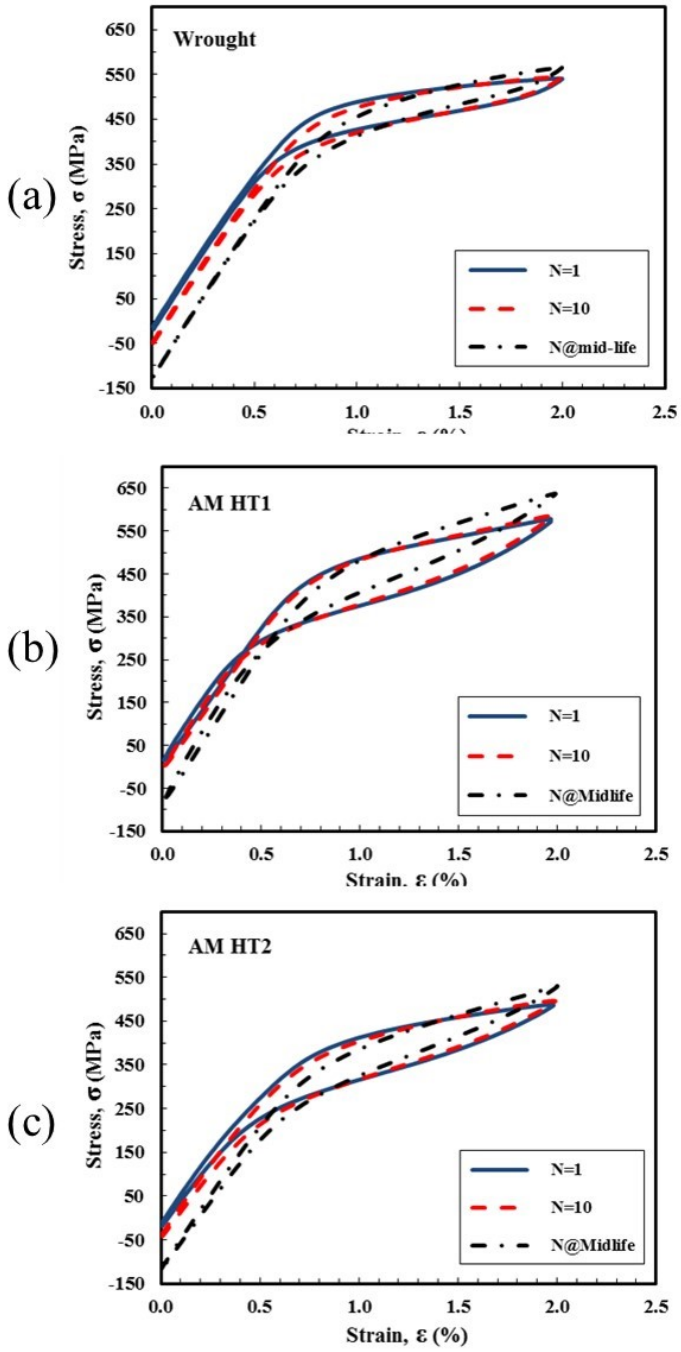

Figure 3.6 Cyclic stress-strain response at different cycles of loading for: (a) wrought [31], (b) AM HT1, and (c) AM HT2. For all the AM and wrought specimens, the amount of residual strain at zero stress was not remarkable.

First cycle stress-strain response at ε_{max}=2.0% for all three sets of specimens, including wrought, AM HT1 and AM HT2, are plotted in Fig. 3.7. As can be seen from

this figure, AM HT1 and wrought specimens have very similar stress levels (both A→M start stress, σ_s^{AM}, and maximum stress, σmax) with maximum stress level of AM HT1 being slightly higher than the wrought material. Unlike AM HT1 specimen, the AM HT2 specimen exhibits lower level of σ_s^{AM} and σ_{max} compared to the wrought counterpart. Adjusting the heat treatment to have AM NiTi specimens with two different stress levels provide the opportunity to interpret the experimental fatigue data with respect to stress as well as strain Mahtabi *et al*. [26] also suggests that the fatigue analysis of superelastic NiTi may yield different results in stress-life and strain-life approaches.

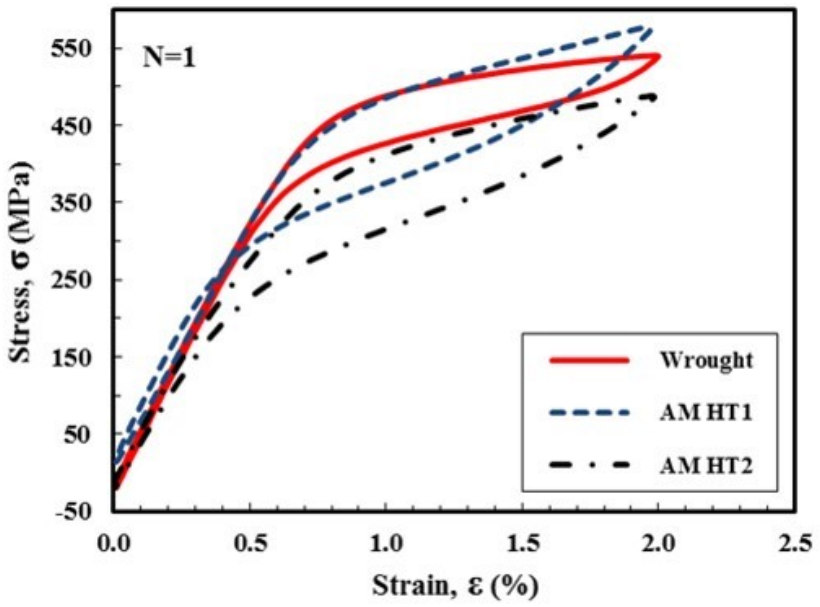

Figure 3.7 Comparison of the first cycle stress-strain response of wrought [31] and AM NiTi at ε_{max}=2.0%. AM NiTi specimens with two different stress levels are produced by adjusting the heat treatment, therefore, the experimental fatigue data with respect to stress as well as strain is interpreted.

3.4 Fatigue Behavior and Discussion

3.4.1 Fatigue Life Behavior

Results from constant amplitude strain-controlled fatigue experiments on wrought and two types of AM NiTi specimens (heat-treated at two different conditions) are presented in this section and discussed in the form of strain-life and stress-life approaches. Experimental measurements of the fatigue life and corresponding stress response at different strain amplitudes are listed in Table 3.4 for wrought [31], AM HT1 and AM HT2 NiTi. The values of the stress in this table are obtained from the stable cycle, measured near the mid-fatigue life of the specimen.

Table 3.4 Summary of the strain-controlled pulsating (R_ε =0) fatigue tests on AM and wrought NiTi.

	ε_{max} (%)	σ_{max} (MPa)	Reversals to Failure, $2N_f$
Wrought [31]	3.0	586	1,271
	3.0	577	1,487
	3.0	575	1,489
	2.0	562	3,542
	2.0	564	4,666
	2.0	570	4,920
	1.0	511	>216,410
AM HT1	2.0	610	634
	2.0	590	1,082
	1.4	553	3,706
	1.4	512	8,508
	1.0	475	24,266
	1.0	496	31,542
	0.9	461	38,922
	0.9	498	48,312
	0.8	450	510,428
	0.8	400	>814,574
	0.7	425	>1,541,420
AM HT2	2.0	533	1,394
	2.0	524	1,650
	1.4	500	8,930
	1.4	470	10,368
	1.0	414	25,382
	1.0	350	31,790
	0.8	310	>1,203,274
	0.6	297	>1,861,346

As can be seen in Table 3.4, AM specimens lasted longer than the wrought specimens, before they failed in the grip. As a result, the high cycle fatigue (HCF) data

for both types of AM specimens include longer fatigue lives, compared to the wrought material. Moreover, for larger strain levels (*i.e.* $\varepsilon_{max} > 1.0\%$), AM HT1 specimens exhibit higher stress response as compared to AM HT2 specimens.

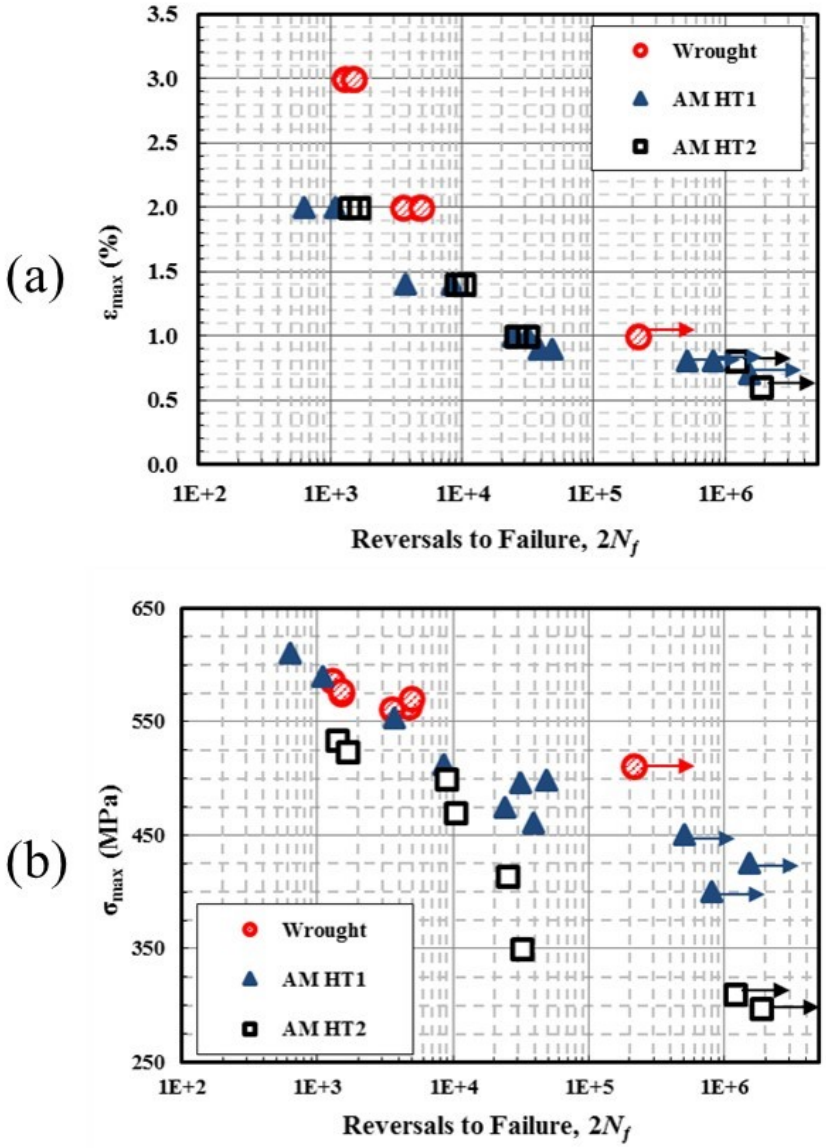

Figure 3.8 Comparison of pulsating (R_ε=0) fatigue behavior of AM and wrought [31] NiTi: (a) strain-life data and (b) stress-life data. Data points shown by arrow indicate failure in the grip.

Fig. 3.8a presents the strain-life (ε_{max}-N) data from strain-controlled fatigue experiments for the three batches of specimens investigated in this study. A run-out life of 10^5 cycles was considered in this study. Data points indicated by arrow are specimens that failed in the grip, demonstrating the actual fatigue life to be longer than that reported here. As can be seen from Fig. 3.8a, fatigue lives of both sets of AM specimens are shorter than those for wrought NiTi in both low cycle (*i.e.* larger maximum strains) and high cycle (*i.e.* smaller maximum strains) fatigue regimes. In short life regime, for instance, the average fatigue life at ε_{max} = 2.0% for wrought NiTi is a factor of two and six longer than the ones for AM HT2 and HT1 specimens, respectively.

In the HCF regime, however, the main challenge was the grip failure, probably due to the fretting fatigue, that limited the fatigue testing and did not allow continuation of the test to reach failure at the gage section. The grip failure was more pronounced for wrought specimens. Despite the fact that the HCF tests on wrought material are not available for very long lives (for example 10^6 cycles), the existing data confirm noticeably reduced fatigue lives of both AM HT1 and HT2 specimens compared to the wrought material (see the data points at ε_{max} = 1.0% in Fig. 3.8a). Comparing the AM NiTi specimens in strain-life plot (*i.e.* Fig. 3.8a), the HT2 specimens typically exhibit longer fatigue lives in short life regime, while fatigue lives of HT1 and HT2 specimens are similar in long life regime. The shorter fatigue lives of HT1 specimens in short life regime may be attributed to the higher stress response of AM HT1 specimens as compared to AM HT2 ones at higher strain levels, *i.e.* low cycle fatigue (LCF) regime, as seen in Fig. 3.7 and Table 3.4. Moreover, Table 3.4 shows that for duplicate tests, the one with larger stress response always yielded shorter fatigue life, which illustrates the

significant effect of the maximum stress level on the fatigue behavior of superelastic NiTi.

The stress-life fatigue data for wrought, AM HT1 and HT2 specimens are presented and compared in Fig. 3.8b. As can be seen from this figure, AM specimens, regardless of their heat treatment, yield shorter fatigue lives as compared to the investigated wrought NiTi, specifically in long life regime. In contrast to the strain-life behavior, the AM HT1 specimens show longer fatigue lives than AM HT2 specimens at the same stress level. Moreover, the AM HT1 specimen with ε_{max} = 2.0% that had the shortest fatigue life (*i.e.* $2N_f$ = 634 reversals) in strain-life plot (in Fig. 3.8a), appears to have a significantly larger stress level as compared to both wrought and AM HT2 specimens at the same strain level. The larger stress may explain the shorter fatigue life and indicate the coupling effects of strain and stress on fatigue behavior of superelastic NiTi. However, other influential factors, such as microstructural defects, may have also influenced the fatigue resistance of this specimen to some extent. The observed discrepancy in fatigue behavior of superelastic NiTi in stress-life and strain-life approaches was also reported in other studies [26,35]. Therefore, one may conclude that an appropriate fatigue damage model for superelastic NiTi should take into account the synergistic effects of stress and strain components on fatigue resistance, as discussed in detail by Mahtabi and Shamsaei [35].

3.4.2 Failure Analysis

Fracture surfaces of fatigue specimens fabricated by the employed AM technique were observed using scanning electron microscopy (SEM), and the crack initiation sites were investigated to determine the cause of fatigue failure in AM NiTi. Failure analysis

of the wrought fatigue specimens, corresponding to the data used in this study, was reported elsewhere [31]. In wrought material, small inclusion particles such as carbide and oxide particles, as shown in Fig. 3.9a, were observed to be present at the crack initiation sites. Fractography under SEM illustrated that the location and shape of the inclusion particles are very important factors, influencing the fatigue resistance of wrought superelastic NiTi.

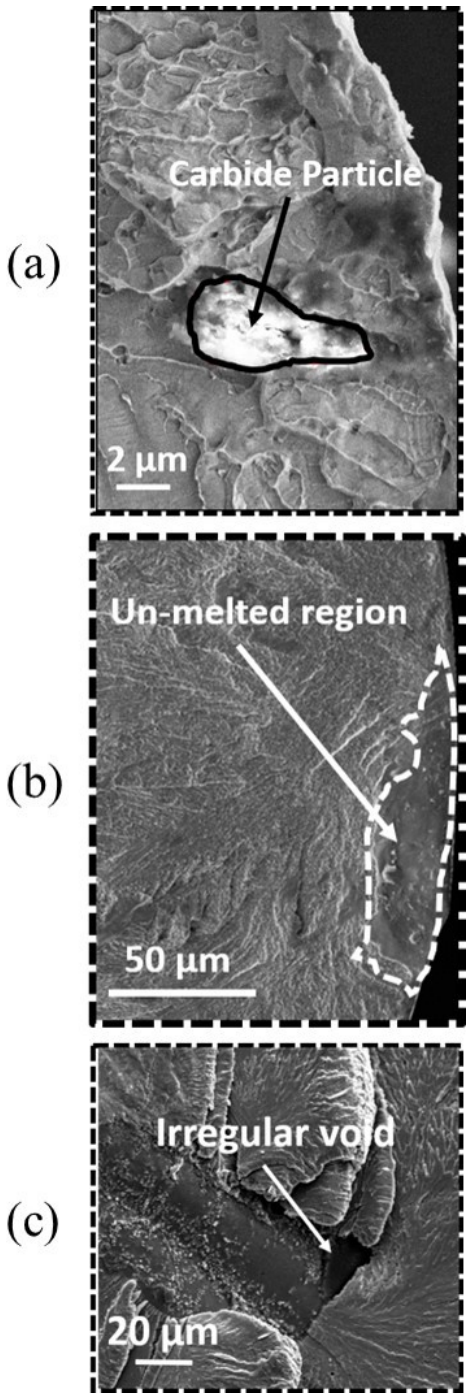

Figure 3.9 Magnified fracture surfaces of wrought (a), and two AM fatigue specimens (b and c) showing the presence of different types of defects at crack initiation sites. Spherical voids are formed from entrapped gas bubbles, generated by application of high laser energy to the melt pool, while irregular void, which are mostly un-melted regions, may be resulting from the lack of fusion and/or low laser penetration depth.

Spherical and irregular voids are the two common defect types observed on the fracture surface of AM NiTi specimens in this study, as shown in Figs. 3.9b and c, respectively. Spherical voids may be resulting from the entrapped gas bubbles, generated when a high laser energy is applied to the melt pool, whereas irregular void, which are mostly un-melted regions, can form due to the lack of fusion and/or low laser penetration depth. For AM parts, presence of various types of microstructural defects with different sizes, shapes, and at different locations (near surface or subsurface) provides various opportunities for the crack initiation [36]. The effects of surface roughness are reduced by machining and polishing the specimens in this study; however, the remaining interior voids and subsurface defects, located near the surface of the specimens, still have significant effects on accelerating the crack initiation. By machining and polishing the specimen's surface, subsurface voids may turn into very small notches on the polished surface, and contribute to the fatigue damage by inducing local stress concentrations [25].

For common metals, the presence of defects such as inclusion particles and voids causes stress concentration and increases the localized stress level, to a level typically larger than the yield strength of the material, resulting in localized plastic deformation. The larger stress level consequently leads to fatigue crack initiation under cyclic loading. For superelastic NiTi, however, the mechanism is different. The localized stress concentration results in a rise in the stress level that forms a localized stress-induced martensitic phase. Following unloading, the localized stress concentration will result in either residual martensitic phase, plastic deformation or a combination of both adjacent to the defect. Presence of plastic deformation and residual martensite may result in crack

initiation in superelastic NiTi caused by the sharp interfaces between austenite and martensite phases [37].

Fracture surfaces of two AM HT1 specimens, one from the HCF regime (*i.e*. low strain amplitude) and the other one from the LCF regime (*i.e*. high strain amplitude) are presented in Fig. 3.10. Generally, three main regions can be observed on all the fracture surfaces, corresponding to the different stages of the fatigue process: crack initiation, crack growth, and final fracture. Although the crack growth region is not very large for superelastic NiTi and majority of the fatigue life is devoted to the crack initiation stage, the size of the crack growth region depends on the fatigue testing regime (*i.e.* strain/stress amplitude) [27]. A larger crack propagation area can be observed at higher strain amplitudes (*i.e*. LCF regime), as shown in Fig. 3.10b, whereas for lower strain levels (*i.e*. HCF regime) a smaller crack growth area typically exists, as seen in Fig. 3.10a.

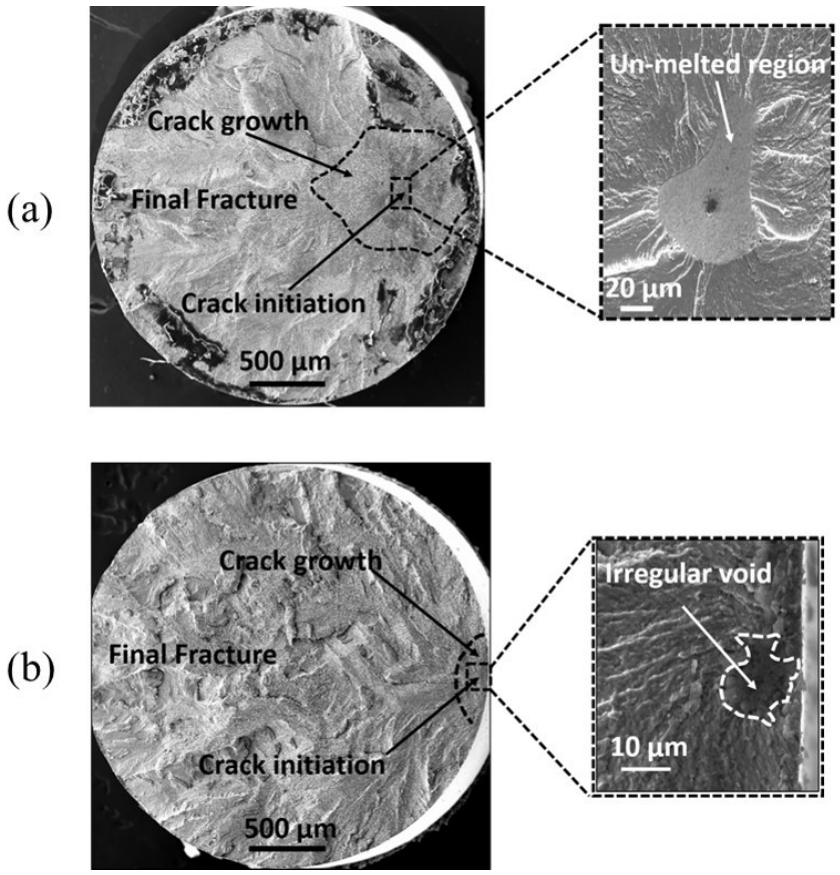

Figure 3.10 Scanning electron microscopy (SEM) images of fracture surfaces of two AM HT1 specimens: (a) a high cycle fatigue (HCF) specimen at ε_{max}=0.8% and $2N_f$ = 510,428 reversals, and (b) a low cycle fatigue (LCF) specimen at ε_{max}=2.0% and $2N_f$ = 634 reversals. At smaller strain amplitudes, HCF regime, a larger crack propagation area can be observed, whereas in higher strain levels, HCF regime, a smaller crack growth area is present.

For the HCF regime, ε_{max} = 0.8%, due to grip failure, fracture at the gage section was only achieved for one AM specimen from HT1 that had a fatigue life of 510,428 reversals. The corresponding fracture surface is shown in Fig. 3.10a and shows a subsurface defect (an un-melted region) with an approximate size of 55 µm located approximately 550 µm away from the surface. The fracture surface of the specimen tested in LCF regime (ε_{max} = 2.0%, $2N_f$ = 634 reversals), presented in Fig. 3.10b, shows a near surface irregular void with an approximate size of 14 µm to be responsible for crack

initiation. Although not statistically significant, observation may indicate that cracks tend to initiate from subsurface defects in the HCF regime and on-surface/close-to-surface defects in the LCF regime.

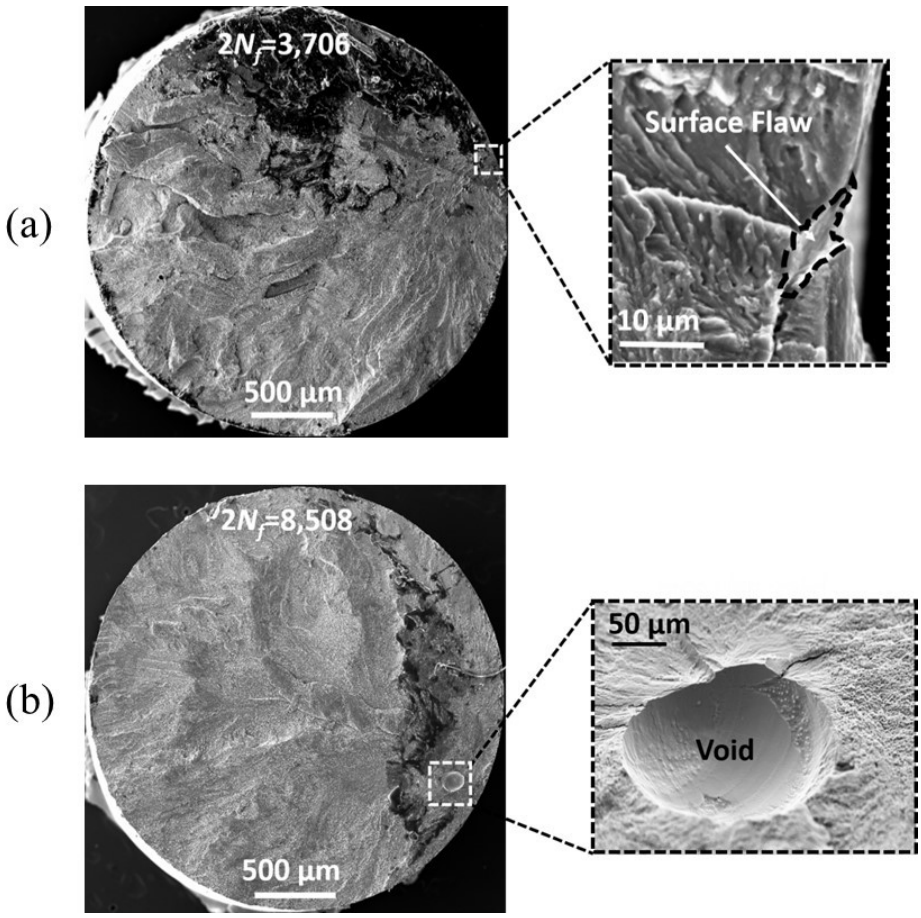

Figure 3.11 Scanning electron microscopy (SEM) images of fracture surfaces of two AM HT1 specimens tested at ε_{max}=1.4%, showing (a) a surface defect, and (b) a subsurface void at the crack initiation sites. One source of surface defects might be the subsurface irregular voids in as-fabricated rod that after machining the specimen are brought into the surface and turned into the surface defects.

Fig. 3.11a and b present crack initiation sites, corresponding to two AM HT1 specimens, both tested at 1.4% maximum strain, *i.e.* mid-cycle fatigue (MCF) regime. The surface defect in Fig. 3.11a with an approximate size of 7 µm may have been

generated due to the presence of subsurface irregular voids in as-fabricated rod that turned into a surface defect after machining the specimen. Fig. 3.11b illustrates a specimen with a subsurface void (approximately located 170 μm from the surface) with an approximate size of 140 μm. For irregular shape defects, the square root of the defect's area [38] was considered to approximate the size of the defect. Fatigue results demonstrate that the specimen with a surface irregular shape defect (Fig. 3.11a) has almost three times shorter fatigue life than the specimen with subsurface more regular shape defect (Fig. 3.11b), although the defect size in the latter specimen was significantly larger.

Noticeably different fatigue lives observed for the two specimens in Fig. 3.10 may be attributed to the differences in shape and locations of these defects serving as the crack initiation sites. When a crack forms near surface, it quickly reaches the free surface of the specimen under cyclic loading. On the free surface, the crack growth is generally accelerated, resulting in a shorter fatigue life. In addition, more irregular shape defects result in higher stress concentrations in their adjacent area, which in turn can accelerate the crack initiation process by increasing the amount of localized plastic deformation and/or residual stress-induced martensitic phase.

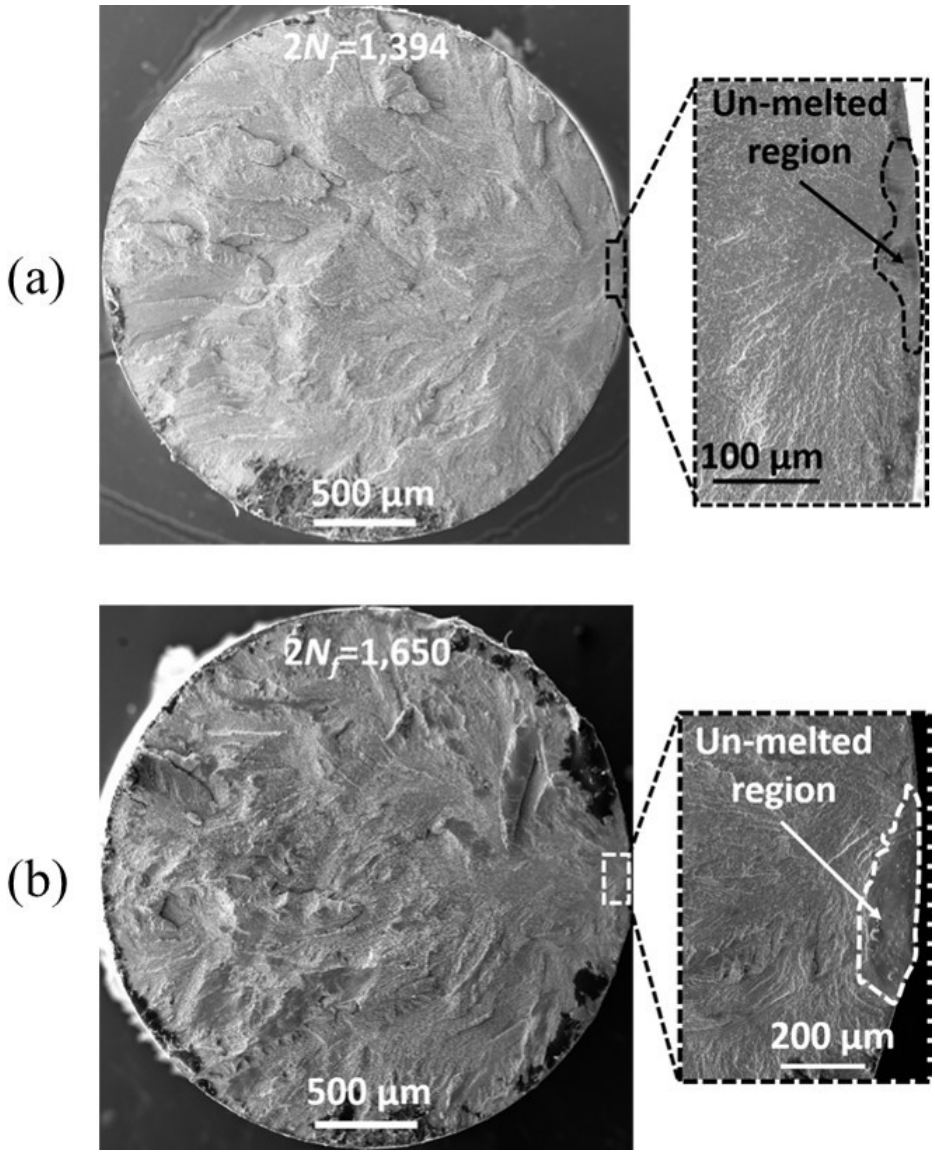

Figure 3.12 Scanning electron microscopy (SEM) images of fracture surfaces of two AM HT2 specimens tested in low cycle fatigue (LCF) at ε_{max}=2.0%, showing an un-melted region at the crack initiation site. The similar fatigue lives of these two specimens containing impurities with three times difference in sizes, may indicate the more dominant effect of the location of microstructural defect as compared to the size of the impurity, on the fatigue behavior.

Figs. 3.12a and b present crack initiation sites for two AM HT2 specimens, both tested in LCF regime (2.0% maximum strain) and having slightly different fatigue lives, *i.e*. $2N_f$ = 1,394 and 1,650 reversals. Table 3.4 shows that both specimens had similar

stress levels; the stress level of the specimen with shorter fatigue life being slightly higher. As can be seen in this figure, cracks have initiated from un-melted regions near the surface in both specimens. The un-melted regions in Figs. 3.12a and b have approximate sizes of ~ 65 μm and 190 μm, respectively. The comparable fatigue lives of these two specimens, while having impurities with three times different sizes, may indicate the location of the microstructural defect to be a more influential factor on the fatigue life than the size of the impurity. As mentioned earlier, the specimens broke at the grip in HCF tests of both AM HT1 and HT2, except for one AM HT1 specimen (Fig. 3.10a); thus, there were not any fracture surfaces for AM HT2 at the HCF regime to be investigated.

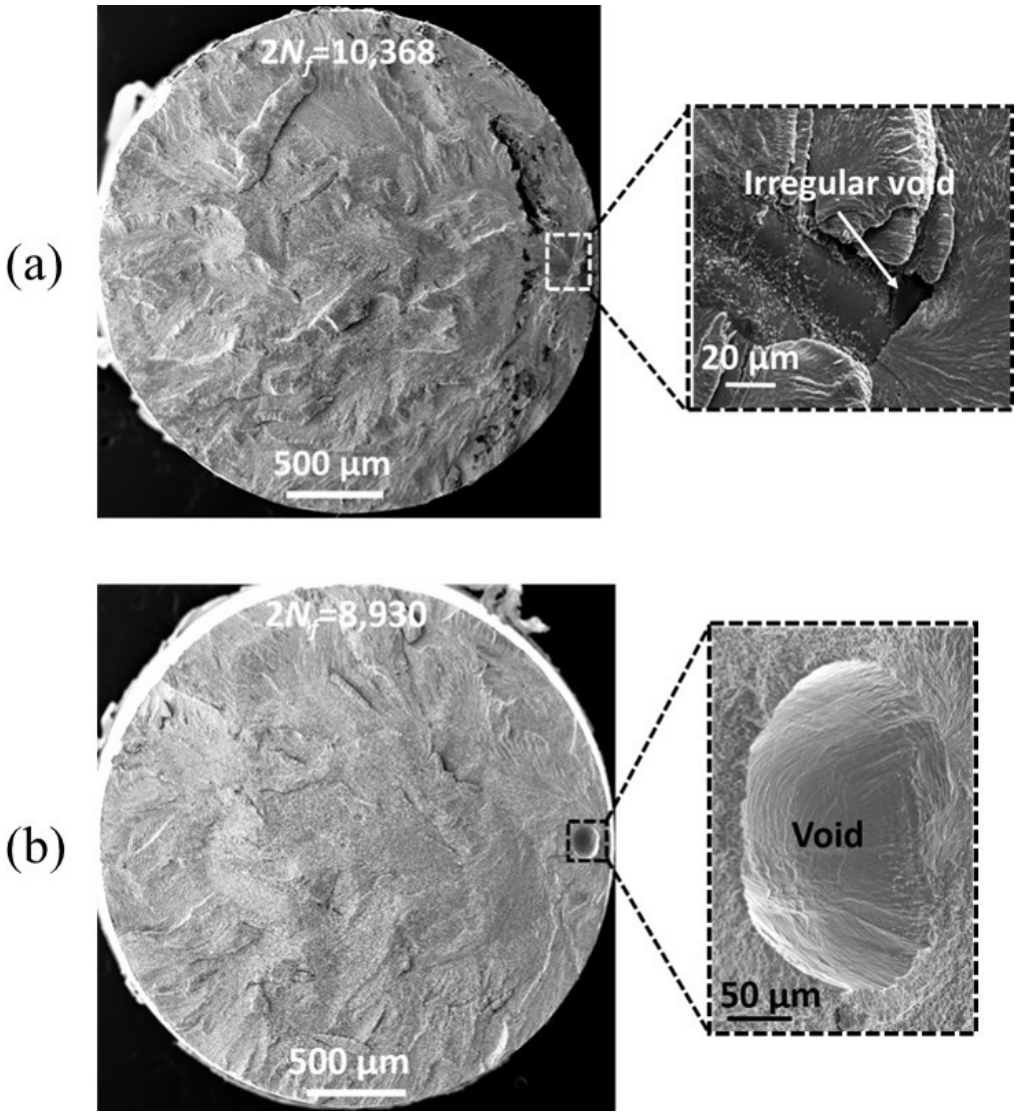

Figure 3.13 Scanning electron microscopy (SEM) images of the fracture surfaces of two AM HT2 specimens tested at ε_{max} = 1.4%, showing (a) a smaller irregular shape void, and (b) a larger regular shape void at crack initiation sites at different distances from the surface. Slightly different fatigue lives of these two specimens, while their defects are in size, shape, and location at the crack initiation sites, may indicate that the stress level and the defect's shape to be a more influential factor on the fatigue life than the defect's size.

Fracture surfaces of two AM HT2 specimens tested at 1.4% maximum strain, belonging to the MCF regime, are presented in Fig. 3.13. In both tests the cracks initiated from subsurface voids, approximately located at 180 µm and 105 µm from the surface, in

Figs. 3.13a and b, respectively. The corresponding voids have approximate sizes of 25 μm and 155 μm. Besides, the specimen with shorter fatigue life and a larger, more regular shape void had 6% larger stress level, as listed in Table 3.4. Therefore, slightly different fatigue lives observed for these two specimens, while having noticeably different defects (*i.e.* size, shape, location) at the crack initiation sites, may indicate the more dominant effects of the stress level and the defect's shape, as compared to the defect's size, on the fatigue behavior.

In order to study the effects of heat treatment on the fatigue behavior and damage mechanisms of AM NiTi specimens, the differences in fatigue life and the fracture surfaces of AM HT1 and HT2 specimens can be investigated. A comparison of the fracture surfaces of AM HT1 and AM HT2 specimens in the LCF regime, tested at 2.0% maximum strain, can be made from Fig. 3.10b and Fig. 3.12. Cracks in both specimens originated due to the near surface defects (irregular void for AM HT1 and un-melted region for AM HT2). AM HT2 specimens had longer fatigue lives which were more than twice as long than that of AM HT1 specimen. The longer fatigue lives of the AM HT2 specimens, while having larger defects at their crack initiation site, may be attributed to the lower stress levels of this specimens (average σ_{max} = ~ 530 MPa) as compared to the stress level of AM HT1 specimen (σ_{max} = 610 MPa).

Comparisons of the fatigue lives of AM HT1 and HT2 specimens tested at ε_{max} = 1.4% (*i.e.* MCF regime) can be made based on Figs. 3.11 and 3.13. Figs. 3.11a and 3.13a show two relatively small irregular shape voids at the crack initiation sites, the void on AM HT1 is located on the surface of the specimen, while the void on AM HT2 specimen is 180 μm away from the surface. The maximum stress values for AM HT1 specimen

(Fig. 3.11a) and AM HT2 specimen (Fig. 3.13a) are 553 MPa and 470 MPa, respectively. Since the AM HT1, in this case, has three times shorter fatigue life, while the void in AM HT2 is almost three times larger, one may conclude that the stress level and the defect's location have larger effects on the fatigue resistance of AM NiTi than the defect's size.

Similar microstructural defects (*i.e.*, voids) on both fracture surfaces in Figs. 3.11b and 3.13b are noticeable. Moreover, the stress levels of the two specimens are about the same (512 MPa for HT1 and 500 MPa for HT2). Therefore, the comparable fatigue lives (*i.e.* $2N_f$ = 8,508 and 8,930 reversals) obtained for these specimens can be explained by their similar fatigue related microscopic (such as defect's type, shape and location) as well as macroscopic (such as stress and strain levels) features. These observations as well as other analogies and differences reported before in Figs. 3.10 to 3.13, indicate that a reliable fatigue life prediction can be made by developing (or calibrating) a microstructure-sensitive model for fatigue analysis of AM NiTi, similar to the one utilized in references [39,40]. The microstructure-sensitive fatigue model should be able to account for the effects of microstructural features such as type, size, shape, and location of defects on the fatigue behavior. However, calibrating such models are cumbersome and requires extensive experimental and analytical efforts. On the other hand, based on Table 3.4, regardless of the size, shape, and location of the microstructural defect, fatigue life is always shorter for the duplicate specimen with higher stress response. Thus, stress may be the most influential factor on the fatigue behavior of superelastic NiTi, as also stated before by Mahtabi and Shamsaei [26].

Considering the fact that a major portion of fatigue life of superelastic NiTi is spent in the fatigue crack initiation stage, which mainly forms around the microstructural

defects such as voids. So, for fabricating more fatigue resistant AM NiTi parts, such defects should be minimized. Process parameter optimization in this study, similar to other investigations conducted on AM parts [25,41], was carried out to maximize the density, measured using Archimedes' principle, to get as close as possible to the density of wrought NiTi. Presence of the voids on the fracture surface of the fatigue specimens, as shown in Figs. 3.9 through 3.13, while having a very high density (99.8% of the wrought NiTi) can be due to two possibilities. Either there was a small number of voids in the as-fabricated AM NiTi rods, or the voids had very small volumes, and were most likely planar, similar to the ones shown in Fig. 3.12.

On the other hand, since the NiTi specimens fracture soon after the crack initiation occurs, even the presence of a few three-dimensional voids, serving as the crack initiation sites, may be enough to accelerate the fatigue failure of the AM NiTi specimens. Thus, presence of many planar-small volume voids or a few three-dimensional voids, while not greatly influencing the density of the part, can significantly reduce the fatigue resistance. Consequently, optimizing the process parameters for AM NiTi parts, based on density, as the only optimization objective, may not be adequate to improve their fatigue behavior. Further investigations are then needed to determine the appropriate AM process parameters for manufacturing NiTi parts, considering the effects of type, shape and size of possible microstructural defects on the fatigue behaviors, together with maximizing the density [25].

3.5 Conclusions

In this study, strain-controlled cyclic deformation and fatigue behavior of AM superelastic NiTi alloys were analyzed experimentally under pulsating (R_ε=0) cyclic

loads and the results were compared to wrought superelastic NiTi. The following conclusions can be drawn based on experimental observations and analyses performed:

1. Mechanical properties of AM NiTi, such as modulus of elasticity and loading/unloading stress plateaus, can be adjusted by appropriate heat treatment processes, *i.e*. combination of annealing and cooling steps. So, fabrication of NiTi parts with tailored mechanical properties for specific applications such as for bio-implants becomes possible.

2. Due to the presence of microstructural defects in AM NiTi specimens, they generally exhibited lower elongation to failure as compared to the wrought material.

3. Fatigue analysis of AM NiTi specimens may yield different results depending on the approach employed, *i.e*. stress-life of strain-life. Among AM specimens, AM HT2, with lower plateau stress, showed slightly longer fatigue lives in strain-life approach, while exhibited shorter fatigue lives in stress-life approach. Therefore, one can conclude that both stress and strain levels are influential factors on the fatigue behavior of the superelastic NiTi. As a result, depending on the application, *i.e*. load- or deformation-bearing, the fatigue analysis should be conducted utilizing either stress-life or strain-life approach.

4. Although machining and polishing can reduce the surface roughness and associated notch effects for AM NiTi specimens, some subsurface voids can come to the surface and form new surface flaws. These surface flaws are the desired locations for fatigue crack initiation.

5. AM NiTi specimens exhibited shorter fatigue lives, specifically in high cycle fatigue regime, as compared to the wrought material mainly due to the existence of microstructural defects.

6. Location, shape (irregular or spherical shape), and size of the defects were the main factors affecting the fatigue resistance of superelastic AM NiTi. Location and shape of the defect were found to be the most influential factors on the shorter fatigue lives observed for AM NiTi.

7. Optimizing the AM process parameters solely based on maximizing density, measured using Archimedes' principle, may not be appropriate to enhance the fatigue resistance of AM fabricated NiTi parts because most of the defects serving as the crack initiation site are planar voids (*e.g.*, un-melted regions), which do not significantly affect the measured density. As a result, an AM NiTi part with a density close to wrought NiTi may still contain microstructural defects that can be detrimental on the fatigue behavior.

3.6 References

[1] Duerig TW, Pelton A, Stöckel D. An overview of Nitinol medical applications. Mater Sci Eng A 1999;273:149–60.

[2] Pelton AR, Dicello J, Miyazaki S. Optimisation of processing and properties of medical grade Nitinol wire. Minim Invasive Ther Allied Technol 2000;9:107–18.

[3] Plotino G, Grande NM, Cordaro M, Testarelli L, Gambarini G. A review of cyclic fatigue testing of nickel-titanium rotary instruments. J Endod 2009;35:1469–76.

[4] Andani MT, Shayesteh Moghaddam N, Haberland C, Dean D, Miller MJ, Elahinia M. Metals for bone implants. Part 1. Powder metallurgy and implant rendering. Acta Biomater 2014;10:4058–70. doi:10.1016/j.actbio.2014.06.025.

[5] N.S. Moghaddam, M. Elahinia, M. Miller, D. Dean, Enhancement of bone implants by substituting nitinol for Titanium (Ti-6Al-4V): A modeling comparison, in: ASME 2014 Conf. Smart Mater. Adapt. Struct. Intell. Syst., American Society of Mechanical Engineers, 2014: p. V001T03A031–V001T03A031.

[6] Wu MH. Fabrication of Nitinol Materials and Components. Mater Sci Forum 2002;394–395:285–92. doi:10.4028/www.scientific.net/MSF.394-395.285.

[7] M. Drexel, G. Selvaduray, A. Pelton, The effects of cold work and heat treatment on the properties of nitinol wire, in: ASME 2007 2nd Front. Biomed. Devices Conf., American Society of Mechanical Engineers, 2007: pp. 89–90.

[8] Rahim M, Frenzel J, Frotscher M, Pfetzing-Micklich J, Steegmüller R, Wohlschlögel M, et al. Impurity levels and fatigue lives of pseudoelastic NiTi shape memory alloys. Acta Mater 2013;61:3667–86.

[9] Otsuka K, Wayman CM. Shape Memory Materials. Cambridge University Press; 1999.

[10] Hey JC, Jardine AP. Shape memory TiNi synthesis from elemental powders. Mater Sci Eng A 1994;188:291–300. doi:10.1016/0921-5093(94)90384-0.

[11] Bram M, Ahmad-Khanlou A, Heckmann A, Fuchs B, Buchkremer HP, Stöver D. Powder metallurgical fabrication processes for NiTi shape memory alloy parts. Mater Sci Eng A 2002;337:254–63. doi:10.1016/S0921-5093(02)00028-X.

[12] McNeese MD, Lagoudas DC, Pollock TC. Processing of TiNi from elemental powders by hot isostatic pressing. Mater Sci Eng A 2000;280:334–48. doi:10.1016/S0921-5093(99)00550-X.

[13] Chu CL, Chung CY, Lin PH, Wang SD. Fabrication of porous NiTi shape memory alloy for hard tissue implants by combustion synthesis. Mater Sci Eng A 2004;366:114–9. doi:10.1016/j.msea.2003.08.118.

[14] Zhang N, Babayan Khosrovabadi P, Lindenhovius JH, Kolster BH. TiNi shape memory alloys prepared by normal sintering. Mater Sci Eng A 1992;150:263–70. doi:10.1016/0921-5093(92)90120-P.

[15] Krone L, Schüller E, Bram M, Hamed O, Buchkremer H-P, Stöver D. Mechanical behaviour of NiTi parts prepared by powder metallurgical methods. Mater Sci Eng A 2004;378:185–90. doi:10.1016/j.msea.2003.10.345.

[16] Schüller E, Bram M, Buchkremer HP, Stöver D. Phase transformation temperatures for NiTi alloys prepared by powder metallurgical processes. Mater Sci Eng A 2004;378:165–9. doi:10.1016/j.msea.2003.10.341.

[17] Griffith ML, Keicher DL, Romero JA, Atwood CL, Harwell LD, Greene DL, et al. Laser engineered net shaping (LENS) for the fabrication of metallic components. Sandia National Labs., Albuquerque, NM (United States); 1996.

[18] Gu DD, Meiners W, Wissenbach K, Poprawe R. Laser additive manufacturing of metallic components: materials, processes and mechanisms. Int Mater Rev 2012;57:133–64. doi:10.1179/1743280411Y.0000000014.

[19] Shamsaei N, Yadollahi A, Bian L, Thompson SM. An overview of direct laser deposition for additive manufacturing; Part II: Mechanical behavior, process parameter optimization and control. Addit Manuf 2015;8:12–35. doi:10.1016/j.addma.2015.07.002.

[20] Bagheri A, Shamsaei N, Thompson SM. Microstructure and Mechanical Properties of Ti-6Al-4V Parts Fabricated by Laser Engineering Net Shaping. IMECE2015-51698, vol. 2A: Advanced Manufacturing, Houston: ASME; 2015, p. V02AT02A005-013. doi:10.1115/IMECE2015-51698.

[21] Bian L, Thompson SM, Shamsaei N. Mechanical Properties and Microstructural Features of Direct Laser-Deposited Ti-6Al-4V. JOM 2015;67:629–38. doi:10.1007/s11837-015-1308-9.

[22] Rafi HK, Pal D, Patil N, Starr TL, Stucker BE. Microstructure and mechanical behavior of 17-4 precipitation hardenable steel processed by selective laser melting. J Mater Eng Perform 2014;23:4421–8. doi:10.1007/s11665-014-1226-y.

[23] Sehrt JT, Witt G. Dynamic strength and fracture toughness analysis of beam melted parts. Proc. 36th Int. MATADOR Conf., Springer; 2010, p. 385–8.

[24] Stoffregen HA, Butterweck K, Abele E. Fatigue analysis in selective laser melting: review and investigation of thin-walled actuator housings. 25th Solid Free. Fabr. Symp, Austin, Texas: University of Texas in Austin; 2014.

[25] Yadollahi A, Shamsaei N, Thompson SM, Elwany A, Bian L. Effects of building orientation and heat treatment on fatigue behavior of selective laser melted 17-4 PH stainless steel. Int J Fatigue 2016. doi:10.1016/j.ijfatigue.2016.03.014.

[26] Mahtabi MJ, Shamsaei N, Mitchell MR. Fatigue of Nitinol: The state-of-the-art and ongoing challenges. J Mech Behav Biomed Mater 2015;50:228–54. doi:10.1016/j.jmbbm.2015.06.010.

[27] Robertson SW, Pelton AR, Ritchie RO. Mechanical fatigue and fracture of Nitinol. Int Mater Rev 2012;57:1–37.

[28] Mahtabi MJ, Shamsaei N. Multiaxial fatigue modeling for Nitinol shape memory alloys under in-phase loading. J Mech Behav Biomed Mater 2016;55:236–49. doi:10.1016/j.jmbbm.2015.10.022.

[29] ASTM B214−15. Standard test method for sieve analysis of metal powders. West Conshohocken, PA: ASTM International; 2011.

[30] ASTM E606 / E606M-12. Test method for strain-controlled fatigue testing. West Conshohocken, PA: ASTM International; 2012.

[31] Mahtabi MJ, Shamsaei N, Rutherford B. Mean Strain Effects on the Fatigue Behavior of Superelastic Nitinol Alloys: An Experimental Investigation. Procedia Eng 2015;133:646–54. doi:10.1016/j.proeng.2015.12.645.

[32] Yadollahi A, Shamsaei N, Thompson SM, Seely DW. Effects of process time interval and heat treatment on the mechanical and microstructural properties of direct laser deposited 316L stainless steel. Mater Sci Eng A 2015;644:171–83. doi:10.1016/j.msea.2015.07.056.

[33] Mahtabi MJ, Shamsaei N, Rutherford B. Mean Strain Effects on the Fatigue Behavior of Superelastic Nitinol Alloys: An Experimental Investigation. Procedia Eng 2015;133:646–54. doi:10.1016/j.proeng.2015.12.645.

[34] Miyazaki S, Imai T, Igo Y, Otsuka K. Effect of cyclic deformation on the pseudoelasticity characteristics of Ti-Ni alloys. Metall Trans A 1986;17:115–20.

[35] M.J. Mahtabi, N. Shamsaei, A modified energy-based approach for fatigue life prediction of superelastic NiTi in presence of tensile mean strain and stress, Int. J. Mech. Sci. 117 (2016) 321–333.

[36] Sterling AJ, Torries B, Shamsaei N, Thompson SM, Seely DW. Fatigue behavior and failure mechanisms of direct laser deposited Ti–6Al–4V. Mater Sci Eng A 2016;655:100–12. doi:10.1016/j.msea.2015.12.026.

[37] Tabanli RM, Simha NK, Berg BT. Mean strain effects on the fatigue properties of superelastic NiTi. Metall Mater Trans A 2001;32:1866–9. doi:10.1007/s11661-001-0164-0.

[38] Y. Murakami, Effects of small defects and nonmetallic inclusions on the fatigue strength of metals, JSME Int. J. Ser 1 Solid Mech. Strength Mater. 32 (1989) 167–180.

[39] McDowell DL, Gall K, Horstemeyer MF, Fan J. Microstructure-based fatigue modeling of cast A356-T6 alloy. Eng Fract Mech 2003;70:49–80.

[40] Torries B, Sterling AJ, Shamsaei N, Thompson SM, Daniewicz SR. Utilization of a microstructure sensitive fatigue model for additively manufactured Ti-6Al-4V. Rapid Prototyp 2016.

[41] Gu H, Gong H, Pal D, Rafi K, Starr T, Stucker B. Influences of energy density on porosity and microstructure of selective laser melted 17-4PH stainless steel. Proc. Solid Free. Fabr. Symp., 2013, p. 474–9.

[45] H. Mahabadipour, K.K. Srinivasan, S.R. Krishnan, A second law-based framework to identify high efficiency pathways in dual fuel low temperature combustion, Appl. Energy. 202 (2017) 199–212. doi:10.1016/j.apenergy.2017.05.154

CHAPTER IV

MICROSTRUCTURE-BASED MULTISTAGE FATIGUE MODELING OF ADDITIVE MANUFACTURED NITI USING LASER ENGINEERED NET SHAPING

(*To be summited to* International Journal of Fatigue)

The aim of this study is to predict the fatigue damage of Additively Manufactured (AM) NiTi using a microstructure-based MultiStage Fatigue (MSF) model. All the AM specimens were heat-treated under two different conditions (*i.e.* aging followed by air cooling and solution annealing followed by water quenching) to decrease their plateau stress. In order to study the cyclic deformation and fatigue behavior of heat-treated AM NiTi parts, specimens were subjected to strain-controlled constant amplitude pulsating fatigue experiments at room temperature (~24°C). Specimens were analyzed by Scanning Electron Microscopy (SEM) to establish the structure-property relations between the microstructure and cyclic damage. Fatigue crack initiation sites were associated with the presence of defects (*e.g.* voids, resulting from entrapped gas or lack of fusion) mostly close to the free surface of the specimens. The microstructural effects and mechanics of nucleation and growth observed in AM NiTi were studied via the MSF model. Results indicated that the fatigue behavior of superelastic NiTi was mostly influenced by the level of maximum stress and not the microstructural defects.

4.1 Introduction

NiTi (*i.e.* Nitinol) is an almost equiatomic alloy of nickel and titanium with two unique properties of shape memory and superelasticity/pseudoelasticity. NiTi has been widely used in applications in civil engineering, automotive, aerospace, and biomedical industries due to its shape memory [1] (its ability to recover the plastic strain after being heated to above a certain temperature), superelasticity [1] (its capability to recover strain levels up to 8% after being unloaded), and high resistance to severe environmental conditions [1,2]. Examples of NiTi applications in the biomedical industry are endovascular stents, endodontic files, and vena cava filters [1–3]. Furthermore, NiTi is a great candidate for producing bio-implants [4, 5] because of its unique mechanical properties and biocompatibility. However, the main challenge is the design and fabrication of implants to fit various geometries based on the individual patient.

Laser Engineered Net Shaping (LENS®) is a Direct Laser Deposition (DLD) Additive Manufacturing (AM) technique in which the metal powder is injected into a laser beam created melt pool to build parts with desired geometry. In the late 1990s, Sandia National Laboratories first developed LENS® technique [6], which provided new avenues for fabricating metallic materials with complex geometries that were difficult to fabricate using conventional manufacturing techniques. In the DLD process, a sliced Computer-Aided Design (CAD) model is used to fabricate components in a layer-by-layer fashion. The metal powder is injected into a molten pool created by a laser beam. The desired geometry is formed by repeating this process and adding consecutive layers along the height. Thus, the DLD process has been primarily used for rapid manufacturing and product repair due to its low cost, its ability to produce fine microstructures, and the

capability to fabricate functionally-graded compositions [7]. AM materials possess different microstructures, mechanical behaviors, and more importantly, fatigue properties as compared to their wrought counterparts [8]. Various process parameters, such as the laser power, beam travel speed, layer thickness, and powder feed rate can be adjusted to achieve different microstructures and mechanical properties [9]. Heterogeneous, porous, and anisotropic microstructures are created as a result of different thermal histories [8].

AM NiTi can also form several types of precipitates, including Ni4Ti3 and Ni3Ti particles, during heat treatment [10]. The presence of these precipitates can influence the martensitic phase transformation in NiTi, and subsequently affect the stress-strain behavior of the alloy [11]. Saeidi *et al*. [12] demonstrated that post-fabrication aging with precipitation hardening can improve the strength of a Selective Laser Melting (SLM) fabricated $Ni_{50.8}Ti_{49.2}$ alloy. Moreover, solution annealing of AM NiTi can form new precipitate particles in the material, which may improve the superelastic behavior of the alloy. Nishida *et al.* [13] suggested heat treatment as one of the most effective methods for controlling the transformation temperatures and increasing the strength of Ni-rich NiTi alloys. So, improved strength was attributed to the formation of Ni_4Ti_3, Ni_3Ti_2, and Ni_3Ti precipitates. Karaca *et al.* [14] indicated that the precipitate characteristics, such as size, volume fraction, and nearest neighbor distance, determined the strengthening in NiTi. According to their study, fine and coherent precipitates have a strengthening effect on the matrix and increase the thermal stability; however, there is a decrease in the transformation temperatures. Furthermore, shape memory properties of NiTi alloys, including matrix composition, transformation strain, and critical transformation stress, could be altered by precipitates. Sehitoglu *et al.* [15] showed that the cyclic deformation

of single crystal NiTi alloy was highly associated with the orientation and texture of the grains.

In general, monotonic mechanical properties of AM metallic materials (*e.g.* tensile, compressive strengths, hardness) are comparable to or even higher than their conventionally fabricated counterparts. Microstructural observations can be explained by the higher cooling rate during the AM process, which results in finer microstructures [16,17]. However, microstructural defects (*i.e.* voids and unmelted regions) present in AM components result in lower fatigue strengths compared to wrought materials [18–20]. Therefore, fabricating dense AM components with superior mechanical and fatigue properties via optimization of process parameters is of high importance [8]. Recently, AM technology has been predominantly used to produce NiTi components; however, uncertainty on the fatigue strength of these components is a barrier to the adoption of AM for load bearing applications [21].

Fatigue damage formation and progression occurs in four main stages: fatigue crack incubation (Inc), Microstructurally Small Crack (MSC) growth, Physically Small Crack (PSC) growth, and Long Crack (LC) growth [22]. The MSF model [23] was developed to predict fatigue damage associated with various microstructural features in cast alloys. The MSF model first employed parameters, such as microstructural inclusions (casting pores, oxide films, and silicon particles), porosity, Dendrite Cell Size (DCS), and Nearest Neighbor Distance of defects (NND), to predict fatigue damage in a die-cast Al356-T6 aluminum alloy [23]. Following McDowell *et al*. [23], studies have established that the combination of several factors (maximum pore size, DCS, and NND) were key microstructural features for fatigue damage in the cast A356 aluminum alloy

[24]. The MSF model was adapted to a high strength rolled aluminum alloys to extend the model applicability to wrought products of other aluminum alloys [25, 26]. Later, Xue *et al.* [49] applied the MSF model to an A380 aluminum alloy. Contrary to cast alloys, wrought products do not possess significant initial porosity. In the case of a 7075-T651 aluminum alloy, fatigue crack initiation sites were uniformly distributed intermetallics. The notch root plasticity effects of intermetallic particles were compared to the pores created during the casting using micromechanical simulations [27]. The MSF model was extended to account for other alloy systems, such as Hexagonal Close Packed (HCP) metals, specifically cast, and wrought magnesium alloys [27–30] and Ti-6Al-4V alloy [50]. In addition, when the MSF model was applied to LENS® processed steel [31], similar fatigue damage as cast alloys was observed, because the LENS® processed steel contains a significant number of pores similar or greater than cast specimens.

The correlation between manufacturing induced defects and fatigue resistances in the literature regarding AM NiTi is lacking and not well understood, mainly because the AM technique is a fairly new technology and many challenges are associated with the fatigue testing of NiTi specimens [21, 32]. Our paper aims to extend the MSF model to predict the fatigue damage in AM specimens using AM NiTi as a prototype. Because the structure-property relationships are incorporated into the MSF model, our goal is to use the MSF model to study the fatigue behavior of an AM material subjected to different heat treatments, which develop different microstructures.

4.2 Material and Experimental Methods

Spherical gas atomized NiTi powder (-100/+325 mesh), based on ASTM standard (ASTM B214−15, 2011), was used for the AM NiTi specimens. The powder

comprised 55% nickel and 43% titanium in weight percent (50.7% Ni- 48.6%Ti in atomic percent). Table 4.1 shows the chemical composition details of the powder.

Table 4.1 Chemical composition of NiTi powder utilized in this study.

Element	**O**	**Al**	**C**	**Fe**	**H**	**N**	**Cr**	**Ni**	**Ti**
Weight percent (%)	0.1	0.009	0.017	0.009	0.002	0.008	0.19	55.0	Balance

The powder was analyzed via SEM. In Fig. 4.1a, SEM images are presented indicating the spherical nature of powder. The particle size distribution is illustrated in Fig. 4.1b, showing that particle sizes ranged from 20 µm to 220 µm.

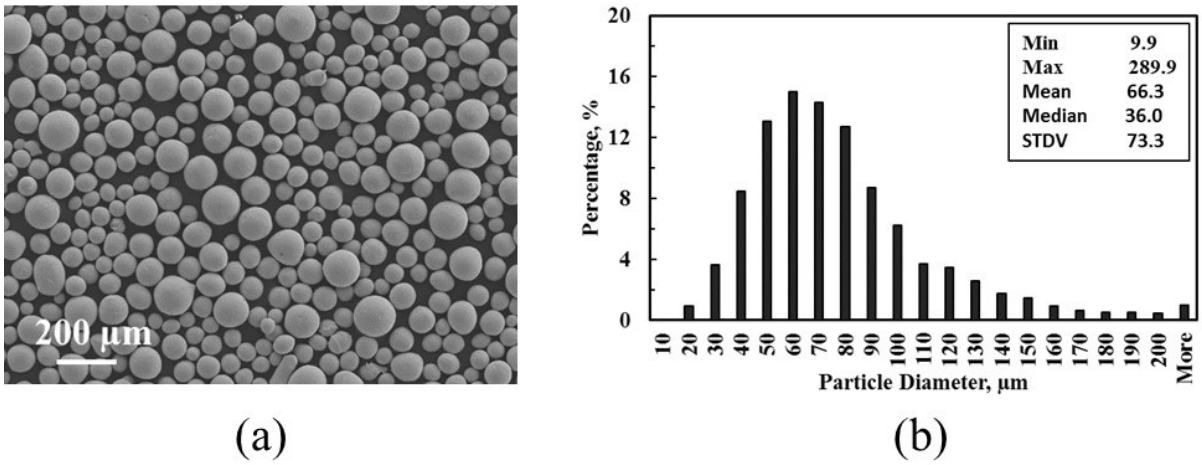

Figure 4.1 (a) Scanning Electron Microscopy (SEM) micrograph of NiTi powder and (b) particle size distribution of the powder.

The NiTi AM specimens were fabricated via an OPTOMEC LENS® 750 machine retrofitted with 1 kW laser source (Nd:YAG). As shown in Fig. 4.2a, the NiTi rods were manufactured one at a time (single-built), with a diameter of 8 mm and height of 80 mm, vertically on a pure titanium (grade 5) substrate. As Figure 4.2b and c show the rod was then machined into the fatigue specimens.

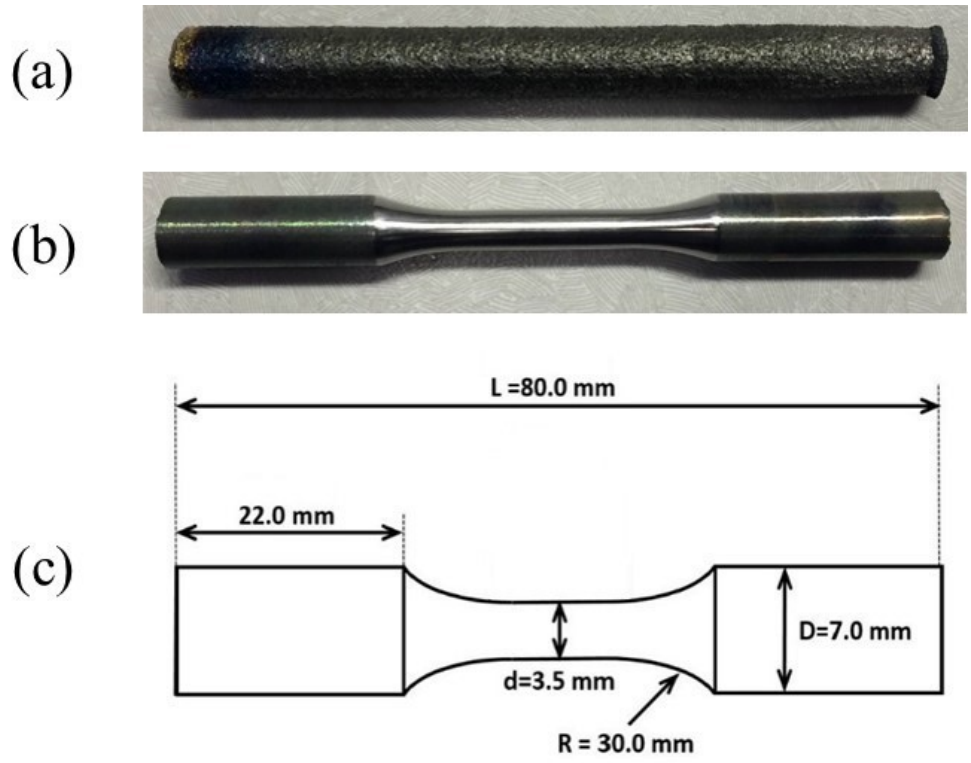

Figure 4.2 (a) As-built NiTi rod, (b) machined specimen, and (c) schematic of the fatigue specimen structure.

To keep the oxygen content in the AM processing chamber below 5 ppm, the chamber was purged with argon gas. The LENS® process parameters important in the fabrication of NiTi specimens are listed in Table 4.2, including laser power, scanning speed, powder feed rate, and layer thickness. These parameters were selected with the goal of obtaining a high level of density for the AM material compared to the wrought NiTi. Archimedes' principle was employed to calculate the density of the AM specimens. The process parameters were selected in a way to achieve 99.8% of the wrought NiTi density.

Table 4.2 Process parameters important in fabrication of NiTi specimens via Laser Engineered Net Shaping (LENS®).

Laser power (W)	Scanning speed (mm/s)	Powder feed rate (g/s)	Layer thickness (mm)
280	8.47	0.06	0.2

As-fabricated NiTi specimens were centered, in order to achieve two objectives: first, to provide a constant diameter over the length of the bar, and second, to make a smooth surface grip section. Subsequent machining was carried out on the centered bars to shape standard cylindrical specimens with a uniform gage section of 3.5 mm diameter, which is the ASTM standard for strain-controlled fatigue testing [34]. Fig. 4.2a shows a picture of the primary as-built NiTi rod, Fig. 4.2b presents a picture of the actual machined specimen, and Fig. 4.2c illustrates a schematic of the fatigue specimen structure showing the dimensions of different sections.

Machined cylindrical specimens were subjected to two different heat treatment conditions. Samples exposed to Heat Treatment 1 (HT1) were aged at 550 °C for 60 min and then cooled in air. Heat Treatment 2 (HT2) occurred in two steps: first, aging at 550 °C for 180 min and cooling in air, and second, solution annealing at 550 °C for 3 min and water quenching. Both heat treatments were chosen to produce a superelastic material at room temperature. The corresponding heat treatment conditions for the NiTi AM specimens were selected based on trial-and-error, in a way that the different plateau stresses were obtained for the two sets of specimens (*i.e.*, AM HT1 and AM HT2). As such, the fatigue behavior for the strain-life and stress-life approaches were readily investigated. In order to minimize the effects of surface flaws on the fatigue life, gage

sections were subjected to mechanical polishing. Sand paper was used to polish the specimens by hand (ranging from a rough level (grit #320) to a smooth level (grit #4000)). All experimental tests were conducted in air and at room temperature (~ 24 °C).

All monotonic tests on AM specimens were conducted under strain-controlled conditions until fracture occurred. Cyclic strain-controlled tests were conducted ($R_\varepsilon = \varepsilon_{min}/\varepsilon_{max} = 0$) using a MTS 858 uniaxial servo-hydraulic testing machine set at different maximum strain levels (*i.e.* ε_{max}= 0.6, 0.7, 0.8, 0.9, 1.0, 1.4, and 2.0%). For strain measurements, an MTS uniaxial extensometer with a gage length of 15 mm was used. All of the cyclic tests were conducted at a constant strain rate [31] of 0.036 s^{-1}. SEM was used to observe the fracture surface of the fatigue specimens and to study the crack initiation and progression characteristics.

4.3 Microstructure-Sensitive Approach

The MSF model is a microstructure-sensitive model that takes into account fatigue damage evolution at each stage, such as crack incubation (Inc), Microstructurally Small Cracks (MSC), Physically Small Cracks (PSC), and Long Cracks (LC) growth [23]. Detailed information, including the theoretical basis for the model, can be found in reference [23]. The total fatigue life N_{Total} is calculated by the following equation,

$$N_{\text{Total}} = N_{\text{Inc}} + N_{\text{MSC-PSC}} + N_{\text{LC}} \quad (4.1)$$

where N_{Inc} is the number of cycles to incubate a crack at a micronotch [23]. The two terms “micronotch” and “inclusion” share the same meaning, where the term “inclusion” refers to any microstructural defect present in a material – including second phase particles, intermetallic particles, and pores. The N_{MSC} term refers to the number of cycles needed for a microstructurally small crack (MSC) to propagate; N_{PSC} is the number of

cycles needed for a physically small crack (PSC) to propagate; and finally N_{LC} is the number of cycles needed for a long crack to propagate.

Crack incubation is followed by small crack growth at the micronotch up to about ½ D (D is inclusion size). The small crack growth (MSC) range consists of crack propagation with a crack length ranging from $a_i < a < k \times MS$ where a_i is the initial crack length, MS represents a characteristic length scale of interaction with microstructural (MS) properties, and k is a multiplier between 1 to 3 [23, 26].

Physically small crack (PSC) refers to the propagation of microstructural cracks with lengths ranging from $k \times MS < a < \sim$ (10 MS). The PSC regime length falls within 300μm to ~2–3 mm, based on the microstructural inclusion morphology and matrix texture.

The fatigue damage incubation life, N_{Inc}, is calculated by Equation 4.2 which is associated with the cyclic damage at the micronotch root. A modified Coffin–Manson law [23] was implemented at the microscale as shown below:

$$C_{Inc} N_{Inc}^{\alpha} = \beta = \frac{\Delta\gamma_{max}^{p^*}}{2} \tag{4.2}$$

where β refers to the nonlocal damage parameter around an inclusion, $(\frac{\Delta\gamma_{max}^{p^*}}{2})$ represents the local average maximum plastic shear strain amplitude, C_{Inc} is the linear coefficient for fatigue crack incubation, and β is its exponential counterpart. The numerical value for exponent α was chosen in a way to fall in the range of the macroscopic Coffin–Mason law [23]. The following relations are used to estimate the numerical value for β:

$$\beta = \frac{\Delta\gamma_{max}^{p^*}}{2} = Y[\varepsilon_a - \varepsilon_{th}]^q \qquad \frac{l}{D} \leq \eta_{lim} \tag{4.3}$$

$$\beta = \frac{\Delta\gamma_{max}^{p^*}}{2} = Y\left(1 + \xi\frac{l}{d}\right)[\varepsilon_a - \varepsilon_{th}]^q \qquad \frac{l}{D} > \eta_{lim} \tag{4.4}$$

In Equations 4.3 and 4.4, ε_a represents the remote applied strain amplitude, and ε_{th} refers to the value for the microplasticity threshold and can be determined by $\varepsilon_{th} = (0.29\sigma_{ult}/E)/(1\text{-}R)$; where E is Young's modulus, σ_{ult} is the ultimate strength, and R is the stress ratio. The ratio of the plastic zone over the inclusion area is subjected to the square root transformation which is described by the ratio $\frac{l}{D}$. In addition, the micromechanical simulations generate the q and ξ parameters [26]. The limiting ratio, η_{lim}, represents the transition from constrained to unconstrained micronotch root plasticity with regards to the applied strain amplitude [28]. The parameter Y [23, 26] is calculated by the equation $Y = y_1 + (1 + R)y_2$, where R is the stress ratio, where y_1 and y_2 are constant parameters. In the case of completely reversed loading conditions, Y is equal to y_1. Beside, when $(\frac{l}{D})$ hits the limits, some modification is performed on the parameter Y to take into account the geometric effects corresponding to the type of inclusion, the correlation is represented by the equation $\tilde{Y} = \left(1 + \frac{l}{d}\right)Y$. Therefore, different values for Y might be generated for a debonded particle and a pore of the same size [36]. The equation $(\frac{\Delta\gamma_{max}^{p^*}}{2})$ is used to calculate correlation of the plastic zone size taking into account the remote loading strain amplitude.

$$\frac{l}{D} = \eta_{lim}\frac{\langle\varepsilon_a - \varepsilon_{th}\rangle}{\varepsilon_{per} - \varepsilon_{th}} \qquad \frac{l}{D} \leq \eta_{lim} \tag{4.5}$$

$$\frac{l}{D} = 1 - (1 - \eta_{lim})(\frac{\varepsilon_{per}}{\varepsilon_a})^r \qquad \frac{l}{D} > \eta_{lim} \tag{4.6}$$

The parameter r is obtained from micromechanical simulations [36] and refers to the shape constant for the transition to limited plasticity [37, 38], and ε_{per} is the percolation limit [23] and is determined by ε_{per} =(0.8σ_y/E)/(1-R).

The MSC and PSC functions were combined into a single mathematical form in McDowell *et al.* [23]. The local driving force for the MSC/PSC crack growth is driven by the range of crack tip displacement, ΔCTD, which is proportional to the crack length. Furthermore, in the High Cycle Fatigue (HCF) regime, the crack growth also depends on the n_{th} power of the applied stress amplitude, σ_a^n, while, in low cycle fatigue (LCF) crack growth is correlated with macroscopic plastic shear strain range, $(\frac{\Delta\gamma_{max}^{p^*}}{2})$, which is calculated by the following equations.

$$\left(\frac{da}{dN}\right)_{MSC} = \chi(\Delta\mathrm{CTD} - \Delta\mathrm{CTD}_{th}) \qquad a_i = 0.625D \qquad (4.7)$$

$$\Delta\mathrm{CTD} = \mathrm{C}_{II}\left(\frac{\mathrm{GS}}{\mathrm{GS}_0}\right)^{\omega}\left(\frac{\mathrm{GMO}}{\mathrm{GMO}_0}\right)^{\psi}\left[\frac{U\Delta\sigma}{S_{ut}}\right]^{\xi} a_i + \mathrm{C}_I\left(\frac{\mathrm{GS}}{\mathrm{GS}_0}\right)^{\omega'}\left(\frac{\mathrm{GMO}}{\mathrm{GMO}_0}\right)^{\psi'}\left(\frac{\Delta\gamma_{max}^{p^*}}{2}\right)^2 \qquad (4.8)$$

where χ represents a constant specific value for a given microstructure whose numerical value is typically less than one and is equal to 0.32 for several different alloys [26]. The parameter, a_i, refers to the initial crack length. GS and GS_0 are grain size and reference grain size, respectively. C_I, C_{II}, and ξ are material dependent parameters that are used to correlate the microstructural effects with the MSC growth [23, 26]. The Burgers vector for the matrix is used to set the threshold value for crack tip displacement. The term $\Delta\hat{\sigma}$ is the combination of the uniaxial effective stress amplitude, $\sigma = \sqrt{\frac{3}{2}\frac{\Delta\sigma'_{ij}}{2}\frac{\Delta\sigma'_{ij}}{2}}$, and the maximum principal stress ranges, $\Delta\sigma_1$, and is calculated by the relation $\Delta\hat{\sigma} = 2\theta m\bar{\sigma}_a + (1-\theta)m\Delta\sigma_1$, with θ falling within $0 \leq \theta \leq 1$ [38]. θ is a weighting parameter in a way that

von Mises stress state is resulted when the θ=1. The Schmid factor, m, falls within $0 \leq m \leq 0.5$ accounts for the slip plane and the slip direction of the stressed material and is quantified from the grains orientations. The load ratio effects are considered by employing the parameter U, which is calculated by the equation $U = \frac{1}{1-R}$ [36]. In this study, the ratio of the grain size to the reference size, $(\frac{\mathrm{GS}}{\mathrm{GS_0}})^{\omega \, or \, \omega'}$, was calculated for all AM specimens to investigate the effect of grain size on small crack growth (ω or ω' is a material parameter; GS_0 and GS represents the reference grain size and specific grain size, respectively) [26]. Also, the ratio of the grain misorientation to the reference misorientation, $(\frac{\mathrm{GMO}}{\mathrm{GMO_0}})^{\psi \, or \, \psi'}$, for all specimens was employed to study the correlation between the grain misorientation and small crack growth, where GMO_0 is the reference grain misorientation, GMO is the specific grain misorientation, and ψ or $\psi'$is a material parameter.

Classical Linear Elastic Fracture Mechanics (LEFMs) is applicable to the MSF model for long crack growth stage [23]. However, similar to Jordon *et al*. [24,29,37], the modeling approach discussed here is centered on the concept of incubation and MSC/PSC regimes. Experimental data has validated that MSC/PSC can predict fatigue cracks as long as several millimeters [23].

4.4 Results and Discussion

4.4.1 Microstructure Behavior

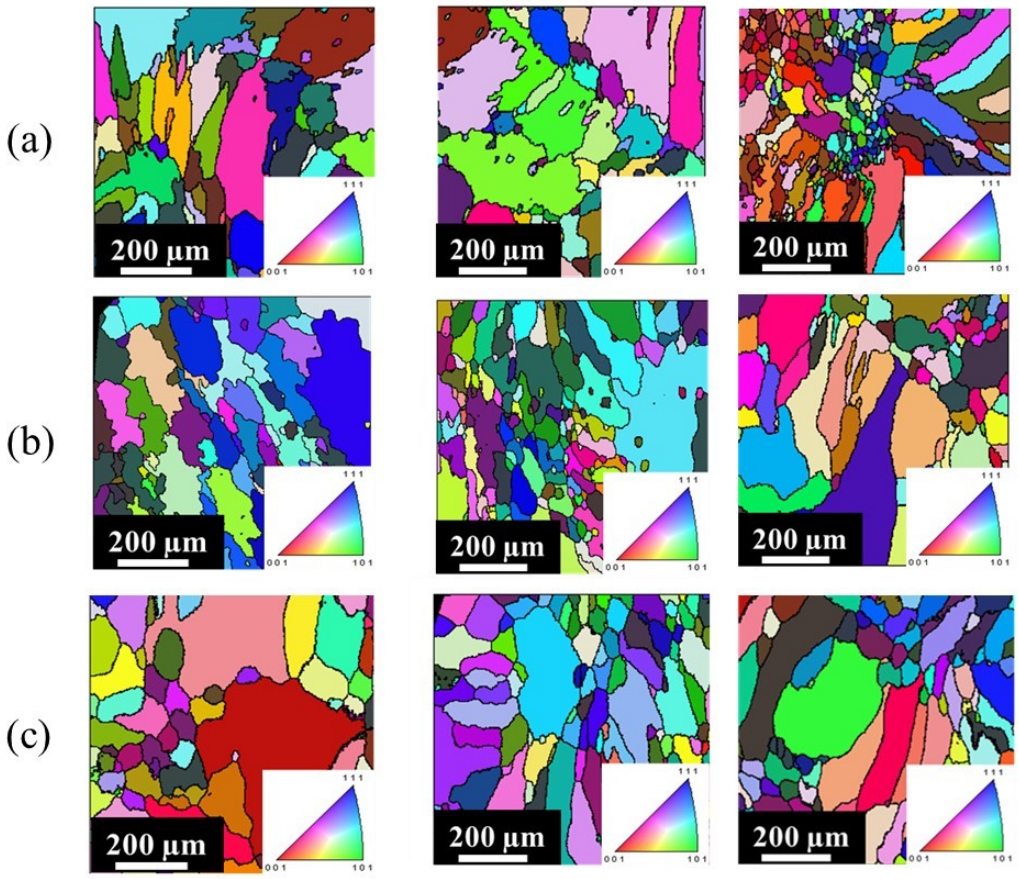

Figure 4.3 Electron backscatter diffraction (EBSD) colored map of microstructure of (a) AM as-built specimens (b) AM HT1, (c) AM HT2 indicating the grain shape, size, and orientation. The larger grain size observed in AM HT1 is due to the lower cooling rate experienced by AM HT1 parts after annealing (cooled in air).

Microstructure of the as-built and heat-treated AM NiTi specimens are shown in Fig. 4.3. Shown in Fig. 4.3a, grains in as-built AM NiTi are distributed over the section of the specimen with an average grain size of ~13 µm. In Fig. 4.3b, AM HT1 specimens possess significantly larger grain sizes with an average grain size about 23 µm. The lower cooling rate after annealing (cooled in air) explains a larger grain size observed in AM

HT1 specimens. In contrast to the AM HT2 specimens, which were quenched in iced water after heat treatment, the AM HT1 grain sizes were greater due to the high cooling rate as depicted in Fig.4.3c. The average grain size of the specimens subjected to AM HT1 was about 17 μm and for AM HT2 was 23 μm as shown in Table 4.3. As the fabrication process for all AM specimens, including as-built, AM HT1 and HT2 specimens were exactly the same, all AM specimens should have similar microstructures prior to heat treatment as shown in Fig. 4.3a. Therefore, the observed different microstructures of these two heat treated AM specimens is attributed to the impact of different heat treatments.

The Electron Backscatter Diffraction (EBSD) images are cleaned to represent the data with confidence index above 0.1. The grain boundaries shown in Fig. 4.4c,d are separated with at least a five degree misorientation angle.

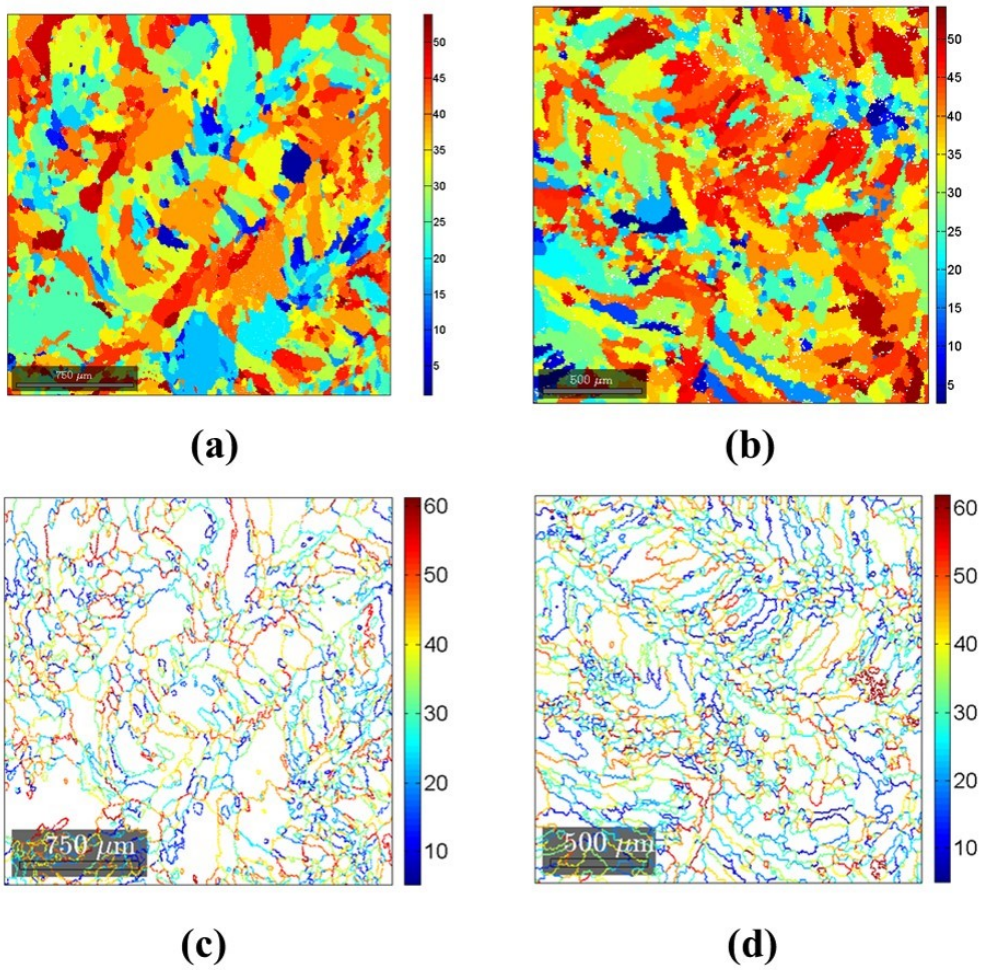

Figure 4.4 Electron backscatter diffraction (EBSD) Grain boundary maps of (a) AM HT1, (b) AM HT2, grain boundary map of (c) AM HT1 and (d) AM HT2 specimens indicating the grain shape, size, and orientation. The stress concentration at the grain boundaries caused by martensitic transformation is an influential factor in the fatigue behavior of NiTi alloys due to its ability to initiate the plastic deformation, thus assisting crack incubation.

The microstructural properties, such as grain size, mean orientation, average misorientation, and other grain boundary properties were analyzed. According to the literature, these microstructural properties have significant effects on the fatigue behavior of the NiTi alloys [39]. The effect of grain size on the fatigue behavior of NiTi alloys as reported by [40,41] suggests that a decrease in grain size increases the fatigue resistance. The fatigue behavior of Nitinol alloys depends on the stress concentrations at grain

boundaries caused by martensitic transformations, which initiate plastic deformation, thus assisting crack incubation [21].

In addition, Figs. 4.4d show that greater angle oriented grains had a much larger impact on annealing and tended to grow laterally with respect to the direction of the laser beam. Low angle oriented grains with small grain sizes were found in the Heat Affected Zone (HAZ). The volume fraction of martensitic particles present was 1.2% for aged specimens and 2.4% for aged and annealed specimens. The annealed specimen showed a more homogenous distribution of martensite particles. Fig. 4.4c and d show the grain boundaries for each of the NiTi specimens with the misorientation angle between them represented by the color change from blue (low angle) to red (high angle).

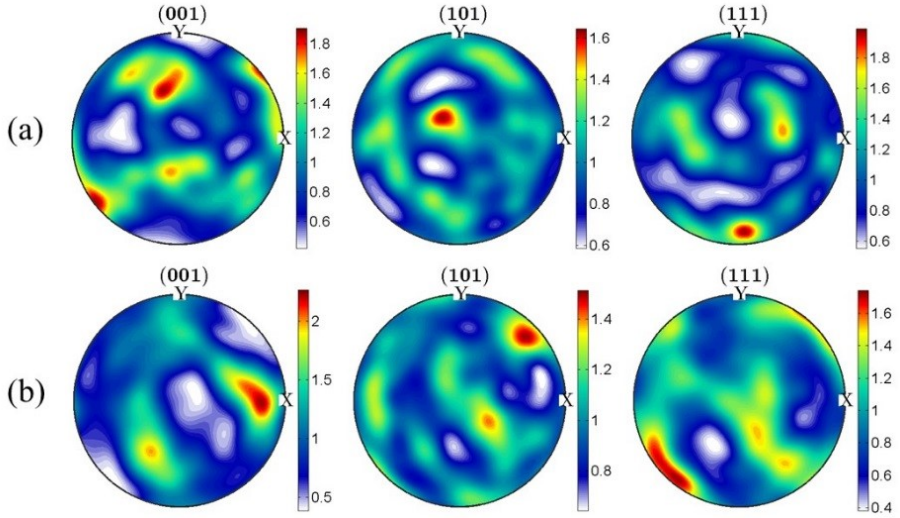

Figure 4.5 Electron backscatter diffraction (EBSD) orientation maps for angular pole of (a) aging and (b) aging plus annealing specimens.

In Fig. 4.5, the pole figures for (001), (101), and (111) are shown for the AM heat treated NiTi specimens. The AM HT1 specimen was highly textured with (101) and (111)

fibers along a certain axis. However, for the AM HT2 specimen, a highly textured pole figure with strong (001) and (111) fibers were observed.

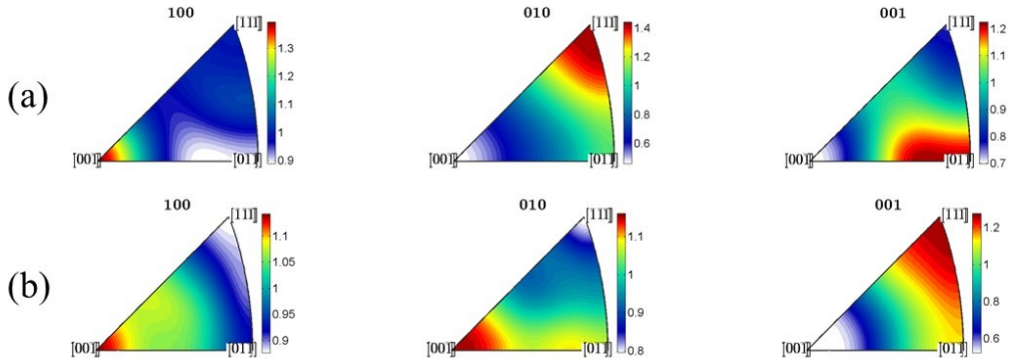

Figure 4.6 Electron backscatter diffraction (EBSD) orientation maps for inverse angular pole of (a) AM HT1 and (b) AM HT2 specimens.

The inverse pole figure in Fig. 4.6a showed a similar behavior with (101) and (111) fibers strongly textured along the yz-plane for the aged specimen. for AM HT2 specimen, the (001) fiber tended to be aligned along xy-plane and (111) fiber textured along the z-direction. A relatively strong <111> texture was previously observed along the rolling/drawing direction [42].

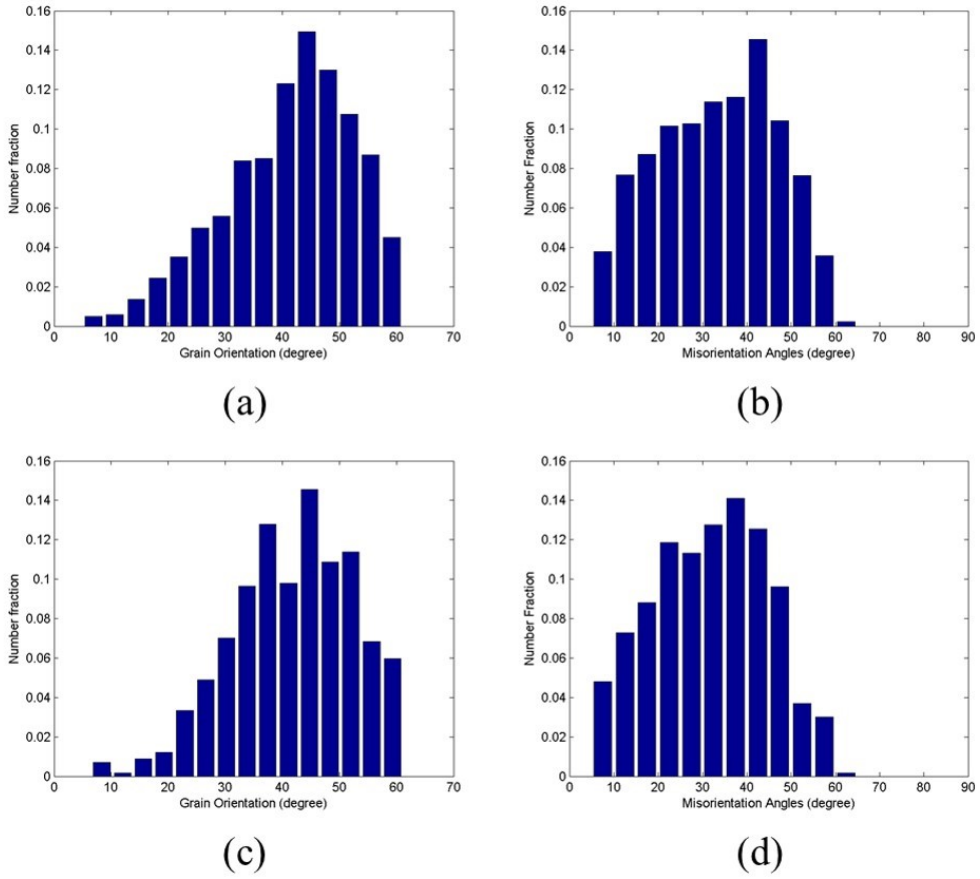

Figure 4.7 Comparison of orientation distribution in first column and misorientation angle in second column vs number fraction of (a, b) AM HT1 and (b, c) AM HT2 specimens. The fatigue crack growth rate decreases by increasing the misorientation angle due to the increased hindrance to the dislocations emitted by the crack tip along the grain boundaries.

Fig. 4.7 shows the grain orientation distribution and the misorientation angle distribution for both cases of heat treated AM NiTi specimens. Both the grain orientation and the misorientation angle distributions are somewhat Gaussian. The average value of the misorientation angle is 33.3 degrees for the aged specimens and 31.7 degrees for the annealed specimens. A recent study [43] shows that an increase in the misorientation angle reduces the fatigue crack growth rate in nanocrystalline materials, because of the

increased resistance to the dislocations emitted by the crack tip along the grain boundaries.

The average values of the microstructure properties for both heat treated AM specimens are presented in Table 4.3. The average grain size for the AM HT2 specimen is ~1.3 times greater compared to the AM HT1 specimen. As observed in Eq. 4.4, the grain size has a significant impact on determining the crack growth rate. The average of mean values for grain size, grain orientation and grain misorientation of AM HT1 and AM HT2 specimens were calculated and used as a reference value in the MSF model. Similarly, the mean values of grain size and grain orientation were used as the observed values. The annealing process had a significant effect on the grain size distribution of the AM specimen. There are no significant differences between the average misorientation angles of AM HT1 and AM HT2 specimens.

Table 4.3 Summary of microstructural properties obtained from electron backscatter diffraction (EBSD) data for aged and aged annealed specimens.

Microstructural properties	**AM HT1**	**AM HT2**	**Reference values**
Mean grain size	17 μm	23 μm	20 μm
Mean misorientation angle	33.3 °	31.7 °	32.5 °
Mean grain orientation angle	41.2 °	41.8 °	41.5 °

The microstructural properties have a great influence on the crack incubation and small crack growth stages in the MSF model [21]. The grain level properties drive the initial fatigue behavior of the material, which can be obtained through the microstructural analysis. The crack tip displacements were calculated by Eq. 4.4 and were directly correlated with their microstructural properties. The ΔCTD for an AM HT1 specimen

differs from the ΔCTD for AM HT2 specimen because of microstructural features, such as grain size, grain misorientations, and grain distribution. In addition, the heterogeneous grain orientation distribution observed in the microstructure, presented in Fig. 4.3, should define the differences in fatigue behavior. A crack with the incubation in the region of smaller grains and crack growth in the region of larger grains will have a lower number of cycles than the crack incubated at larger grain and growing through the region of smaller grains. In the current MSF model, only the microstructural properties related to grain size and grain orientation have been incorporated.

4.4.2 Strain-Life Results

Fig. 4.8 presents the strain-life (ε_{max}-N) data generated from strain-controlled fatigue experiments on the AM specimens. In this study, a run-out life of 10^6 cycles was used in this analysis. In Fig 4.8, data pointed by an arrow represent specimens that failed in the grip, which means that their actual fatigue life was longer than what is reported here.

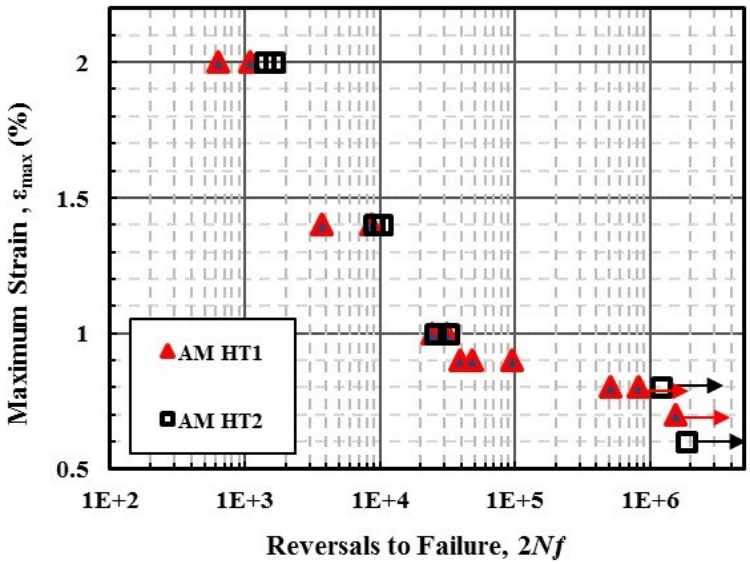

Figure 4.8 Scatter plot comparing the pulsating (Rε=0) fatigue behavior of AM HT1 and AM HT2 specimens. At higher strain levels in the low cycle fatigue (LCF) regime, AM HT1 specimens exhibit lower fatigue life compared to the AM HT2 specimens, which is due to the higher stress response in the AM HT1 specimens.

Grip failure was the main challenge in the HCF regime, which may be attributed to fretting fatigue. According to the strain-life plot, shown in Fig. 4.8, the AM HT2 specimens typically exhibited longer fatigue lives in the Low Cycle Fatigue (LCF) regime. However, comparing fatigue lives of HT1 and HT2 specimens in the High Cycle Fatigue (HCF) regime, the fatigue lives were similar. The AM HT1 material exhibited a lower fatigue life than AM HT2 material in the LCF regime, because under a strain-controlled test, the stress in the AM HT1 specimens was greater as per the stress-strain behavior illustrated in Fig 4.9.

Table 4.4 Summary of the data for strain-controlled pulsating (R_ε =0) fatigue test on AM specimens.

	ε_{max} (%)	σ_{max} (MPa)	Reversals to Failure, $2N_f$	Defect Type	Defect Size (μm)
AM HT1	2.0	610	634	Irregular void	14
	2.0	590	1,082	-	-
	1.4	553	3,706	Surface flaw	7
	1.4	512	8,508	Regular void	140
	1.0	475	24,266	-	-
	1.0	496	31,542	-	-
	0.9	461	38,922	-	-
	0.9	498	48,312	-	-
	0.8	450	510,428	Un-melted	55
	0.8	400	>814,574	-	-
	0.7	425	>1,541,420	-	-
AM HT2	2.0	533	1,394	Un-melted	65
	2.0	524	1,650	Un-melted	190
	1.4	500	8,930	Regular void	155
	1.4	470	10,368	Irregular void	25
	1.0	414	25,382	-	-
	1.0	350	31,790	-	-
	0.8	310	>1,203,274	-	-
	0.6	297	>1,861,346	-	-

Table 4.4 also shows clearly that shorter fatigue lives were always attributed to the greater stresses demonstrated in the fatigue behavior of the superelastic NiTi.

4.4.3 Stress-Life Results

Fig. 4.9 presents the stress-life fatigue data for AM HT1 and AM HT2 specimens. Contrary to what was observed for strain-life behavior, the fatigue life for AM HT1 specimens were greater than the AM HT2 specimens at the same stress level. The fatigue

resistance of this specimen may have been affected by other influential factors as well, such as microstructural defects. Other studies have also reported the discrepancy in fatigue behavior of superelastic NiTi in stress-life and strain-life approaches [21].

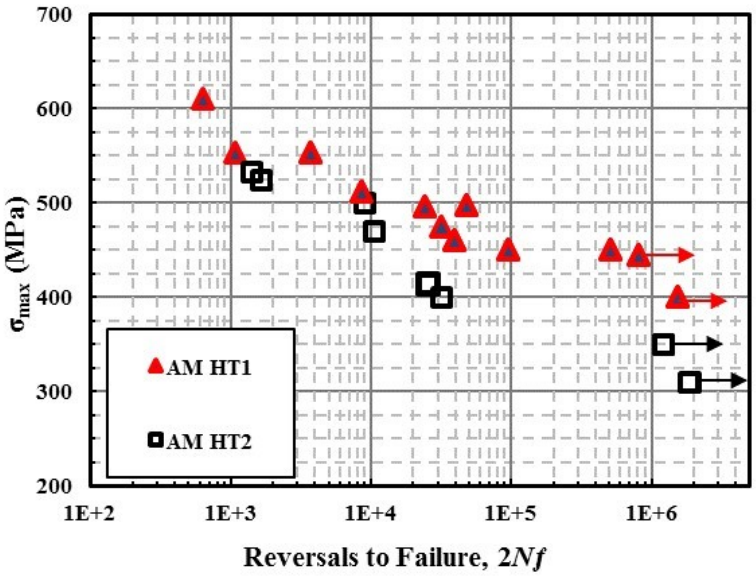

Figure 4.9 Scatter plot comparing stress-life of AMHT1 and AM HT2. Data points shown by arrow indicate failure in the grip. AM HT1 exhibit a larger stress level than the AM HT2 specimens, at the same strain level.

As mentioned earlier, the mechanical behavior and fatigue resistance of superelastic NiTi alloys is influenced by microstructural features of NiTi. Gall and Maier [44] reported that the size of Ni_4Ti_3 precipitates has an impact on the fatigue resistance of NiTi. They also proposed aging as a way to significantly improve the fatigue resistance of NiTi since smaller coherent Ni_4Ti_3 precipitates are produced by this method. However, the presence of small coherent Ni_4Ti_3 precipitates in the NiTi results in a stabilized martensite due to mechanical cycling and no dislocation activity.

4.4.4 Cyclic Hysteresis Loop

Increasing the number of loading cycles leads to the cyclic deformation behavior of the superelastic NiTi, similar to other cyclic hardening metallic materials. However, as reported in other studies on wrought NiTi, after a limited number of cycles (~150-200 cycles) the stress-strain behavior reaches a stable plateau state [35,36]. In the process of creating the cyclic stress-strain behavior for NiTi, different parameters are involved including the stress-induced martensite start stress, σ_s^{AM}, change in the size of the hysteresis loop, and sometimes, change in the accumulation of the residual strain. Furthermore, Mahtabi *et al.* [35] reported cyclic stress hardening and mean stress relaxation for wrought superelastic NiTi. In tests with larger mean strains, where the volume fraction of the martensitic phase is larger, more stress hardening and mean stress relaxation were observed.

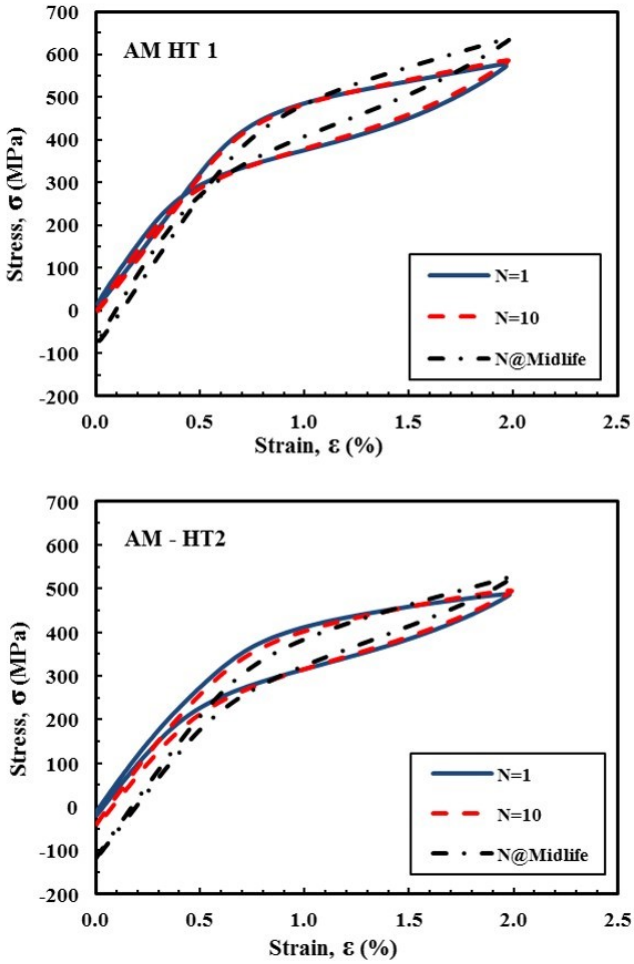

Figure 4.10 Cyclic stress-strain response at different loading cycles for: (a) AM HT1 and (b) AM HT2 specimens, N is the number of cycles. The amount of residual strain, for all the AM and wrought specimens at zero stress was negligible.

In Fig. 4.10, cyclic stress-strain behaviors for two different NiTi alloys (*i.e.* AM HT1 and HT2), at their first, tenth and mid-life cycles (with the ε_{max}=2.0%) are presented. For NiTi subjected to three different conditions, by increasing numbers of loading cycles, the A→M start stress (σ_s^{AM}) decreased and the stress level corresponding to the maximum strain (*i.e.* 2.0%) increased, as presented in Fig. 4.10. Furthermore, by increasing the number of cycles, the area surrounded by loading and unloading paths, *i.e.* hysteresis loop, decreased until the stress-strain behavior reached the plateau state. For

AM HT1 and AM HT2, increasing the stress range by increasing the number of loading cycles resulted in a cyclic hardening behavior. According to Fig. 4.10, for all the AM specimens, the amount of residual strain due to the residual martensitic phase at zero stress was negligible.

4.4.5 Fatigue Fracture Surface

SEM was used to observe the fracture surfaces of AM specimens. In order to determine the cause of fatigue failure in AM NiTi, the crack initiation sites were studied. As shown in Figs. 4.11, two common defect types observed on the fracture surface of AM NiTi specimens were spherical voids and irregular voids. Spherical voids can be created from gas bubbles generated by the laser in the melt pool. Whereas, lack of fusion and/or low laser penetration depth causes irregular voids, which are mostly unmelted regions. Various types of microstructural defects with different sizes and shapes were present in different areas on AM parts, such as near surface or subsurface areas which often act as crack initiation sites [46]. In this study, specimens were subjected to machining and polishing to reduce the surface roughness effect; however, the remaining defects present in the interior voids and subsurface area, located near the surface of the specimens, still accelerated the crack growth process. Machining and polishing the specimen's surface transformed subsurface voids into very small notches on the polished surface, which induced local stress concentrations causing fatigue damage [20].

Localized plastic deformation is caused by defects, such as particles and voids, where stress concentrations can cause the local stress level to exceed the yield strength of the material. The larger local stress level consequently leads to initiation of fatigue cracks under cyclic loading. The increase in the stress level due to localized stress concentration

results in the formation of a localized stress-induced martensitic phase. After unloading, the localized stress concentration causes changes in the area close to the defect, including residual martensitic phase, plastic deformation, or a combination of both. Plastic deformation and residual martensite may cause crack initiation in superelastic NiTi due to the sharp interfaces between austenite and martensite phases [47].

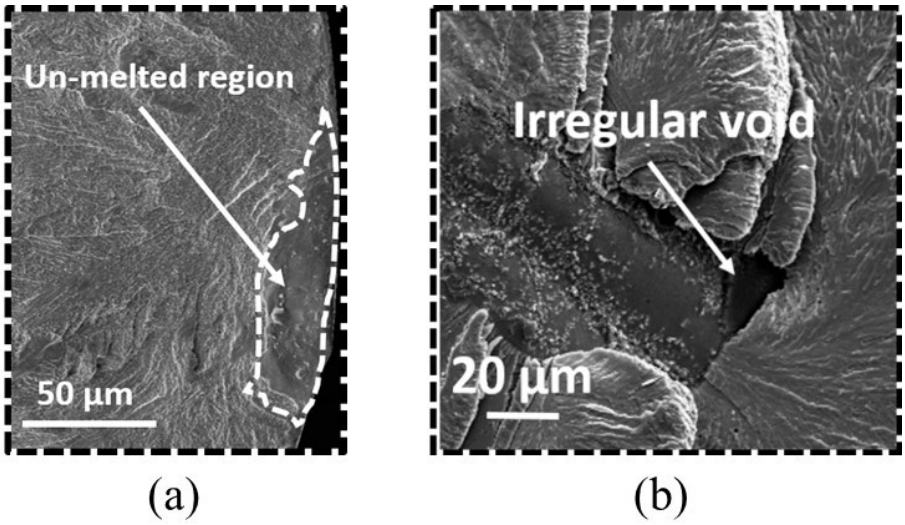

Figure 4.11 Fracture surfaces of two AM fatigue specimens (a and b) different types of defects are present that can act as crack initiation sites. Spherical voids are produced from the entrapped gas bubbles, as a result of the high laser energy applied to the melt pool, while irregular void, which are mostly un-melted regions, can be produced due to the lack of fusion and/or low laser penetration depth.

In Fig. 4.12, fracture surfaces for two AM HT1 specimens are shown, the specimen shown in Fig. 4.12a was exposed to the HCF regime (*i.e.* low strain amplitude) and the one on the right was under the LCF regime (*i.e.* high strain amplitude). On all the fracture surfaces, three main regions can be observed, including crack initiation, crack growth, and final fracture, which are correlated with different stages of the fatigue process. For superelastic NiTi, the majority of the fatigue life is devoted to the crack

incubation stage and the crack growth region is small; however, the fatigue testing regime (*i.e.* strain/stress amplitude) dictates the size of the crack growth region [32]. Fig. 4.12a shows that smaller strain amplitudes (*i.e.* HCF regime) results in a larger crack propagation area; however, a smaller crack growth area was typically produced under higher strain levels (*i.e.* LCF regime), as depicted in Fig. 4.12b.

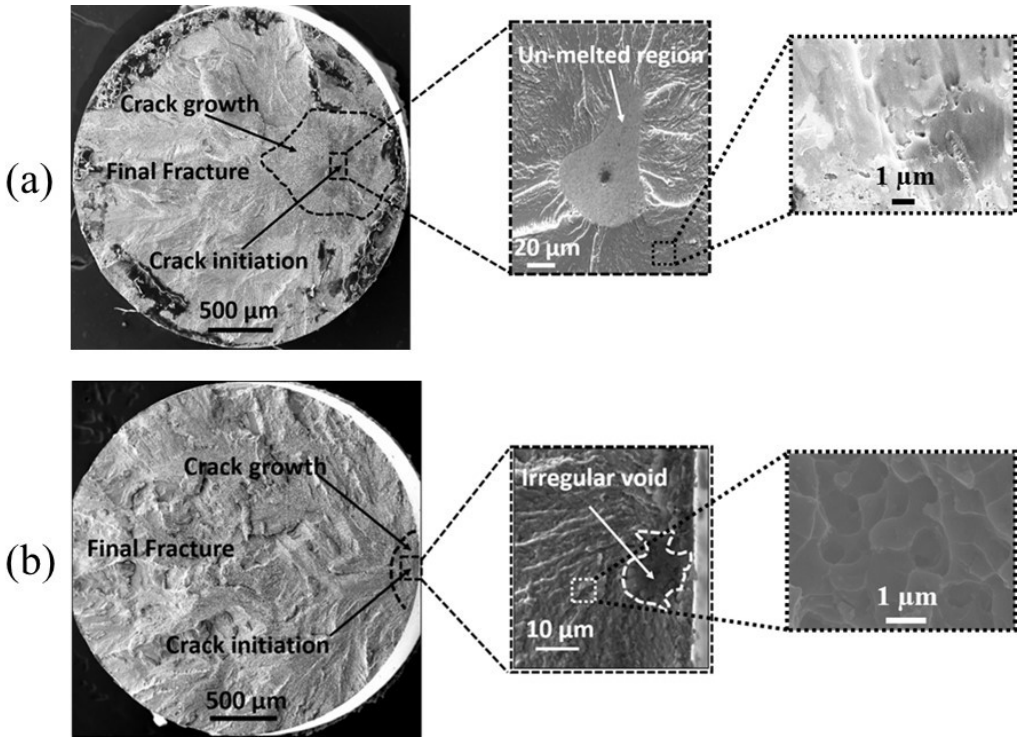

Figure 4.12 SEM images of fracture surface of two AM HT1 specimens: (a) a high cycle fatigue (HCF) specimen at ε_{max}=0.8% and $2N_f$ = 510,428 reversals, and (b) a low cycle fatigue (LCF) specimen at ε_{max}=2.0% and $2N_f$ = 634 reversals. At higher strain amplitudes (LCF regime) a larger crack propagation area is observed, while for lower strain levels (HCF regime) a smaller crack growth area typically exists.

On the other hand, since the NiTi specimen fracture occurs immediately after the crack incubation stage, the fatigue failure of the AM NiTi might be accelerated by the presence of even a few three-dimensional voids acting as the crack incubation sites. Thus,

presence of many planar-small volume voids or a few three-dimensional voids can significantly reduce the fatigue resistance, while its impact on the density of the part is negligible. Thus, in order to improve the fatigue behavior of AM NiTi parts, optimizing the process parameters, only based on density might not be enough. Further studies are still required to investigate the type, shape, and size of possible microstructural defects on the fatigue behavior of AM NiTi parts. Also, still unknown is material processing parameters that relate to the microstructures that in turn affect the fatigue behavior AM NiTi parts [20].

4.5 Microstructure-Sensitive Fatigue Model Correlation

Fig.4.13a shows the MSF model prediction compared to the experimental fatigue strain-life data. Based on the incubation and MSC/PSC crack regimes, the MSF model predictions are well correlated with the mean values of the fatigue life of the AM HT1 specimens. The MSF model supports the conclusion that the fatigue life is dominated by the microstructurally small and physically small fatigue crack growth in the low cycle regime and dominated by crack incubation in the high cycle regime. Furthermore, experimental results revealed that the fatigue cracks incubated and propagated from defects (*e.g*. voids or unmelted region). Additionally, the uncertainties that were associated with the MSF model could account for nearly the entire scatter for the experimental data. The uncertainty bands shown in Fig. 4.13a are calculated using a Monte Carlo (MC) method with calibrated parameters as nominal values and uncertainty of 5% implied in each variable [48]. The MC simulations were conducted for randomly chosen 10,000 datasets within the range of 5% of nominal values. In order to validate the process, the MSF model was calibrated based on the experimental strain-life data of AM

HT1. Then, all the calibrated parameters were used to predict the fatigue life of AM HT2. Thus, different microstructural constants for AM HT1 and AM HT2 cause the difference between the MSF prediction of fatigue life. In Fig. 4.13b, the MSF model fatigue life predictions for AM HT2 along with the experimental fatigue-life data of AM HT2 are shown. The model correlation looks very good in 4.13b. In order to explore the contributions of the two factors of incubation and MSC growth stages in the total life, a breakdown of the fatigue cycles predicted by the MSF model for incubation and MSC growth is shown in Figs. 4.13c and d. The results show that for all the strain ranges, the relative influence of incubation is greater than MSC growth with respect to the total life. The fatigue results obtained corroborate the results from Robertson *et al*. [49], which show that as soon as a crack nucleates it starts to grow and fracture occurs slightly after nucleation due to the high crack growth rate of NiTi.

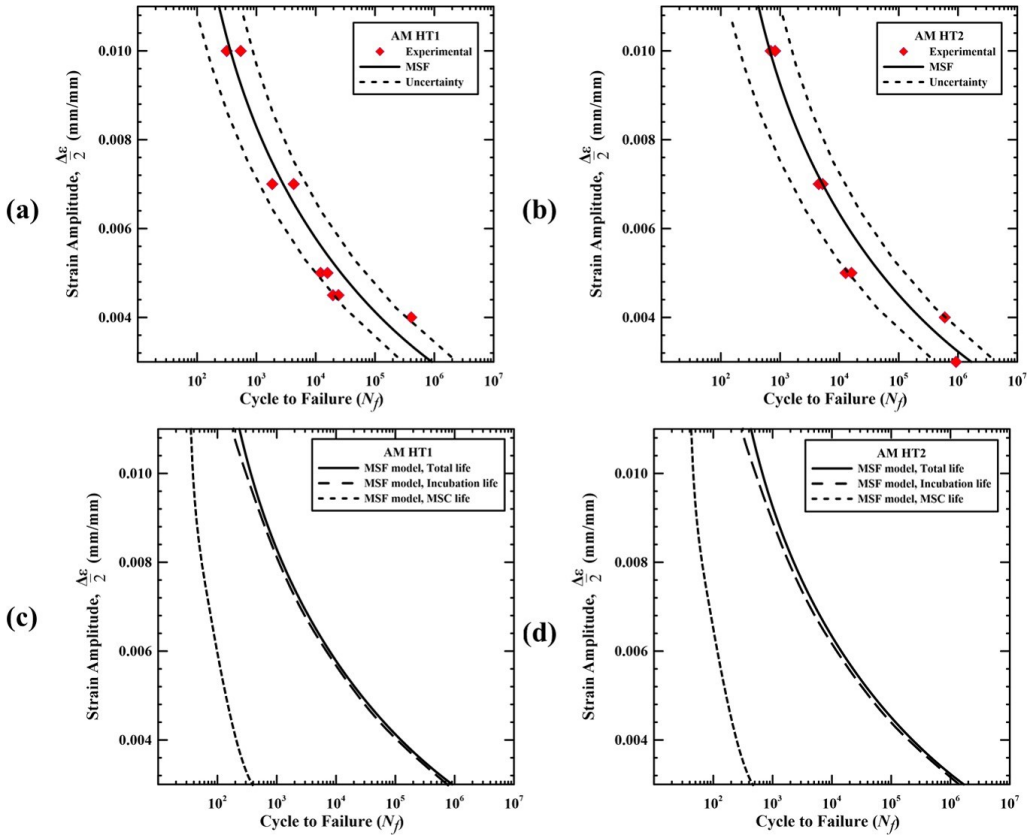

Figure 4.13 Microstructure-sensitive fatigue model (calibration of the model using data of aging specimens, (b) validating of the model using data of aging plus annealing specimens, (c) and (d) the multistage fatigue (MSF) model prediction for the breakdown of regimes of incubation and small crack growth for AM HT1 and AM HT2 specimens.

The model parameters that are used to relate the MSF predictions to cyclic uniaxial strain-life results for AM HT1 are listed in Table 4.5.

Table 4.5 The model parameters used to overlay the MultiStage Fatigue (MSF) model on experimental data.

Constant	AM NiTi	Constant	AM NiTi
k'	1106.64	**CTD_{th}**	2.86E-09
n'	0.150606	**af**	500
CN	3.79697	**GS Exponent**	1.64848
CM	-7.68789	**Pore Exponent**	0.014
α	-4.34545	**GMO Exponent**	0.301515
q	1.63637		
Y1	860.606		
Y2	133.334		
ψ	1.38182		
R	1.63636		
E Exponent	1.60606		
Particle Exponent	0.42424		
omega	46.303		
ainic	2.94545		
theta	0.072728		
n	6.93334		
CI	3173.91		
CII	0.001		
chi	0.32		

4.6 Summary

Following conclusions were drawn from both the experimental and modeling portions of this study on fatigue damage in AM NiTi.

(1) In the LCF regime, the fatigue lives for AM HT2 specimens were typically greater than HT1 specimens; however, similar fatigue lives were observed for both HT1 and HT2 specimens in the HCF regime.

(2) Manufacturing voids and unmelted particles were the main defects that caused the fatigue cracks for AM NiTi.

(3) The MSF model was correlated to experimental strain-life results for AM NiTi for the first time. The model correlation distinguished between the different strain-life curves that arose from microstructures arising from different heat treatments with the same material constants for the NiTi.

4.7 References

[1] Duerig TW, Pelton A, Stöckel D. An overview of Nitinol medical applications. Mater Sci Eng A 1999;273:149–60.

[2] Pelton AR, Dicello J, Miyazaki S. Optimisation of processing and properties of medical grade Nitinol wire. Minim Invasive Ther Allied Technol 2000;9:107–18.

[3] Plotino G, Grande NM, Cordaro M, Testarelli L, Gambarini G. A review of cyclic fatigue testing of nickel-titanium rotary instruments. J Endod 2009;35:1469–76.

[4] Andani MT, Shayesteh Moghaddam N, Haberland C, Dean D, Miller MJ, Elahinia M. Metals for bone implants. Part 1. Powder metallurgy and implant rendering. Acta Biomater 2014;10:4058–70.

[5] Moghaddam NS, Elahinia M, Miller M, Dean D. Enhancement of bone implants by substituting Nitinol for Titanium (Ti-6Al-4V): A modeling comparison 2014:V001T03A031.

[6] Griffith ML, Keicher DL, Romero JA, Atwood CL, Harwell LD, Greene DL, et al. Laser engineered net shaping (LENS) for the fabrication of metallic components. Sandia National Labs., Albuquerque, NM (United States); 1996.

[7] Gu DD, Meiners W, Wissenbach K, Poprawe R. Laser additive manufacturing of metallic components: materials, processes and mechanisms. Int Mater Rev 2012;57:133–64.

[8] Shamsaei N, Yadollahi A, Bian L, Thompson SM. An overview of direct laser deposition for additive manufacturing; Part II: Mechanical behavior, process parameter optimization and control. Addit Manuf 2015;8:12–35.

[9] Bagheri A, Shamsaei N, Thompson SM. Microstructure and Mechanical Properties of Ti-6Al-4V Parts Fabricated by Laser Engineering Net Shaping. IMECE2015-51698, vol. 2A: Advanced Manufacturing, Houston: ASME; 2015, p. V02AT02A005-013.

[10] Otsuka K, Ren X. Physical metallurgy of Ti–Ni-based shape memory alloys. Prog Mater Sci 2005;50:511–678.

[11] Gall K, Sehitoglu H, Chumlyakov YI, Zuev YL, Karaman I. The role of coherent precipitates in martensitic transformations in single crystal and polycrystalline Ti-50.8 at% Ni. Scr Mater 1998;39:699–705.

[12] Saedi S, Turabi AS, Andani MT, Haberland C, Elahinia M, Karaca H. Thermomechanical characterization of Ni-rich NiTi fabricated by selective laser melting. Smart Mater Struct 2016;25:035005.

[13] Nishida M, Wayman CM, Honma T. Precipitation processes in near-equiatomic TiNi shape memory alloys. Metall Trans A 1986;17:1505–15.

[14] Karaca HE, Saghaian SM, Ded G, Tobe H, Basaran B, Maier HJ, et al. Effects of nanoprecipitation on the shape memory and material properties of an Ni-rich NiTiHf high temperature shape memory alloy. Acta Mater 2013;61:7422–31.

[15] Sehitoglu H, Anderson R, Karaman I, Gall K, Chumlyakov Y. Cyclic deformation behavior of single crystal NiTi. Mater Sci Eng A 2001;314:67–74.

[16] Bian L, Thompson SM, Shamsaei N. Mechanical Properties and Microstructural Features of Direct Laser-Deposited Ti-6Al-4V. JOM 2015;67:629–38.

[17] Rafi HK, Pal D, Patil N, Starr TL, Stucker BE. Microstructure and mechanical behavior of 17-4 precipitation hardenable steel processed by selective laser melting. J Mater Eng Perform 2014;23:4421–8.

[18] Sehrt JT, Witt G. Dynamic strength and fracture toughness analysis of beam melted parts. Proc. 36th Int. MATADOR Conf., Springer; 2010, p. 385–8.

[19] Stoffregen HA, Butterweck K, Abele E. Fatigue analysis in selective laser melting: review and investigation of thin-walled actuator housings. 25th Solid Free. Fabr. Symp, Austin, Texas: University of Texas in Austin; 2014.

[20] Yadollahi A, Shamsaei N, Thompson SM, Elwany A, Bian L. Effects of building orientation and heat treatment on fatigue behavior of selective laser melted 17-4 PH stainless steel. Int J Fatigue 2016.

[21] Mahtabi MJ, Shamsaei N, Mitchell MR. Fatigue of Nitinol: The state-of-the-art and ongoing challenges. J Mech Behav Biomed Mater 2015;50:228–54.

[22] Suresh S. Fatigue of materials. Cambridge university press; 1998.

[23] McDowell DL, Gall K, Horstemeyer MF, Fan J. Microstructure-based fatigue modeling of cast A356-T6 alloy. Eng Fract Mech 2003;70:49–80.

[24] Jordon JB, Horstemeyer MF, Yang N, Major JF, Gall KA, Fan J, et al. Microstructural Inclusion Influence on Fatigue of a Cast A356 Aluminum Alloy. Metall Mater Trans A 2010;41:356.

[25] Xue Y, El Kadiri H, Horstemeyer MF, Jordon JB, Weiland H. Micromechanisms of multistage fatigue crack growth in a high-strength aluminum alloy. Acta Mater 2007;55:1975–1984.

[26] Xue Y, McDowell DL, Horstemeyer MF, Dale MH, Jordon JB. Microstructure-based multistage fatigue modeling of aluminum alloy 7075-T651. Eng Fract Mech 2007;74:2810–23.

[27] Xue Y, Horstemeyer MF, McDowell DL, El Kadiri H, Fan J. Microstructure-based multistage fatigue modeling of a cast AE44 magnesium alloy. Int J Fatigue 2007;29:666–676.

[28] Jordon JB, Gibson JB, Horstemeyer MF, Kadiri HE, Baird JC, Luo AA. Effect of twinning, slip, and inclusions on the fatigue anisotropy of extrusion-textured AZ61 magnesium alloy. Mater Sci Eng A 2011;528:6860–71.

[29] Rettberg LH, Jordon JB, Horstemeyer MF, Jones JW. Low-Cycle Fatigue Behavior of Die-Cast Mg Alloys AZ91 and AM60. Metall Mater Trans A 2012;43:2260–74.

[30] Lugo M, Jordon JB, Solanki KN, Hector LG, Bernard JD, Luo AA, et al. Role of different material processing methods on the fatigue behavior of an AZ31 magnesium alloy. Int J Fatigue 2013;52:131–143.

[31] Xue Y, Pascu A, Horstemeyer MF, Wang L, Wang PT. Microporosity effects on cyclic plasticity and fatigue of LENS TM-processed steel. Acta Mater 2010;58:4029–4038.

[32] Robertson SW, Pelton AR, Ritchie RO. Mechanical fatigue and fracture of Nitinol. Int Mater Rev 2012;57:1–37.

[33] ASTM B214−15. Standard Test Method for Sieve Analysis of Metal Powders. West Conshohocken, PA: ASTM International; 2011.

[34] ASTM E606 / E606M-12. Test method for strain-controlled fatigue testing. West Conshohocken, PA: ASTM International; 2012.

[35] Mahtabi MJ, Shamsaei N, Rutherford B. Mean Strain Effects on the Fatigue Behavior of Superelastic Nitinol Alloys: An Experimental Investigation. Procedia Eng 2015;133:646–54.

[36] Gall K, Horstemeyer M, McDowell DL, Fan J. Finite element analysis of the stress distributions near damaged Si particle clusters in cast Al–Si alloys. Mech Mater 2000;32:277–301.

[37] Brown DW, Jain A, Agnew SR, Clausen B. Twinning and Detwinning during Cyclic Deformation of Mg Alloy AZ31B. Mater Sci Forum 2007;539–543:3407–13.

[38] Hayhurst D, Leckie F, McDowell D. Damage Growth Under Nonproportional Loading. In: Miller K, Brown M, editors. Multiaxial Fatigue, 100 Barr Harbor Drive, PO Box C700, West Conshohocken, PA 19428-2959: ASTM International; 1985, p. 688-688–12.

[39] Eggeler G, Hornbogen E, Yawny A, Heckmann A, Wagner M. Structural and functional fatigue of NiTi shape memory alloys. Mater Sci Eng A 2004;378:24–33.

[40] Wilkes KE, Liaw PK, Wilkes KE. The fatigue behavior of shape-memory alloys. JOM J Miner Met Mater Soc 2000;52:45–51.

[41] Melton K, Mercier O. Fatigue of NiTi thermoelastic martensites. Acta Metall 1979;27:137–144.

[42] Gall K, Tyber J, Wilkesanders G, Robertson SW, Ritchie RO, Maier HJ. Effect of microstructure on the fatigue of hot-rolled and cold-drawn NiTi shape memory alloys. Mater Sci Eng A 2008;486:389–403.

[43] Zhou P, Zhou J, Ye Z, Hong X, Huang H, Xu W. Effect of grain size and misorientation angle on fatigue crack growth of nanocrystalline materials. Mater Sci Eng A 2016;663:1–7.

[44] Gall K, Maier HJ. Cyclic deformation mechanisms in precipitated NiTi shape memory alloys. Acta Mater 2002;50:4643–57.

[45] Miyazaki S, Imai T, Igo Y, Otsuka K. Effect of cyclic deformation on the pseudoelasticity characteristics of Ti-Ni alloys. Metall Trans A 1986;17:115–20.

[46] Sterling AJ, Torries B, Shamsaei N, Thompson SM, Seely DW. Fatigue behavior and failure mechanisms of direct laser deposited Ti–6Al–4V. Mater Sci Eng A 2016;655:100–12.

[47] Tabanli RM, Simha NK, Berg BT. Mean strain effects on the fatigue properties of superelastic NiTi. Metall Mater Trans A 2001;32:1866–9.

[48] Hughes, J.M., Horstemeyer, M.F., Carino, R., Sukhija, N., Lawrimore, W.B., Kim, S. and Baskes, M.I., 2015. Hierarchical bridging between ab initio and atomistic level computations: Sensitivity and uncertainty analysis for the modified embedded-atom method (meam) potential (part b). Jom, 67(1), pp.148-153.

[49] Robertson, S.W., Pelton, A.R. and Ritchie, R.O., 2012. Mechanical fatigue and fracture of Nitinol. International Materials Reviews, 57(1), pp.1-37.

CHAPTER V

GENERAL CONCLUSIONS

Laser-based additive manufacturing is an active area of study, and has recently attracted lots of attention [1-5]. Over the years, many advancements have occurred in material properties required for extreme applications [6-8]; however, economical ways to process these materials have been absent [8]. Thus, laser direct deposition provides a unique capability for synthesis and fabrication of components without the risk of contamination or oxidation [3, 5]. Although the objective of this study was to synthesize and characterize Additively Manufactured (AM) alloys and then model the fatigue behavior with the MultiStage Fatigue (MSF) model, AM can be exploited for the synthesis of other alloys as well.

For AM techniques, thermal dissipation during the AM process is significantly affected by changes in the size, geometry, and number of fabricated parts on the build plate [1,4]. The size and geometry of fabricated parts strongly affect the thermal history, and consequently, the resultant microstructure and mechanical properties [1,4]. In addition, using current laser-based AM methods to obtain a homogenous microstructure, and defect distribution for parts with complex geometry is still challenging [4].

Over the past decade, numerous studies focused on characterizing the fatigue behavior of AM metals; however, more research is required to develop more accurate and reliable methodologies for estimation of fatigue life in AM parts [9-12]. Achieving this

objective is challenging as it requires standardized approaches and measurement techniques [9]. In general, impurities introduced by the AM process are one of the major factors impacting the damage evolution of metallic AM materials under cyclic loading [9-12]. Furthermore, voids are the major life limiting factor, and the most dominant mechanism for fatigue crack initiation under cyclic loadings in AM metals [9]. The large scatter observed in the AM fatigue data is due to variations in location, shape, and size of voids which act as crack incubation sites [9,10]. Durability and HCF performance of AM parts are improved by the hot isostatic pressing (HIP) process, which helps by fusing un-melted particles, decreasing the voids size and smoothening their sharp angles, and even closing some voids [4]. Multiple factors play important roles in this process, including the parameters chosen for HIP (*i.e*. pressure and temperature), material's microstructure, associated failure mechanism, void location, and the encapsulated gas inside of the voids [4]. Furthermore, fatigue behavior of machined AM parts is significantly affected by the voids' characteristics – especially their locations – and the thickness of the removed surface during machining [9]. The thickness of the outer layer that is trimmed away during machining determines if the voids are removed or brought to the surface [4, 9]. Regarding the impact of post fabrication process, AM HT1 specimens show longer fatigue lives in the short life regime, while, in the long life regime both HT1 and HT2 AM specimens show similar fatigue lives.

At last, a microstructure-based MultiStage Fatigue (MSF) model for AM specimens is proposed. The model was modified by implementing the effect of grain misorientation and grain orientation angle for a better fatigue life prediction of additively manufactured NiTi. The MSF model was correlated to experimental strain-life results for

AM NiTi for the first time. The MSF model supports the conclusion that the fatigue life is dominated by the microstructurally small and physically small fatigue crack growth in the low cycle regime and dominated by crack incubation in the high cycle regime [13]. Additionally, the uncertainties that were associated with the MSF model could account for nearly the entire scatter for the experimental data [14].

References

[1] Thompson SM, Bian L, Shamsaei N, Yadollahi A. An overview of Direct Laser Deposition for additive manufacturing; Part I: Transport phenomena, modeling and diagnostics. Addit Manuf 2015;8:36–62. doi:10.1016/j.addma.2015.07.001.

[2] Bikas, H., Stavropoulos, P. and Chryssolouris, G., 2016. Additive manufacturing methods and modelling approaches: a critical review. The International Journal of Advanced Manufacturing Technology, 83(1-4), pp.389-405.

[3] Frazier WE. Metal Additive Manufacturing: A Review. J Mater Eng Perform 2014;23:1917–28. doi:10.1007/s11665-014-0958-z.

[4] Shamsaei N, Yadollahi A, Bian L, Thompson SM. An overview of direct laser deposition for additive manufacturing; Part II: Mechanical behavior, process parameter optimization and control. Addit Manuf 2015;8:12–35. doi:10.1016/j.addma.2015.07.002.

[5] Huang, Y., Leu, M.C., Mazumder, J. and Donmez, A., 2015. Additive manufacturing: current state, future potential, gaps and needs, and recommendations. Journal of Manufacturing Science and Engineering, 137(1), p.014001.

[6] Lewandowski, J.J. and Seifi, M., 2016. Metal additive manufacturing: a review of mechanical properties. Annual Review of Materials Research, 46, pp.151-186.

[7] Guo, N. and Leu, M.C., 2013. Additive manufacturing: technology, applications and research needs. Frontiers of Mechanical Engineering, 8(3), pp.215-243.

[8] Khairallah, S.A., Anderson, A.T., Rubenchik, A. and King, W.E., 2016. Laser powder-bed fusion additive manufacturing: Physics of complex melt flow and formation mechanisms of pores, spatter, and denudation zones. Acta Materialia, 108, pp.36-45.

[9] Yadollahi A, Shamsaei N, Thompson SM, Elwany A, Bian L. Effects of building orientation and heat treatment on fatigue behavior of selective laser melted 17-4 PH stainless steel. Int J Fatigue 2016. doi:10.1016/j.ijfatigue.2016.03.014.

[10] Brandl, E., Heckenberger, U., Holzinger, V. and Buchbinder, D., 2012. Additive manufactured AlSi10Mg samples using Selective Laser Melting (SLM): Microstructure, high cycle fatigue, and fracture behavior. Materials & Design, 34, pp.159-169.

[11] Spierings, A.B., Starr, T.L. and Wegener, K., 2013. Fatigue performance of additive manufactured metallic parts. Rapid Prototyping Journal, 19(2), pp.88-94.

[12] Chan, K.S., Koike, M., Mason, R.L. and Okabe, T., 2013. Fatigue life of titanium alloys fabricated by additive layer manufacturing techniques for dental implants. Metallurgical and Materials Transactions A, 44(2), pp.1010-1022.

[13] Jordon JB, Horstemeyer MF, Yang N, Major JF, Gall KA, Fan J, et al. Microstructural Inclusion Influence on Fatigue of a Cast A356 Aluminum Alloy. Metall Mater Trans A 2010;41:356.

[14] Hughes, J.M., Horstemeyer, M.F., Carino, R., Sukhija, N., Lawrimore, W.B., Kim, S. and Baskes, M.I., 2015. Hierarchical bridging between ab initio and atomistic level computations: Sensitivity and uncertainty analysis for the modified embedded-atom method (meam) potential (part b). Jom, 67(1), pp.148-153.

CHAPTER VI

FUTURE WORKS

Mechanical testing methods, design procedures, and standards may need to be revised for Additively Manufactured (AM) materials. The thermal history experienced by each specimen has a significant impact on the part properties and performance. Thus, in the mechanical testing methods and design procedures, the thermal history needs to be addressed. In addition, as fatigue failure mechanisms of AM metallic parts are unique and different from the wrought materials, the heat treatment schedule found effective for wrought materials might not improve the structural integrity of AM parts. Therefore, developing specific and exclusive post-manufacturing processes (*e.g.*, heat treatment) for AM parts is essential.

Developing models to predict the mechanical behavior based on the microstructural details makes prototype testing unnecessary. In addition, these models are beneficial for the improvement of the part's reliability and design optimization. Finite element analysis (FEA) can be added to microstructural sensitive mechanical models, which can locate the fatigue failure initiation sites. As a result, a reverse design approach should be exploited to calculate the process/design parameters with the input data of the targeted application, geometry, and service loading. Hence, improving the fatigue resistance of AM parts by improving the surface quality and minimizing defects only in critical locations is a more economically favorable strategy.

Further research in this field is required to introduce the AM technology to industries to be exploited appropriately in the mass-production of supplies. So, design guidelines and feature values for industrial machines must be compiled and published. For new processes and machines that are under development, this information should be gathered during their development process. While this information is accessible to designers, designs will go in a direction to benefit from additive manufacturing's unique capabilities. With designs being streamlined for metal AM processes, the time and iteration that can occur in the information exchange between designers and machine operators can be dramatically reduced.

Future work on the process selection tool consists of a more formal scoring system, user testing for intuitiveness, and evaluating the AM process selection tool as a teaching tool. Future research is required in feature recognition of Computer Aided Design (CAD) designs. If the feature recognition and part analysis become automated, each AM process can be easily simulated by redesigning the process selection tool. Then, the build time, cost estimation, and final part geometry would be provided to the designer.

In order to take full benefits of metal additive manufacturing technology, the capabilities and limitations of this process should be thoroughly understood by designers and engineers. By spreading this knowledge about how to use the AM process among designers, more advanced parts can be developed, and its capabilities increase. Distributing and expanding the design guidelines for metal additive manufacturing processes is one way to achieve this goal. A powerful method to spread design guidelines is the process selection tool.

APPENDIX A

NOMENCLATURE

A.1 Nomenclature

AM	Additive Manufacturing / Additively Manufactured
A→M	Austenite to martensite transformation
DLD	Direct Laser Deposition
E_A	Austenite modulus
E_M	Stress-induced martensite modulus
HCF	High Cycle Fatigue
HT	Heat Treatment/Heat-treated
LCF	Low Cycle Fatigue
LENS	Laser Engineered Net Shaping
MCF	Mid Cycle Fatigue
$2N_f$	Number of reversals to failure
N_f	Number of cycles to failure
ε_{max}	Maximum strain
ε_{min}	Minimum strain
ε_s^{AM}	A→M start strain
ε_f^{AM}	A→M finish strain
σ_s^{AM}	A→M start stress